Universität Stuttgart

High pressure dielectric studies on hybrid crystals: perovskites and beryl

Von der Fakultät Mathematik und Physik der Universität Stuttgart zur Erlangung der Würde eines Doktors der Naturwissenschaften (Dr. rer. nat.) genehmigte Abhandlung

Vorgelegt von

Yuk Tai Chan

aus Hong Kong

Hauptberichter:	Prof. Dr. Martin Dressel
Mitberichter:	Prof. Dr. Hidenori Takagi
Tag der mündlichen Prüfung:	20 July 2022
Prüfungsvorsitzend:	Prof. Dr. Peter Büchler

1. Physikalisches Institut der Universität Stuttgart

2022

Zusammenfassung

Die dielektrische Hochfrequenzspektroskopie (RF) ist ein vielseitiges Instrument zur Untersuchung molekularen Bewegungen und der Ionendynamik in einem System aus kondensierter Materie, während die Anwendung von physikalischem Druck als ausgereifte Technik für das Engineering Gitterstruktur und zur Feinabstimmung der Materialeigenschaften. Die Kombination dieser beiden Fachkenntnisse hat zu bemerkenswerten Entdeckungen in komplexen elektronisch korrelierten und weichen Gittersystemen geführt, z. B. im organischen Mott-Isolator, und exotische Phasen im Quantenbereich hervorgebracht. Nichtsdestotrotz ist der volle Nutzen der dielektrischen Druckspektroskopie noch nicht voll ausgeschöpft, da es noch ein großes Verbesserungspotential gibt. Bereits vor dem Beginn dieser Arbeit konnten in dem dielektrische Aufbau, Druckmessungen mittels kolbenartiger Druckzellen ausgeführt werden, welche den Vorteil hoher Genauigkeit haben, aber bei einem begrenzten Druck von maximal 1 GPa arbeiten. Damit der Druck neue Materiezustände hervorrufen kann, ist empirisch die in der Größenordnung von 10 GPa die Voraussetzung, und um diese zehnfache Verbesserung zu erreichen, ist eine fortgeschrittenere Drucktechnik erforderlich. Diese Arbeit befasst sich mit der Entwicklung und der Einbindung der Diamant-Ambosszellen-Technik mit dem bestehenden kryogenen RF-Dielektrikum-Messsystem und zielte darauf ab die Druckgrenze von den bisherigen 1 GPa auf 10 GPa zu erhöhen.

Der erste Teil dieser Arbeit dokumentiert die Überlegungen und die gere-

gelte Umsetzung der Diamant-Amboss-Zelle für dielektrische Messungen, ergänzt durch die Druckaufzeichnung und die Kalibrierungsergebnisse. Der zweite Teil dieser Arbeit besteht aus Untersuchungen an zwei verschiedenen Materialien: hybride anorganisch-organische Perowskite und wassereinschließender Beryll. Die beiden Systeme wurden ausgewählt, um die Eignung und Fähigkeit des neu eingerichteten dielektrischen Hochdruckaufbaus zu testen.

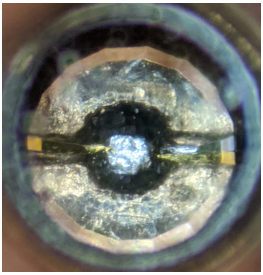

RF dielektrischer Aufbau in DAC

Diamant-Amboss-Zellen (DAC) arbeiten mittels zweier gegenüberliegenden Diamant-Ambosse, die von beiden gegenüberliegenden Seiten gegen das Bohrloch einer besonders harten Dichtung drücken. Der Druck, der von den sich berührenden Ambossflächen ausgeübt wird, wird durch die Füllung mit einem Druckmedium, d.h. einem Medium mit niedriger Viskosität, gleichmäßig über das Volumen verteilt. Der maximale Druck, den der Hohlraum aufnehmen kann, wird durch die Härte der Dichtung und der Reinheit der Hohlraumwand bestimmt. Ersteres bestimmt die theoretische Druckgrenze, letzteres verhindert ein Durchbrechen durch Druckstau. Bei Diamant-Ambosszellen, die für optische Messungen, z. B. Röntgenbeugung und Infrarotspektroskopie, präpariert sind, kann das Signal durch die Diamant-Ambosse hindurch übertragen werden, und die Hohlraumwand kann defektfrei gemacht werden, so dass die resultierende Druckgrenze bis zu 100 GPa reicht. Andererseits erfordert die dielektrische Messung Öffnungen in der versiegelten Kavität für die Zugänge zu den elektrischen Verbindungen. Außerdem sind Hochfrequenzsignale anfällig für Dämpfungen, so dass die elektrischen Verbindungen idealerweise vollständig durch Koaxialkabel erhalten bleiben sollten. Dieser Konflikt stellt eine große technische Herausforderung bei der Entwicklung der dielektrischen Druckspektroskopie dar. Die in dieser Arbeit gewählte Lösung besteht in einem leichten Umbau der harten Metalldichtung, die eine isolierte, aber immer noch harte Bahn für die elektrischen Drähte bildet, wobei die Koaxialkabel in unmittelbarer Nähe der Diamantambosse

liegen um eine minimale Drahtexposition zu gewährleisten. Werkzeuge wie das Funkenerosionsverfahren werden zum sauberen Bohren von Löchern und zum Ausheben von Gräben eingesetzt. Wärmebehandeltes, starkes Epoxidharz fixiert die isolierte Straße. Für die elektrischen Verbindungen werden dünne Golddrähte und Platinstreifen verwendet, die einen geringen Querschnitt aufweisen und somit den Hohlraum am wenigsten gefährden. Kalibrierungen des Prototyps haben gezeigt, dass die Streukapazität und der Leitwert akzeptabel niedrig sind. Die Druckdecke hat sich in den beiden erfolgreichen erfolgreichen Projekten bewiesen.

Hybride Perowskite sind eines der am meisten erwarteten Materialien der nächsten Generation im Rahmen der Erzeugung von Solarenergie. Dessen Strukturstabilität, Ionenleitfähigkeit und Dynamik spielen eine entscheidende Rolle für dessen Leistung. Hybrid-Perowskit hat die chemische Formel ABX_3, in der A^+ ein organisches Kation mit anorganischen Anteilen ist. Zum Beginns dieser Arbeit war das am intensivsten untersuchte und für die Vermarktung vorgesehene Perowskit, Methylammoniumbleijodid ($CH_3NH_3PbI_3$), mit den Nachteilen einer instabilen Struktur aufgrund von Bleidiffusion und ernsthafter Ionenwanderung konfrontiert. Das angeborene permanente dipolare Methylammoniumkation wird durch das PbI_6-Tetraedernetz eingeschlossen, kann sich aber frei drehen und bewegen. Gleichermaßen sind I^- und sogar Pb^{2+} Ionen für die Diffusion geeignet. Wenn zum Beispiel ein flüssiger Elektrolyt auf die Perowskit-Hybridschicht trifft, kommt es zu einer starken Auflösung welche die Perowskit-Schicht durchbrechen kann. Selbst wenn ein fester Ladungsträgertransporter eingesetzt wird, würde die Auflösung in Anwesenheit von hoher Luftfeuchtigkeit immer noch auftreten.

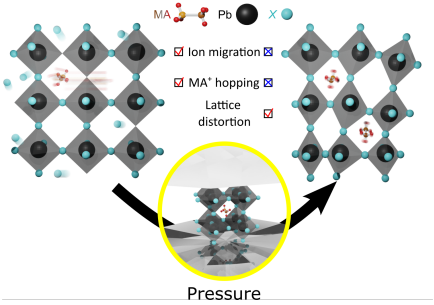

Um die hinderlichen Probleme zu lösen oder ein alternatives Material zu finden, ist es notwendig, die zugrunde liegende Mechanik, die für die starke Ionenwanderung verantwortlich ist, sowie den Zusammenhang zwischen

der Struktur und den chemischen Einheiten zu verstehen. Die Hochdruck-Hochfrequenz-Dielektrikums-Spektroskopie passt gut zu den gestellten Fragen, da die Ionenausbreitung und die elektrische Polarisation im Frequenzbereich erfasst werden und der strukturelle Faktor durch Beobachtung der Druckentwicklung der Eigenschaften erkannt Eigenschaften erfasst werden kann. In dieser Arbeit wurden die drei Methylammonium-Bleihalogenide bis zu einer kryogenen Temperatur von 4 K und bis zu 5 GPa gemessen. Die vollständigen Temperatur-Druck-Struktur-Phasendiagramme von $CH_3NH_3PbX_3$ (X = I, Br, Cl) wurden untersucht, wobei in allen Fällen eine Stabilisierung der orthorhombischen Niedertemperaturphase bei Raumtemperatur in jedem Halogenid zu beobachten ist. Die Frequenzabhängigkeit der dielektrischen Eigenschaften spiegelt den Grad der Ionenwanderung und der langsamen molekularen Relaxation wider. Es wurde eine kHz-Relaxation entdeckt, die nur die nur in der isotropen Phase bei niedrigem Druck auftritt und aufhört, wenn das System in die orthorhombische Phase eintritt, begleitet von einer vollständigen Unterdrückung der Ionenwanderung. Die Verneinung der beiden Bewegungen zeigt einen delokalisationsfreien Zustand an, der für photovoltaische Anwendungen günstig ist. Daraus folgt, dass Substitution von sperrigeren Kationen oder kleinerer Halogenidionen, die die Wirkung physikalischen Drucks zu einer verbesserten strukturellen Stabilität und verbesserter Lichtsammelleistung führen.

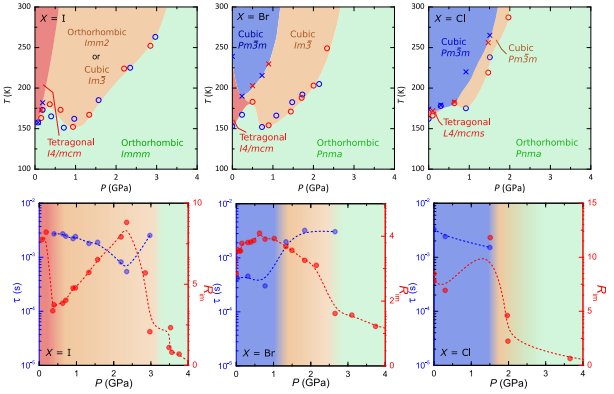

Phasendiagramme und Entwicklung der Ionenbewegungen in $CH_3NH_3PbX_3$ (X = I, Br, Cl)

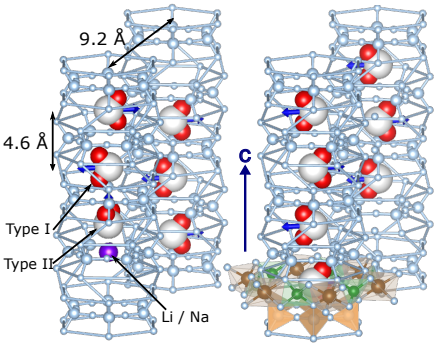

Wassermoleküle besitzen starke elektrische Dipole und sind aufgrund ihrer geringen Masse und ihrer einfachen chemischen Formel ideale Kandidaten für die Untersuchung von wechselwirkenden "Punkt"-Dipolen. In frei beweglicher Form wird ihre Wechselwirkung jedoch von der Wasserstoffbrückenbindung mit kurzer Reichweite dominiert. Durch die Synthese von Beryllkristallen in wässriger Umgebung entsteht ein wassereinschließender Beryll. Im Inneren des Beryllkristalls sind die Wassermoleküle von der Wasserstoffbrückenbindung getrennt, so dass eine reine Dipol-Dipol-Wechselwirkung entsteht. Mit anderen Worten, es wird ein dipolar gekoppeltes Netzwerk hergestellt. Die Pionierstudie hatte impliziert, dass ein ferroelektrischer Phasenübergang in diesem eingeschlossenen Wasser auftritt, begründet durch die Beobachtung einsetzender erroelektrizität, ausgedrückt durch ein gesättigtes Plateau im Realteil der Dielektrizitätskonstanten bei niedriger Temperatur und eines ferroelektrischen weichen Mode aufgezeigt. Die Verhinderung einer vollständigen Ladungsordnung ist nachweislich auf das Tunneln zwischen den sechszähligen azimutalen Potentialminima der Wasserdipole zurückzuführen. Diese Verbote können potenziell durch zwei Ansätze aufgehoben werden: Substitution schwerer Isotope und Verstärkung der Dipol-Dipol-Kopplungsstärke. Ersteres verstärkt die Phononmodenerweichung und verringert die Wahrscheinlichkeit des Tunnelns. Der zweite Ansatz verringert den Abstand zwischen den Dipolen, und erhöht somit die Kopplungsstärke proportional zu r^3.

In dieser Arbeit wurden H_2O- und D_2O-gefüllte Beryls bis zu 7 GPa unter Druck gesetzt und bis zu 4 K gemessen. Die Robustheit der Quantenfluktuation und der Abstand vom Phasenübergang werden durch das charakteristische Plateau der realen Dielektrizitätskonstante bestimmt. Die Ergebnisse haben die Vorteile der Erhöhung der Massen der Dipole bestätigt,

da schweres Wasser in Beryll einen geringeren Quanteneffekt aufweist. Die Anwendung von Druck führt zu einem progressiv verstärkten und schließlich gesättigten Quanteneffekt, der durch die Unterdrückung der Barriere des Lokalisierungspotentials modelliert wird, was durch die Energieabschätzung des frei rotierenden Wasserdipols belegt wird. Der ferroelektrische Phasenübergang scheint sich mit zunehmendem Druck verlassen zu erschwachen, was durch die wachsende negative kritische Temperatur erkennbar ist. Zwei theoretische Arbeiten wurden von Mitarbeitern eingebracht.

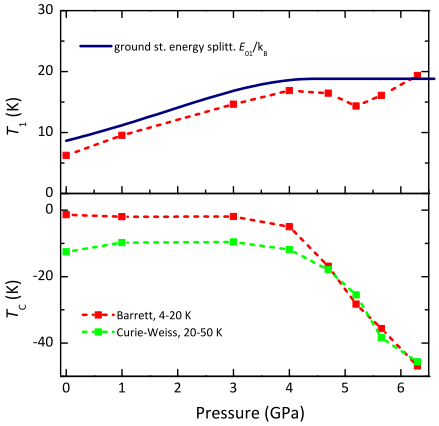

Entwicklung des Quanteneffekts und der kritischen Temperatur in Beryll. Die Sättigung von T_1 tritt jenseits von $P = 4{,}5$ GPa ein, begleitet von einem raschen Anstieg des negativen T_c.

In einer quantenmechanischen Arbeit wurde die Orientierung der Dipole in einem idealen, regelmäßigen, perfekt gefüllten und von Verunreinigungen freien Dreiecksgitter analytisch berechnet. Das Ergebnis deutet auf eine globale ferroelektrische (FE) Ordnung in der Ebene hin, aber auf eine antiferroelektrische (AFE) Ordnung in der Richtung außerhalb der Ebene. Außerdem entwickelt sich bei Vorhandensein von Leerstellen sofort eine Wirbelkonfiguration, die die FE-Ordnung zunichte macht. Es wurde eine Monte-Carlo-Simulation durchgeführt, um die Konfiguration der Dipole im Grundzustand und die entsprechende dielektrische Suszeptibilität mit dem realistischen 30-prozentigen Füllfaktor abzuschätzen. Diese Berechnung bestätigt die Orientierung der kreisförmigen Wirbeldipole um die Leerstellen herum und zeigt eine robuste AFE-Ordnung in der Achse außerhalb der Ebene. Die wachsende negative kritische Temperatur, die bei den Druckmessungen beobachtet wurde, wird auf die aus der Ebene herauswachsende antiferroelektrische Kopplung aufgrund der anisotropen Kompression des Beryllgitters zurückgeführt. In Zukunft ist es ratsam, un-

iaxialen Druck auf wassereinschließenden Beryll zu untersuchen oder auf Materialien mit einem weicherem Gitter und einem stärkerem Lokalisierungspotenzial auszuweichen.

In Kapitel 1 werden die Beweggründe für die Entwicklung eines Hochdruck-HF-Dielektrikums erläutert.

In Kapitel 2 werden die allgemeine Einführung in die dielektrische Theorie und spezifische theoretischen Themen, die in dieser Arbeit behandelt werden, kurz vorgestellt. Der Inhalt Grundlagen der Elektrodynamik, Modelle für Dipolrelaxation, die Klassen der elektrischen Ordnungen und das Leitungsverhalten in Festkörpern.

In Kapitel 3 werden die Hintergründe der beiden Hybridsysteme, Halogenidperowskit und Wasser einschließenden Berylls, zusammengefasst. Ein umfassender Überblick über die Eigenschaften, die aus früheren experimentellen Arbeiten und theoretischen Interpretationen bekannt sind, wird gegeben. Diese Erkenntnisse bilden die Grundlage für die Erwartungen an die druckabhängigen RF-dielektrischen Messungen.

In Kapitel 4 werden das Verfahren und die Überlegungen zur Vorbereitung des DAC-HF-Dielektrikums vorgestellt. Von der Auswahl der Dichtung bis zur Herstellung des Isolierkanals wird jeder Schritt detailliert und mit anschaulichen Grafiken erläutert. Die Charakterisierungsergebnisse, d.h. die Kompensationsdaten, und die Erfolgsbilanz der Druckbeaufschlagung werden ebenfalls dokumentiert. Man sollte in der Lage sein, die Messungen zu reproduzieren, indem man diese Anweisungen befolgt.

In den Kapiteln 5 und 6 werden die experimentellen Daten und Analysen der beiden interessanten Hybridsysteme vorgestellt. Sie sind in ähnlicher Weise aufgebaut, getrennt nach Ergebnissen bei Umgebungsdruck und unter Hochdruck. Gezielte Diskussionen sind in jedem Kapitel hervorgehoben.

In Kapitel 7 werden die Kernaussagen dieser Arbeit kurz und bündig zusammengefasst.

Summary

Radio-frequency (RF) dielectric spectroscopy is a versatile tool for studying molecular motion and ion dynamics in a condensed matter system, meanwhile, physical pressure application is a cultivated technique for engineering lattice structure and fine-tuning material's properties. The combination of these two expertise has achieved remarkable discoveries in complex electronic correlated soft lattice systems, for instance, organic Mott insulators, and induced exotic phases in the quantum regime. Nonetheless, the full utility of pressurized dielectric spectroscopy is being concealed since there remains a vast room for improvement. Back, before the start of this thesis, the in-situ pressurized dielectric setup takes use of piston type pressure cells which has the advantage of meticulousness but ceases at a limited pressure ceiling of 1 GPa. Except for a few very soft organic compounds, for pressure to induce novel states of matter, empirically the magnitude in order of 10 GPa is the prerequisite. To reach this ten-fold improvement, more advanced pressure techniques are required. This thesis set foot on developing the incorporation of diamond anvil cells technique with the existing in-situ cryogenic RF dielectric measurement system, and aimed to improve the pressure limit from the preceding 1 GPa to 10 GPa.

The first part of this thesis documents the considerations and regulated implementation of the diamond anvil cell for dielectric measurement, supplemented with the pressure track record and calibration results. The second part of this thesis consists of investigations on two distinct materials: hybrid

inorganic-organic perovskite and water-confining beryl. The two systems were chosen to testify the suitability and capability of the newly established high pressure dielectric setup.

Diamond anvil cells (DAC) operate as two opposing diamond anvils compressing against the drilled hole of an exceptionally hard gasket from the two opposite sides. The pressure received from the contacting anvil surfaces is distributed evenly over the volume with the filling of pressure medium, *i.e.* low-viscosity medium. The maximum pressure that the cavity can hold is dictated by the hardness of the gasket and tidiness of the wall of the cavity. The former dictates the theoretical limit of pressure and the latter prevents breaching from pressure accumulation. As a reference, diamond anvil cells prepared for optical measurements, *e.g.* X-ray diffraction and infra-red spectroscopy, allow its signal to be transmitted through the diamond anvils and the cavity wall can be made defectless, such that the resulting pressure ceiling reaches as high as 100 GPa.

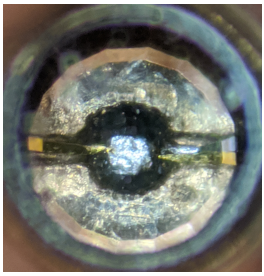

RF dielectric setup in the DAC

On the other hand, dielectric measurement demands breaches on the sealed cavity for the entrances of electrical connections. Furthermore, radio-frequency signals are susceptible to attenuation and thus the electrical connections shall ideally be entirely preserved by coaxial cables. The conflict imposes great technical challenges when developing pressurized dielectric spectroscopy. The solution adapted in this thesis is a slight reconstruction on the hard metallic gasket, which paves an insulated but still hard lane for electrical wires to lay upon, with coaxial cables in closest proximity next to the diamond anvils for minimal wire exposure. Tools such as electric discharge machining are employed for tidy hole-drilling and trench-carving. Heat-treated strong epoxy sets the insulated road. Thin gold wires and platinum strips are used as the electrical connections for small cross-section and thus the least vulnerability for the cavity. Calibrations of the prototype demonstrated the acceptably low stray capacitance and conductance. The pressure ceiling is

proven adequate by the two successful projects.

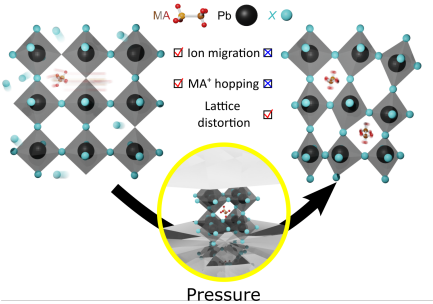

Hybrid perovskite is one of the most anticipated next-generation materials for light-harvesting applications. Its structural stability, ionic conduction and dynamics are found to take influential roles for its performance. Hybrid perovskite possesses the chemical formula of ABX_3, in which A^+ is an organic cation with inorganic B^{2+} and X^- anions. At the beginning of the thesis, the most extensively studied and commercially promising perovskite, methylammonium lead iodide ($CH_3NH_3PbI_3$) faced drawbacks of unstable structure due to lead diffusion and serious ion migration. The innate permanent dipolar methylammonium cation is caged by the PbI_6 tetrahedral network but is free to perform rotation and translation. Equivalently, I^- and even Pb^{2+} ions are eligible for diffusion. For instance, if liquid electrolyte is set upon hybrid perovskite layer, serious dissolution will occur and break the perovskite layer down. Even with replacement of solid carrier transporters, dissolution would still occur in the presence of rich atmospheric moisture.

To solve the hampering issues or search an alternative material, it is necessary to figure out the underlying mechanics responsible for the severe ion migration and the correspondences between the structure and chemical units. The fortes of high pressure radio-frequency dielectric spectroscopy fits well with the presented issues, as ionic propagation and electrical polarization have their signature captured in this frequency domain and the structural factor can be discerned by observing the pressure evolution of relevant material properties. In this work, the three methylammonium lead halides were measured down to cryogenic temperature of 4 K and up to 5 GPa. The full temperature-pressure structural phase diagrams of $CH_3NH_3PbX_3$ (X = I, Br, Cl) were probed and a stabilization of low temperature orthorhombic phase to room temperature is observed in every halide. The frequency dependence of dielectric properties reflects the degrees of ion migration and

slow molecular relaxation. A kHz relaxation has been discovered, which only exist in the low pressure isotropic phase and ceases after the system enters the orthorhombic phase accompanied by a full suppression of ion migration. The negation of both motions indicates an ion delocalization free state, which is favourable for photovoltaic application. Hence, it is concluded that substitution of bulkier cation or smaller halide ion, mimicking the effect of physical pressure, would lead to improved structural stability and enhanced light-harvesting performance.

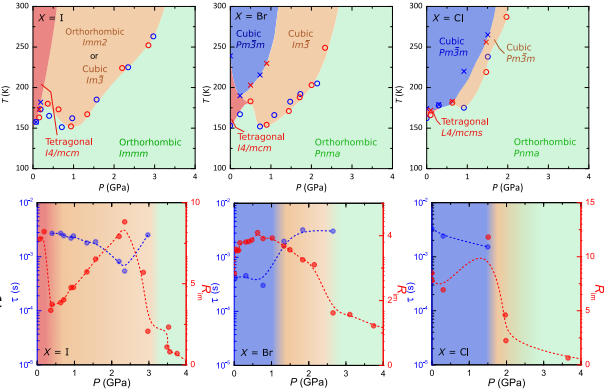

Phase diagrams and evolution of ion motions in $CH_3NH_3PbX_3$ ($X = I, Br, Cl$)

Water molecules possess strong electric dipoles. With their light mass and simple chemical formula, they are ideal for the study of interacting "point" dipoles. However, in free roaming form, their interaction is dominated by the short-range hydrogen bonding. By synthesizing beryl crystals in aqueous environments, water is confined in beryl.

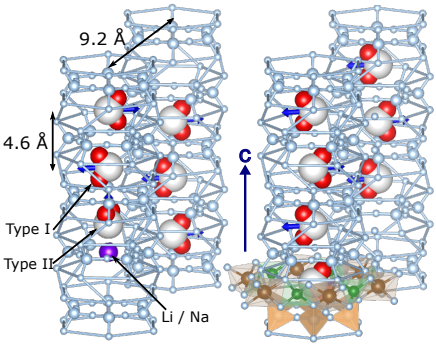

Inside the beryl crystal, water molecules are segregated from hydrogen bonding so pure dipole-dipole interaction is revealed. In other words, a dipolar coupled network is fabricated. Pioneer study has demonstrated the hope of ferroelectric phase transition in this confined water by observation of incipient ferroelectricity, a saturated plateau in real dielectric permittivity at

low temperature, and a ferroelectric soft mode. The prevention of complete charge order is evidenced to originate from the tunnelling between the six-fold azimuthal potential minima of the water dipoles. These prohibitions can potentially be broken through by two approaches: heavy isotope substitution and dipole-dipole coupling strength reinforcement. The former enhances the phonon mode softening and reduces the tunnelling probability. The latter reduces the inter-dipole separation and thus increases the coupling strength in proportion to r^3.

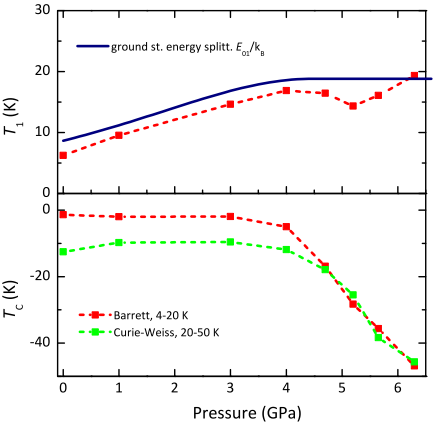

Evolution of quantum effect and critical temperature in beryl. Saturation of T_1 occurs beyond $P = 4.5\,GPa$, accompanied by rapid growth in negative T_c.

In this work, H_2O- and D_2O-filled beryls were pressurized up to 7 GPa and measured down to 4 K. The robustness of quantum fluctuations and the distance from phase transitions are entailed by the characteristic plateau in the real dielectric permittivity. The results have confirmed the benefits of mass enhancement of the dipoles, as the saturation develops at lower temperature in beryl filled with heavy water. Application of pressure leads to a progressively enhanced and eventually saturated quantum effect, which is modelled by suppression of a localization potential barrier, as evidenced by an energy estimation of free rotating water dipole. The ferroelectric phase transition recedes as pressure is applied, indicated by the growing negative critical temperature. Two theoretical works were contributed by collaborators. A quantum mechanical treatment analytically calculated the dipoles orientation in ideal, regular, perfectly-filled and impurity-free triangular lattice. The result suggests global ferroelectric (FE) order in the plane, but antiferroelectric (AFE) order in the out of plane direction. Additionally, in the presence of vacancies, vortex configuration immediately develops and

ruins the FE order. Monte Carlo simulations are performed to estimate the ground state dipoles configuration and corresponding dielectric susceptibility with the realistic 30% filling factor. This computation corroborates the vortex circular dipoles orientation around vacancies and reveals robust AFE order in the out-of-plane axis. The growing negative critical temperature observed in the pressure measurements is attributed to the outgrowing out-of-plane antiferroelectric coupling due to anisotropic compression of the beryl lattice. In the future, it is advised to study uniaxial pressure on water-confining beryl or switch to materials with softer lattice and stronger localizing potential.

In chapter 1, the motivations for developing a high pressure RF dielectric setup is explained.

In chapter 2, the general introduction of dielectric theory and specific theoretical topics covered in this thesis are briefly presented. The content includes basic electrodynamics, models for dipole relaxation, the classes of electric orders and conducting behaviours in solids.

In chapter 3, the background of the two hybrid systems, halide perovskite and water-confining beryl, are summarized. A comprehensive overview of the properties reported from preceding experimental works and theoretical interpretations is given. These findings set the foundation for the expectations towards the pressurized RF-dielectric measurements.

In chapter 4, the procedure and consideration of preparation for DAC RF dielectric measurements are presented. From the selection of gasket to the creation of insulating channels, each step is explained in detail with illustrating graphics . The characterization results, *i.e.* the compensation data, and the track record of pressurization are also documented. One should be able to replicate the measurement by following these instructions.

In chapters 5 and 6, the experimental data and analysis of the two hybrid systems of interests are presented. They are structured in similar manners, separated from ambient pressure and under pressure results. Focused discussions are highlighted in each chapter.

In chapter 7, the essences of this thesis are concisely concluded.

Publications

Publications presented in this thesis:

- **Yuk Tai Chan**, Natanja Elliger, Berina Klis, Márton Kollár, Endre Horváth, László Forró, Martin Dressel, Ece Uykur, *Realization of ion migration free $CH_3NH_3PbX_3$ (X = I, Br and Cl) perovskite structure under high pressure*. Submitted to Adv. Sci..
- **Yuk Tai Chan**, Ece Uykur, Martin Dressel, Veniamin A. Abalmasov, Thomas Victor, Elena S. Zhukova, Mikhail A. Belyanchikov, Boris Gorshunov, *Effect of hydrostatic pressure on the quantum paraelectric state of dipolar coupled water molecular network*. Submitted to Phys. Rev. Res..

Not presented in this thesis:

- **Yuk Tai Chan**, Seulki Roh, Soohyeon Shin, Tuson Park, Martin Dressel, Ece Uykur, *Three-dimensional hopping conduction triggered by magnetic ordering in the quasi-one-dimensional iron-ladder compounds $BaFe_2S_3$ and $BaFe_2Se_3$*. Phys. Rev. B. **102**, 035120 (2020)

List of abbreviations

Abbreviation	Meaning
PE	Paraelectricity / paraelectric
FE	Ferroelectricity / ferroelectric
AFE	Antiferroelectricity / antiferroelectric
QPE	Quantum paraelectricity
QCP	Quantum critical point
TO	transverse-optical
ND	Neutron diffraction
XRD	X-ray diffraction
INS	Inelastic neutron scattering
FTIR	Fourier-transform infrared spectroscopy
HOIP	Hybrid organic-inorganic halide perovskite
MA	Methylammonium $CH_3NH_3^+$
FA	Formamidinium $NH_2CHNH_2^+$
MAPX	$CH_3NH_3PbX_3$
MAPI	$CH_3NH_3PbI_3$
MAPB	$CH_3NH_3PbBr_3$
MAPC	$CH_3NH_3PbCl_3$
Beryl	$Be_3Al_2Si_6O_{18}$
Beryl-H(D)	$H_2O(D_2O)$-confining beryl

Water-I(II)	Type-I(II) water dipole's orientation when confined in beryl crystal
DC / AC	Direct current; frequency $f = 0$ / Alternating current; frequency $f > 0$
RF	Radio-frequency
DAC	Diamond anvil cell
DAC-dielectric	The incorporated setup of dielectric spectroscopy with DAC
EDM	Electrical discharge machining

Contents

1 Motivation 22

2 Theoretical overview 25
2.1 Definitions . . . 25
2.1.1 Dimensionality of system . . . 26
2.2 Polarizations in matters . . . 27
2.2.1 Mechanisms . . . 27
2.2.2 Debye model . . . 28
2.3 Modifications from Debye model . . . 31
2.3.1 Cole-Cole . . . 31
2.3.2 Cole-Davidson . . . 32
2.3.3 Havriliak-Negami . . . 33
2.4 Activation of polarization modes . . . 34
2.5 Classes of dielectric phases . . . 35
2.5.1 Piezoelectricity . . . 36
2.5.2 Pyroelectricity . . . 37
2.5.3 Ferroelectricity . . . 38
2.5.4 Quantum paraelectricity . . . 41
2.6 Conduction in solids . . . 52
2.6.1 Hopping . . . 52
2.6.2 Ion migration . . . 53

3 Background 56
3.1 Hybrid halide perovskite . . . 56
3.1.1 Motivations . . . 57
3.1.2 Crystal structure of $CH_3NH_3PbX_3$ (X = I, Br or Cl) . . . 58
3.1.3 Ion migration in $CH_3NH_3PbX_3$ (X = I, Br or Cl) . . . 64
3.1.4 $CH_3NH_3^+$ cation motion in $CH_3NH_3PbX_3$ (X = I, Br or Cl) . . . 67
3.2 Confined water . . . 71
3.2.1 Beryl . . . 71

4 Experimental Methods 80
4.1 Ambient pressure . . . 80
4.1.1 Compensations . . . 81
4.1.2 Intensive physical quantities calculation . . . 84
4.2 Under pressure . . . 86
4.2.1 Diamond anvil cells (DAC) . . . 86
4.2.2 Gasket preparation . . . 91
4.2.3 Cell filling and closure . . . 95
4.2.4 Pressure determination . . . 96
4.2.5 Setup characterisation . . . 97

5 Hybrid perovskite $CH_3NH_3PbX_3$ (X = I, Br, Cl) 102
5.1 Sample preparations . . . 102
5.2 Dielectric properties of MAPX at ambient pressure . . . 103
5.2.1 $CH_3NH_3PbBr_3$ (MAPB) . . . 103
5.2.2 $CH_3NH_3PbCl_3$ (MAPC) . . . 104
5.2.3 $CH_3NH_3PbI_3$ (MAPI) . . . 104
5.2.4 Expectations towards MAPX under pressure . . . 106
5.3 Dielectric properties of MAPX under pressure . . . 108
5.3.1 $CH_3NH_3PbI_3$ (MAPI) . . . 108
5.3.2 $CH_3NH_3PbBr_3$ (MAPB) . . . 110
5.3.3 $CH_3NH_3PbCl_3$ (MAPC) . . . 112

5.4 Focused discussions . . . 114
5.4.1 Structure of MAPX under pressure . . . 114
5.4.2 Ion migration in MAPX under pressure . . . 117
5.4.3 Disappearence of kHz relaxation in MAPX under pressure . . . 120
5.4.4 Validity of amorphization . . . 122
5.4.5 Effect of pressure cycle on MAPX . . . 125
5.5 Conclusion . . . 127

6 Confined water 129
6.1 Sample preparations . . . 129
6.2 Ambient pressure . . . 130
6.2.1 Hysteresis . . . 131
6.2.2 Effect of D_2O substitution . . . 131
6.2.3 Effect of type-II water concentration . . . 132
6.3 Effect of physical pressure . . . 134
6.3.1 Extrinsic effects . . . 135
6.3.2 H_2O-beryl . . . 136
6.3.3 D_2O-beryl . . . 139
6.3.4 Refined D_2O-beryl . . . 141
6.4 Theoretical interpretation . . . 145
6.5 Conclusion . . . 149

7 Conclusion 152
7.1 DAC-dielectric establishment . . . 152
7.2 Hybrid perovskite $CH_3NH_3PbX_3$ . . . 153
7.3 Water-confining beryl . . . 155

Bibliography 159

Chapter 1

Motivation

Correlated electron condensed matter systems encompass all sorts of compounds that exhibit exotic and fascinating electrical and magnetic properties due to the interplay between the electric or magnetic units and the structural configuration, and can not be described solely in terms of non-interacting entities. Phenomena such as superconductivity, heavy fermionic behavior, metal-insulator transition and multiferroics are repeatedly discovered in complex materials. Every experimental (and theoretical) means available is agilely endeavoured to gain insights into the enigma of the underlying mechanism. Prestigious techniques like angle-resolved photoemission spectroscopy, Raman spectroscopy, inelastic neutron scattering, x-ray spectroscopy and high precision transport measurement have all been employed, but, till today, most of the reputed complex systems remain mysterious. It is natural for the community to look for new aspects of information, *i.e.* new experimental techniques, to excite new ideas.

The secret of the enigma may be laying on the collective behaviour which cannot be resolved by microscopic experiments, as one has seen that new physics emerges from isolated elementary particles to condensed matter systems [1]. The global orders, long-range coupling and domains correlations

in the systems are also necessary to be examined.

These objectives fall right into the expertises of radio-frequency dielectric spectroscopy. Radio-frequency (RF) dielectric spectroscopy measures the macroscopic polarization and conduction, and it entails the collective responses of electric dipoles upon external varying electric voltage. Its excellency in probing electric orders has been proven in distinguished works, for instance, discovering the charge order domain wall motions in 2D organic conductor α-(BEDT-TTF)$_2$I$_3$ [2], [3] and discerning relaxor ferroelectricity in spinel compound $CdCr_2S_4$ [4] and Mott insulator κ-(BEDT-TTF)$_2$Cu[N(CN)$_2$]Cl [5].

The structure takes a crucial role in realizing peculiar collective conditions; for example, a frustrated magnet due to equivalent triangular lattice leads to realization of spin liquid [6] and charge order or disproportionation due to broken symmetry [7], [8]. To effectively discern the pure effect of structure, physical pressure application is undoubtedly the tool since it can alter the lattice constant on the same piece of specimen for an extended range without introduction of chemical impurity or defects.

Roland Rösslhuber, the predecessor of the author in our institution, has achieved the astounding composition of a generic phase diagram for genuine Mott insulator [9], [10] with the help of pressurized RF dielectric spectroscopy, as it provides the detailed evolution of insulator-metal transition upon pressure application. This is a well-deserved hard, but also fortuitous, work, since organic compounds are one of the most malleable groups of compounds and a pressure ceiling of 1 GPa is able to cover a rich phase diagram. There are plenty of pending materials classes that could be benefited from pressurized dielectric spectroscopy but demands a strong pressure in the order of 10 GPa.

When a higher pressure ceiling is available, yearned studies of two compounds will finally be enabled: hybrid organic-inorganic halide perovskite and water-confining beryl. Both compounds are hybrid systems in which strong polar ions are caged by neighbouring ions but preserve a high degree of freedom for motions.

Hybrid organic-inorganic halide perovskite (HOIP) earns its reputation

for being the most viable next-generation light-harvesting material. Its low cost, variety of composition, and defect-tolerant efficiency allow HOIP to gradually take over silicon in industrial production. Regardless, the replacement of HOIP is not yet perfect. The commercial HOIP solar cell, made of methylammonium lead iodide, is facing drawbacks of poor structural stability and thus short longevity and environmental concerns [11]–[13]. The degradation originates from the severe ion migration, which also generates pronoun characteristic stoichiometric polarization. On the other hand, literature reported structural transitions and amorphization of HOIP at a pressure above 5 GPa. Such that, pressurized RF dielectric spectroscopy up to 10 GPa can examine the relationship between structure and the ion migration and guide the selection of chemical composition.

Water-confining beryl is a dipolar coupled water network in which water molecules are spatially segregated away from short-range hydrogen bonding and long-range dipole-dipole interaction is revealed. The pioneering study uncovered incipient ferroelectricity in beryl [14] and the prohibition is evidenced to be the quantum tunnelling between the azimuthal potential minima. In order to suppress the tunnelling effect and settle down the dipoles for stable orders, one feasible approach is a reinforcement of dipole-dipole coupling by reducing the spatial separation of water molecules. The evolution of the quantum effect and the development of electric order can be clearly identified in RF dielectric spectra as well.

These two systems promise great potential in both technological advancements and fundamental scientific enrichment that are hidden in extreme, high pressure and low cryogenic temperature, conditions. Inspired by the need and incentivized by the rewards of a technical breakthrough, this thesis embarked on the development of diamond anvil cells, the frontier pressurization tool at the moment, with the existing cryogenic RF dielectric setup and set goal to improve the pressure ceiling to 10 GPa and perform high pressure RF dielectric measurements in very low temperature.

Chapter 2

Theoretical overview

'In dielectric, by contrast, all charges are attached to specific atoms or molecules - they're on a tight leash, and all they can do is move a bit within the atom or molecule. Such microscopic displacements are not as dramatic as the wholesale rearrangement of charge in a conductor, but their cumulative effects account for the characteristic behaviour of dielectric materials.' - a quota from David J. Griffiths's book *Introduction to electrodynamic* [15]. These cumulative effects of microscopic displacements of individual dielectric materials are characterized by the physical quantity - dielectric permittivity.

Dependences of dielectric permittivity thus reflect every electrical aspect of the matter, from microscopic details such as the displacement of electrons and the dynamics of charged ions, to macroscopic properties such as the geometric orders in lattice and the presence of domains.

2.1 Definitions

When an external electric field $\boldsymbol{E}_{\text{ext}}$ is applied onto dielectric materials, polarizations $\boldsymbol{P}$ are induced. Trickily, induced $\boldsymbol{P}$ will produce its own electric field and trigger the change in the $\boldsymbol{P}$ of neighbouring dipoles, which initiates

the cycle again. We can not help but alternatively, which is actually even better, we can jump out of this infinite loop, consider only the equilibrium situation and root the discussion directly from the total electric field $\boldsymbol{E}$, which is the collective result contributed by the $\boldsymbol{E}_{\text{ext}}$, the free charges and $\boldsymbol{P}$.

Providing that $\boldsymbol{E}$ is not too strong, which can ionize the electrons and the relationship is linear, one can write:

$$\boldsymbol{P} = \varepsilon_0 \chi_e \boldsymbol{E} \tag{2.1}$$

where ε_0 is the permittivity of free space and χ_e is the electric susceptibility of the material. χ_e is the quantity which characterises the extent of polarizations of every material. Alternatively, by rearranging the equations, other parameters are introduced which contain the exact information as χ_e. As in linear media:

$$\boldsymbol{D} = \varepsilon_0 \boldsymbol{E} + \boldsymbol{P} = \varepsilon_0 (1 + \chi_e) \boldsymbol{E} \tag{2.2}$$

$$= \varepsilon_r \varepsilon_0 \boldsymbol{E} = \varepsilon \boldsymbol{E} \tag{2.3}$$

where $\boldsymbol{D}$ is the electric displacement, ε_r and ε are the relative permittivity and dielectric permittivity of the material, respectively. All three quantities, χ_e, ε_r and ε carry the same information regarding the response to the external electric field of the material. However, conventionally, ε_r is adapted in the reports of dielectric research (as you shall see in the later sections of this thesis) because it is dimensionless.

2.1.1 Dimensionality of system

Given that the structure of matters may not be isotropic and could be consisted of multiple elements each with its own polarizability, induced polarizations may have direction-dependence[1]. Therefore, to characterise the polarizations of matters, ε is expressed in the form of tensor. In the case

[1] Worth noting, $\boldsymbol{P}$ in molecules could point to any direction, instead of aligning with $\boldsymbol{E}_{\text{ext}}$

of 3-dimensional space, eqn. 2.3 becomes:

$$\boldsymbol{D} = \begin{vmatrix} \varepsilon_{xx} & \varepsilon_{xy} & \varepsilon_{xz} \\ \varepsilon_{yx} & \varepsilon_{yy} & \varepsilon_{yz} \\ \varepsilon_{zx} & \varepsilon_{zy} & \varepsilon_{zz} \end{vmatrix} \boldsymbol{E} \tag{2.4}$$

Via insightful choices of the principal axes, the off-diagonal terms could be tuned and vanish, which thereby simplifies eqn. 2.4 to:

$$\boldsymbol{D} = \begin{vmatrix} \varepsilon_{xx} & 0 & 0 \\ 0 & \varepsilon_{yy} & 0 \\ 0 & 0 & \varepsilon_{zz} \end{vmatrix} \boldsymbol{E} \tag{2.5}$$

Note that the principal axes diagonalizing the real part of the dielectric tensor are not always shared with the imaginary part. Nonetheless, they often coincide for high symmetry crystal structure [16].

As suggested here, to completely characterise the dielectric permittivity of a matter in our 3-D world, three parameters ε_{ii} are demanded to be determined. Therefore, a complete determination is fulfilled by a set of measurements at all three crystallographic axes.

2.2 Polarizations in matters

Matters are composed of a sea of atoms or tightly bounded molecules, uniformly distributed or not. Polarizations take place onto each individual atoms and molecules. The overall dielectric response of a matter is not simply the accumulation of local polarizations but has undergone complicated interactions between every individual.

2.2.1 Mechanisms

Depending on the bounding strength and effective masses, every instance of polarizations from different mechanisms possesses a characteristic timescale (resonance / relaxation), and correspondingly would exhibit fea-

tures at different frequency ranges. Figure 2.1 illustrates the schematic exhibition of all mechanisms in a wide frequency range measurement. In the following, those mechanisms are listed in order of the characteristic frequency, from high to low:

Electronic polarization is the separation of the positive core (nucleus) and the negative electron cloud of an atom under the influence of $\boldsymbol{E}_{\text{ext}}$, which takes place at every atom. A dipole moment is set up, which connects the centres of the displaced electron cloud and the nucleus .

Ionic polarization refers to the separation of the positive cations and negative anions of a molecule. Dipole moment is induced between the displaced positive and negative ions for non-polar molecules; dipole moment is either enhanced or suppressed, depending on the alignment with $\boldsymbol{E}_{\text{ext}}$, for polar molecules.

Dipolar / Orientational polarization describes the reorientation process of the permanent dipoles of polar molecules (or induced molecular dipoles) after being subjected into $\boldsymbol{E}_{\text{ext}}$. The innate dipole moment of the molecule $\boldsymbol{p}$ in $\boldsymbol{E}_{\text{ext}}$ experiences a torque:

$$\boldsymbol{N} = \boldsymbol{p} \times \boldsymbol{E} \tag{2.6}$$

and thereby, the dipole moment is rotated towards the direction of $\boldsymbol{E}_{\text{ext}}$.[1]

Interfacial / electrode polarization (a.k.a. Maxwell–Wagner–Sillars polarization) is the resultant of charges accumulation on interfaces [17], [18].

2.2.2 Debye model

The orientational polarization of electric dipoles is first modelled by Debye [20]. Under an external voltage, dipoles are forced to reorient and aligned antiparallelly with the voltage direction. If the voltage is switched off, dipoles are relaxed back to their original orientation. The reorientation of the dipole is not instantaneous but takes a characteristic relaxation time τ (equivalently,

[1] If there is a background electric potential, which is usually the case, the dipole moment of the molecule will not be aligned with $\boldsymbol{E}_{\text{ext}}$, but the rotation is always triggered.

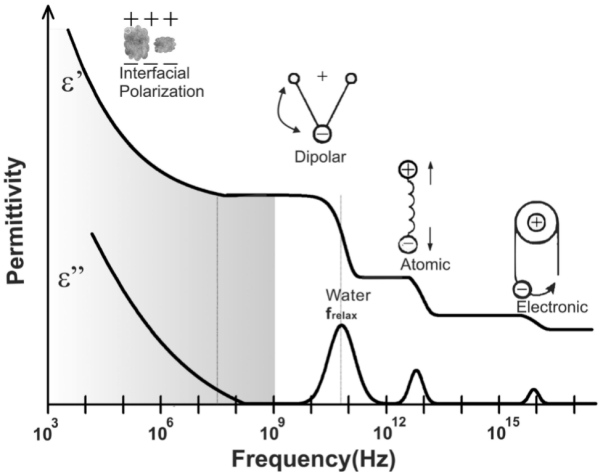

Figure 2.1: Schematic illustration of the frequency dependence of dielectric permittivity contributed by different mechanisms, reproduced from ref. [19]
.

it is the alignment time when the voltage is switched on). Thus, the decay of induced polarization in the voltage direction $P(t)$ is given by:

$$\frac{dP(t)}{dt} = -\frac{1}{\tau}P(t)$$
$$P(t) = P_0 \exp\left(-\frac{t}{\tau}\right) \tag{2.7}$$

In case of a static voltage (DC) or an AC voltage with the period much larger than τ, a complete reorientation is achieved and the dielectric permittivity ε is maximum and labelled as ε_s. On the other hand, if the period of the AC voltage is much shorter than τ, and dipoles fail to catch up or align, so orientational polarization will be absent from ε and is labelled as ε_∞ [1]. Thus, the frequency spectrum of ε is expressed in:

$$\varepsilon(\omega) = \varepsilon_\infty + f(\omega) \tag{2.8}$$

[1] Faster mechanics, namely ionic, atomic and electronic polarizations are present.

$f(\omega)$ corresponds to the Fourier transformation of $P(t)$.

$$f(\omega) = K\int_0^\infty P(t)e^{i\omega t}dt$$
$$= \frac{KP_0}{-i\omega + 1/\tau} \tag{2.9}$$

The product of constants K and P_0 can be represented by τ and the two frequency limits of ε.

$$KP_0 = f(\omega = 0)(-i(0) + 1/\tau)$$
$$= (\varepsilon_s - \varepsilon_\infty)/\tau \tag{2.10}$$

Thus,

$$\varepsilon(\omega) = \varepsilon' + i\varepsilon'' = \varepsilon_\infty + \frac{\varepsilon_s - \varepsilon_\infty}{1 - i\omega\tau} \tag{2.11}$$

decomposing into real and imaginary permittivity gives

$$\varepsilon'(\omega) = \varepsilon_\infty + \frac{\varepsilon_s - \varepsilon_\infty}{1 + \omega^2\tau^2} \tag{2.12}$$

$$\varepsilon''(\omega) = \frac{(\varepsilon_s - \varepsilon_\infty)\omega\tau}{1 + \omega^2\tau^2} \tag{2.13}$$

The frequency spectra of ε' and ε'' are schematically plotted in fig. 2.2. A characteristic step and peak features are exhibited at τ respectively, which illustrate the failure of polarization beyond τ and maximized absorption at τ of the reorientating dipoles.

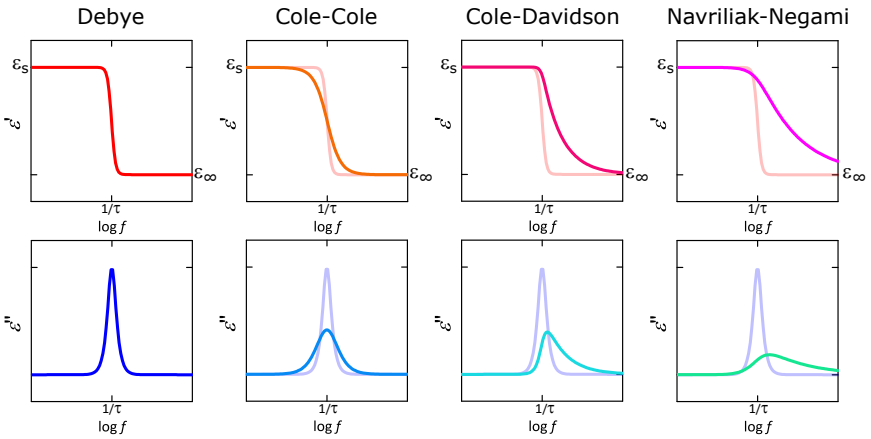

Figure 2.2: Schematic illustration of the Debye model and its empirical modifications.

2.3 Modifications from Debye model

Debye model considers homogeneous dipoles described by a Lorentz . In condensed matter systems, multiple molecular dipoles could present and the dipole-dipole interaction should be included, so the Debye model is not expected to be a satisfactory description of actual systems. A couple of modifications are adapted to capture the deviation. Comparison between each of the modifications with Debye model is depicted in fig. 2.2.

2.3.1 Cole-Cole

Cole-cole equation is a symmetric broadened version of the Debye equation (given by K.S. Cole and R.H. Cole in 1941). The symmetric broadening is captured by the factor α in the exponent of ω at the denominator.

$$\varepsilon^*(\omega) = \varepsilon_\infty + \frac{\varepsilon_s - \varepsilon_\infty}{1 + (i\omega\tau)^{1-\alpha}} \qquad [0 \leq \alpha \leq 1] \tag{2.14}$$

Real and imaginary parts correspondingly become

$$\varepsilon'(\omega) = \varepsilon_\infty + (\varepsilon_s - \varepsilon_\infty)\frac{1 + (\omega\tau)^{1-\alpha}\sin(\alpha\pi/2)}{1 + 2(\omega\tau)^{1-\alpha}\sin(\alpha\tau/2) + (\omega\tau)^{1-\alpha}} \tag{2.15}$$

$$\varepsilon''(\omega) = (\varepsilon_s - \varepsilon_\infty)\frac{(\omega\tau)^{1-\alpha}\cos(\alpha\pi/2)}{1 + 2(\omega\tau)^{1-\alpha}\sin(\alpha\tau/2) + (\omega\tau)^{1-\alpha}} \tag{2.16}$$

Cole-Cole equation reduces to the Debye equation for $\alpha = 0$.

Symmetric broadening of relaxation features occurs unless all vibration modes in the speciman are synchronized. Presences of defects, domain walls, or inhomogeneous distortions will create various local environment for the dipoles and disperse the relaxation times which leads to symmetric broadening. For example, in α-(BEDT-TTF)$_2$I$_3$, two domain wall pairs are formed and their RF relaxations are descripted by Cole-Cole equation with two distinct modes [3].

2.3.2 Cole-Davidson

Cole-Davidson equation is an asymmetric broadened version of the Debye equation. The asymmetric broadening is captured by the factor β in the exponent of the whole denominator.

$$\varepsilon^*(\omega) = \varepsilon_\infty + \frac{\varepsilon_s - \varepsilon_\infty}{(1 + i\omega\tau)^\beta} \qquad [0 \leq \beta \leq 1] \tag{2.17}$$

Real and imaginary parts correspondingly become

$$\begin{aligned}\varepsilon'(\omega) &= \varepsilon_\infty + (\varepsilon_s - \varepsilon_\infty)\cos^\beta(\varphi)\cos(\beta\varphi) \\ &= \varepsilon_\infty + \frac{(\varepsilon_s - \varepsilon_\infty)\cos(\beta\varphi)}{(1 + \omega^2\tau^2)^{\beta/2}}\end{aligned} \tag{2.18}$$

$$\begin{aligned}\varepsilon''(\omega) &= (\varepsilon_s - \varepsilon_\infty)\cos^\beta(\varphi)\sin(\beta\varphi) \\ &= \frac{(\varepsilon_s - \varepsilon_\infty)\sin(\beta\varphi)}{(1 + \omega^2\tau^2)^{\beta/2}}\end{aligned} \tag{2.19}$$

$$\text{with} \qquad \varphi = \tan^{-1}(\omega\tau)$$

Cole-Davidson equation reduces to the Debye equation for $\beta = 1$.

Stimulated by the generalization of Cole-Cole equation, which includes symmetric broadening of relaxation peaks, Cole-Davidson equation is the alike generalization but covers asymmetric features instead. The asymmetric broadening is the characteristic feature of the Fourier transform of the stretched exponential function [21], however an exclusive corresponding physical origin is lacked. In practice, the more generalized Havriliak-Negami equation is preferred for sole empirical approximation.

2.3.3 Havriliak-Negami

Havriliak-Negami equation, combining Cole-Cole and Cole-Davidson equations, is a both symmetric and asymmetric version of the Debye equation.

$$\varepsilon^*(\omega) = \varepsilon_\infty + \frac{\varepsilon_s - \varepsilon_\infty}{(1 + (i\omega\tau)^{1-\alpha})^\beta} \qquad [0 \leq \alpha, \beta \leq 1] \tag{2.20}$$

Real and imaginary parts correspondingly become

$$\varepsilon'(\omega) = \varepsilon_\infty + (\varepsilon_s - \varepsilon_\infty)\frac{\cos(\beta\varphi)}{[1 + 2(\omega\tau)^{1-\alpha}\sin(\alpha\pi/2) + (\omega\tau)^{2(1-\alpha)}]^{\beta/2}} \tag{2.21}$$

$$\varepsilon''(\omega) = (\varepsilon_s - \varepsilon_\infty)\frac{\sin(\beta\varphi)}{[1 + 2(\omega\tau)^{1-\alpha}\sin(\alpha\pi/2) + (\omega\tau)^{2(1-\alpha)}]^{\beta/2}} \tag{2.22}$$

$$\text{with} \qquad \varphi = \tan^{-1}\frac{(\omega\tau)^{1-\alpha}\cos(\pi\alpha/2)}{1 + (\omega\tau)^{1-\alpha}\sin(\pi\alpha/2)}$$

Havriliak-Negami equation reduces to Cole-Davidson and Cole-Cole equations for $\alpha = 0$ and $\beta = 1$ respectively.

Havriliak-Negami equation captures the largest degree of deviation from simplest Debye's conjesture, and is primarily used for descripting complex dynamics, for example, the excess wing feature observed in the relaxation behaviour of glycerol [22].

2.4 Activation of polarization modes

The freedom of motion responsible for local polarization is not an innate property but an activated behaviour and its degree of freedom is characterised by the relaxation time τ.

Arrhenius

Arrhenius activation refers to the thermal activation. The corresponding dipoles are excited by thermal energy and are able to vibrate or be displaced by the application of $\vec{E}$ freely. The temperature dependence of the relaxation time follows the Arrhenius equation [23]:

$$\tau(T) = \tau_0 \exp\left(\frac{U}{k_B T}\right) \tag{2.23}$$

$$\ln \tau(T) = \frac{U}{k_B T} + \ln(\tau_0) \tag{2.24}$$

where U is the activation energy barrier, *e.g.* energy barrier between two adjacent potential wells.

Following Arrhenius behaviour, as arranged in eqn. 2.24 and depicted in fig. 2.3(a), τ will display a linear dependence to $1/T$ with a slope of U/k_B when plotted in logarithmic scales.

Vogel-Fulcher-Tammann (VFT)

Often, deviations from Arrhenius behaviour are observed. A common deviation is captured by the VFT equation, an empirical parameterization with the introduction of a shift in divergence temperature to T_{VF} (fig. 2.3(b)) [23].

$$\tau(T) = \tau_0 \exp(\frac{B}{k_B(T - T_{\mathrm{VF})}}) \tag{2.25}$$

$$\ln \tau(T) = \frac{B}{k_B}\left(\frac{1}{T - T_{\mathrm{VF}}}\right) + \ln(\tau_0) \tag{2.26}$$

where B is an empirical constant that could practically be interpreted as the activation energy U.

VFT equation is found to be a successful parameterization of the freezing out of dipolar motions at finite temperature, *e.g.* glasses [22], order-disorder

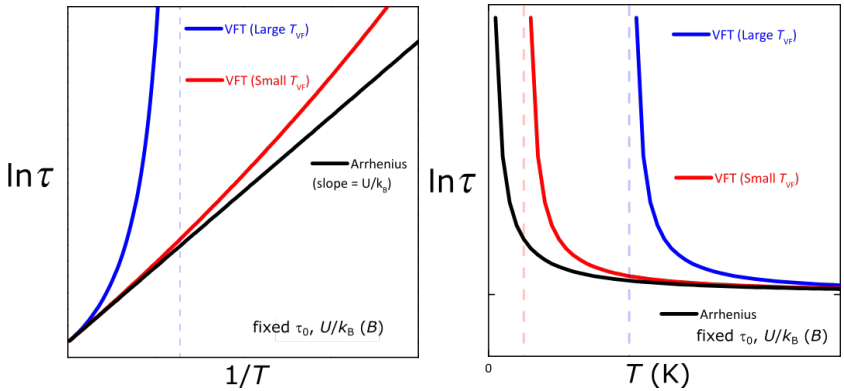

Figure 2.3: A schematic illustration of the temperature dependence of τ exhibiting Arrhenius (black) and VFT (red and blue) behaviours.

ferroelectrics (*c.f.* sec. 2.5.3), relaxor ferroelectric [24] and some organic charge-transfer salts [25]. The presence of T_{VF} can, in general, be interpreted as an indicator of a phase with fixated dipole polarization at a low temperature whose transition temperature shall be, but not necessarily be, close to the T_{VF}.

2.5 Classes of dielectric phases

"Dielectric"[1], by definition, embodies any system exhibiting high polarizability and low electrical conduction. Although the definition does not impose, the coexistence of high relative permittivity and low conductivity is mostly realised in systems possessing inherent molecular electric dipoles.

In a lattice populated by molecular dipoles, depending on the ordering among the dipoles, substantially different physical phenomena could be hosted. Considering the individual physical significance and differentiability,

[1]The term "dielectric" was formed from "dia" + "electric", describing the antiparallel alignment of induced dipoles to the applied electric field.

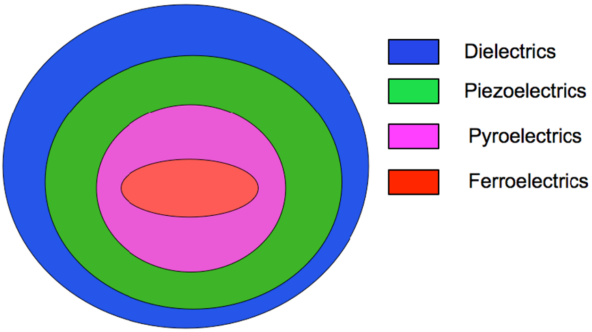

Figure 2.4: Venn diagram indicating graphically the relationship between ferroelectrics, pyroelectrics, piezoelectrics and dielectrics reproduced from ref. [26].

several subclasses have diverged. The relationship between those subclasses is depicted with a Venn diagram in fig. 2.4.

2.5.1 Piezoelectricity

"Piezo" is derived from a Greek word, "piezein", meaning pressure. Piezoelectricity is the phenomenon of polarization is generated by an applied mechanical stress and vice versa.

For any molecular polarization to be induced, the crystals have to be non-centrosymmetric (fig. 2.5), which is found in 21 out of all 32-point groups. 1 out of the 21-point groups, the point group no. 432, has other combined symmetry elements. The remaining 20-point groups are eligible for piezoelectricity. Examples are GeTe, $SrAlF_5$, SbSI, etc [27].

Due to its special electrical-to-mechanical conversion property, piezoelectric crystals are found in devices such as stabilized oscillators, transducers, acoustic amplifiers, etc. Remarkable applications include sonar, cellular radio, automotive radar, etc [28].

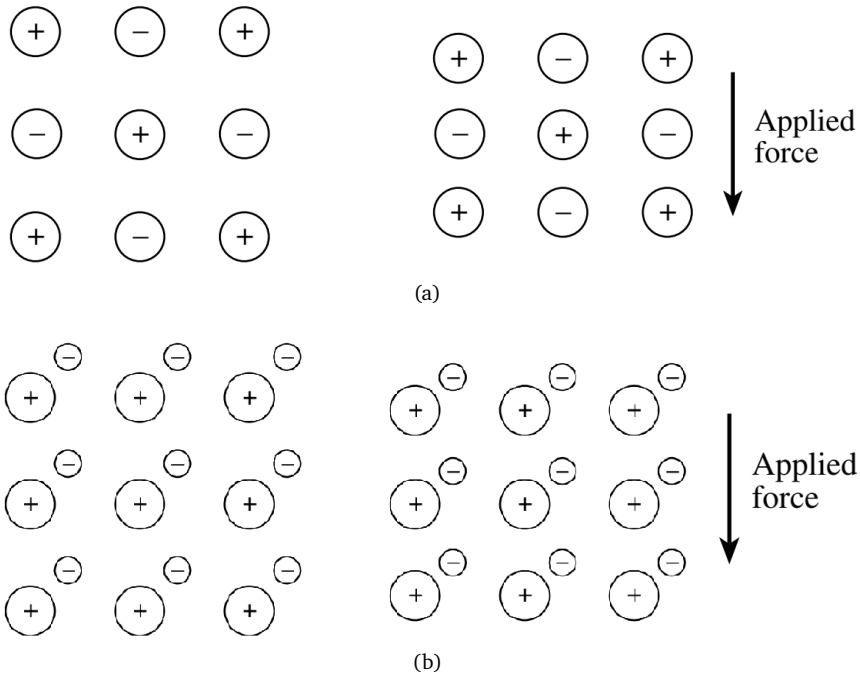

Figure 2.5: Schematic illustrations of a crystal structure (a) with and (b) without centrosymmetry. When being subjected to force (or pressure), only the non-centrosymmetric system is possible to host induced polarization. Pictures are borrowed from ref. [20].

2.5.2 Pyroelectricity

10 out of the 20 piezoelectric point groups are polar; namely, they possess spontaneous polarization without the need for any excitation, and they are further classified as pyroelectricity. "Pyro" means "heat" in Greek since the inherent electrical dipoles were first observed to be generated by the change in temperature [28].

2.5.3 Ferroelectricity

Ferroelectricity (FE) is an analogy to ferromagnetism (FM), where "ferro" is derived from "ferrum," meaning iron in Latin, as iron is the first found ferromagnetic material historically. Analogous to reversible magnetisation in ferromagnetics, a pyroelectric is categorised as ferroelectric if it exhibits reversible (or more generally, switchable) electric polarization.

Properties of FE in analogies with FM [28]:

- The spontaneous polarization P_s occurs below the Curie-Weiss temperature T_C. Above T_C, the material is in a paraelectric state and its permittivity follow Curie-Weiss law [29].

$$\varepsilon_r = \frac{C}{T - T_c} \tag{2.27}$$

  where C is the Curie(-Weiss) constant.

- To minimize depolarizing fields macroscopically, P_s is not uniaxial over the whole crystal, but domains with different orientations of P_s are formed.

- The electric field dependence of the dielectric displacement $P(E)$ is highly nonlinear, and a characteristic hysteresis loop [1] is exhibited (fig. 2.6).

Despite a handful amount of similarities in their exhibitions, ferroelectricity and ferromagnetism are different at the fundamental level. The differences between the two systems are summarised in fig. 2.7. The fundamental difference is that there is no electrical counter-part to the atomic spin and thus the origin of the dipole is the separation of charges. As the formation of electric dipole demands displacement of atoms or ions, henceforth, a structural modulation or distortion always accompanies the emergence of ferroelectricity.

[1] Hysteresis loop does not guarantee FE. For examples, electrets, due to mobile charged defects, and pn-junctions, due to charge depletion, also exhibit hystersis [27]

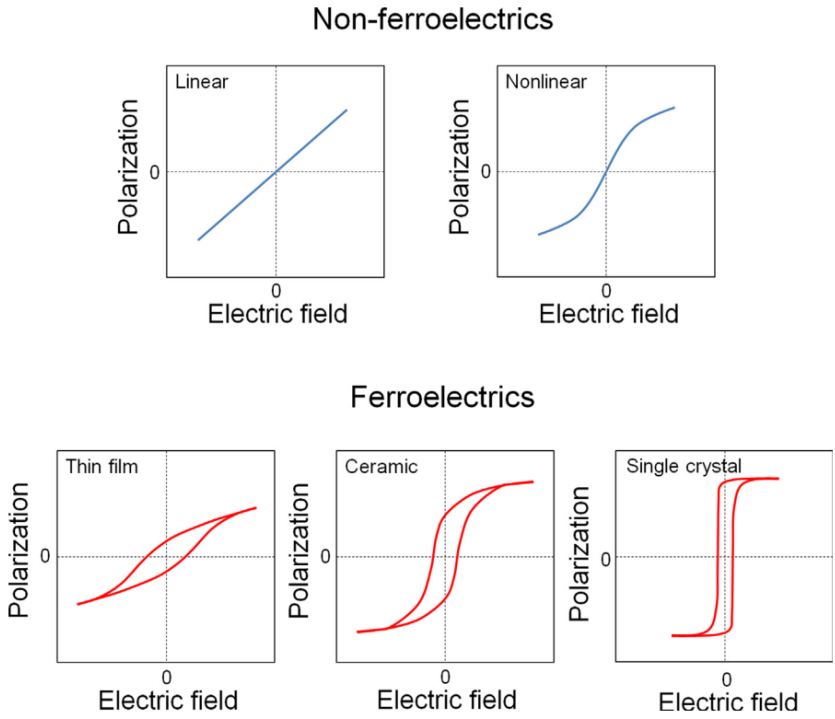

Figure 2.6: A schematic drawing of the characteristic hystersis loop in $P(E)$ of a ferroelectric. Pictures are borrowed from ref. [30].

	Ferroelectric materials	Ferromagnetic materials
Origin of dipole	Charge separation (no intrinsic angular momentum)	Charge flow (intrinsic spin angular momentum)
Dipole interaction	Coulomb (strong)	Ampere (weak relativistic)
Short-range interaction	Elastic coupling	Exchange coupling
Origin of anisotropy	Crystal electric fields	Spin-orbit coupling
Phase transitions	Often first order, non-mean field behaviour rare	Often second order, non-mean field behaviour observed
Dynamics	Generally propagating atomic vibrations	Precessional and dissipative spin fluctuations
Tuning parameter	Electric field (voltage gating)	Magnetic field

Despite seeming similar, electric and magnetic dipole systems in fact exhibit important differences.

Figure 2.7: Comparison of ferroelectric and ferromagnetic systems. Pictures are adapted from ref. [31].

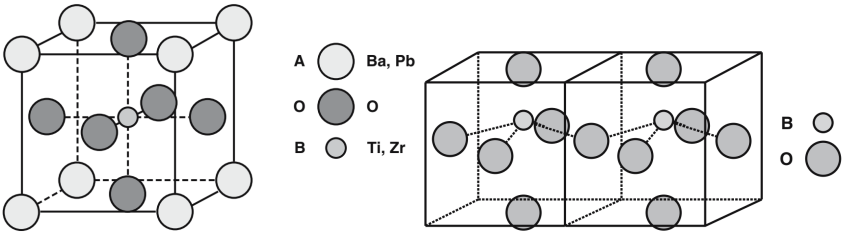

Figure 2.8: Lattice structure of $BaTiO_3$ at (a) paraelectric non-polar state and (b) displacive ferroelectric state. Figures are obtained from ref. [28]

As the geometry of lattice contributes hugely to the nature of ferroelectric, there are two basic types of ferroelectric materials [26], [28]:

1. Order-disorder (amplitude fluctuations driven) - electric dipoles exist above T_C but are randomly oriented, so there is no overall polarization. No addition dipole is induced across T_C. Macroscopic polarization is the result of ordered orientation of the existed dipoles.
2. Displacive (angular fluctuations driven) - no dipole is found within lattice cells above T_C. A relative displacement of sublattices of ions (or atom's nuclei and its electron cloud) is induced across T_C and subsequently generates electric dipoles. The relative displacement is uniform and thus a macroscopic polarization is formed. An schematic illustration taken use of the structure of $BaTiO_3$ is depicted in fig. 2.8.

These two classified mechanisms are not necessarily exhibited exclusively and sometimes coexist in a material and could lead to both presence and absence of ferroelectricity [28]. For example, ionic bonded compounds carry inherent electrical dipoles (displacive), but those dipoles are always anti-aligned due to electrostatics, thus becomes antiferroelectric instead. On the other hand, the Curie-Weiss divergence followed by paraelectrics is the result of both enhancement displacement of the preformed dipoles (displacive) and the flavoured alignment of dipoles due to reduction of thermal fluctuation (order-disorder). The temperature dependence of polarization in $BaTiO_3$ is

an example (fig. 2.9), where the sharp transitions are the results of displacive ferroelectric due to structural changes, the Curie-Weiss divergence in ε' (fig. 2.9(a)) prior to transition is the result of ordering of electrical dipoles (note that spontaneous polarization (fig. 2.9(b)) is constant within each phase).

Neither of the FE transitions is necessarily accompanied by an abrupt transition, *e.g.* structural transition. Displacive FE can be arrived by the freezing-out of active transverse optical (TO) phonon mode, a.k.a. phonon-softening. Order-disorder FE can be reached by the coherence of broad vibration modes [33]. Figure. 2.10 depicts the temperature-dependence of the soft TO mode of $BaTiO_3$, which exhibits both displacive and order-disorder in its FE transition. The reduction of phonon frequency in cubic phase above 410 K is a clear indication of displacive FE transition.

2.5.4 Quantum paraelectricity

At the lowest temperature, where thermal excitation is absent, dipoles shall be stationary and thus succumb to Coulomb interaction to form orders with neighbouring dipoles. Nonetheless, these orders can be prohibited by geometric frustration and quantum fluctuation. In which cases, the electric dipoles persist to tunnel between degenerate energy minima and so a liquid-like ground state is exhibited. A well-known analogue is the quantum spin liquid system in magnetism.

A prime example of quantum paraelectricity encountered by experimentalists is $SrTiO_3$ [34], [36]. There are new material classes showcasing behaviours, such as ferroelectric relaxors [37], organic charge-transfer salts [8], [38]–[41] and M-type hexaferrites [42], [43]. In these systems, a classical paraelectric Curie-Weiss behaviour is well-followed in $\varepsilon'(T)$ at high temperatures, but no transition happens even at T as low as 0.3 K (fig. 2.11(a)) and $\varepsilon'(T)$ seemingly saturates on a plateau at the base temperature.

The quantum paraelectric behaviour is first attempted to be described by the mean-field Barrett theory, which is a quantum mechanical formalism of the ionic polarizability and includes quantum fluctuations due to zero-

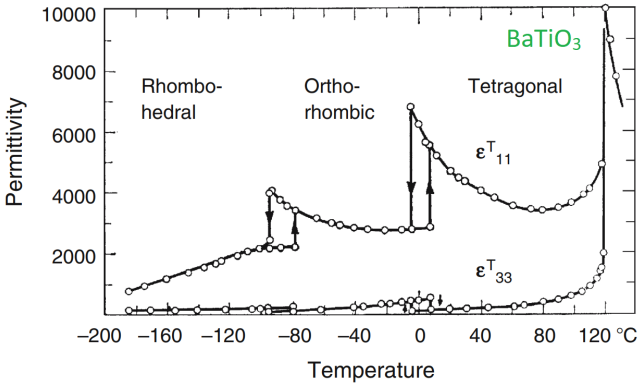

(a)

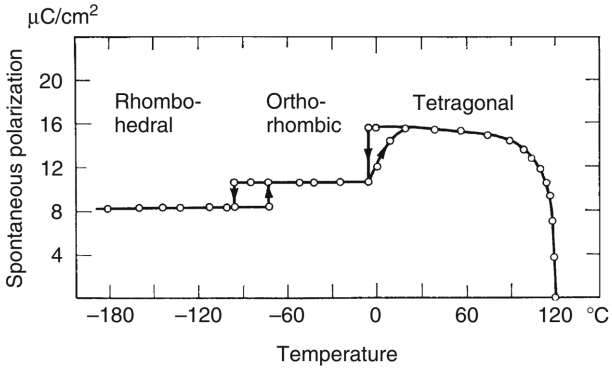

(b)

Figure 2.9: Temperature dependence of (a) the real dielectric permittivity and (b) spontaneous polarization of $BaTiO_3$. Three structural transitions and an order-disorder ferroelectric transition are exhibited in $BaTiO_3$. Figures are obtained from ref. [32]

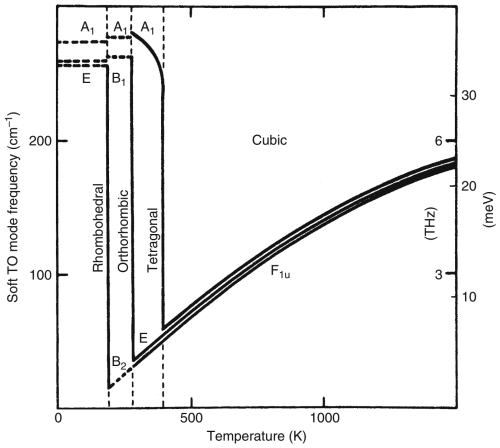

Figure 2.10: Soft-mode behavior in BaTiO3. Figure is obtained from chapter 21 in ref. [28]

point vibration [44]–[46]. The temperature-dependence of ε is plotted in fig. 2.11(b) (labelled as 'QPE') and the equation is:

$$\varepsilon'(T) = \varepsilon_\infty + \frac{C}{\frac{T_1}{2}\coth\frac{T_1}{2T} - T_c} \tag{2.28}$$

Barrett equation is similar to the classic Curie-Weiss law (eqn. 2.27) except for the inclusion of T_1, which is conceptually the dividing point between the classical Curie-Weiss phase and the quantum fluctuation dominated phase when the spectral gap Δ is comparable to the temperature (fig. 2.11(c)). According to Barrett's formalism, the nature of the quantum effect fluctuates the orientation of dipoles and thus prohibits the further enhancement of ε'. If the system undergoes any ordering above T_1, the quantum effect is expected to be simply absent. A quantum critical point (QCP) can be found in between, which is indicated by the full suppression of T_c and emergence of the plateau due to quantum fluctuations.

It is important to note that Barrett's model is a strongly simplified model. It is a single-ion model, namely, all sublattices of atoms except one ion in the

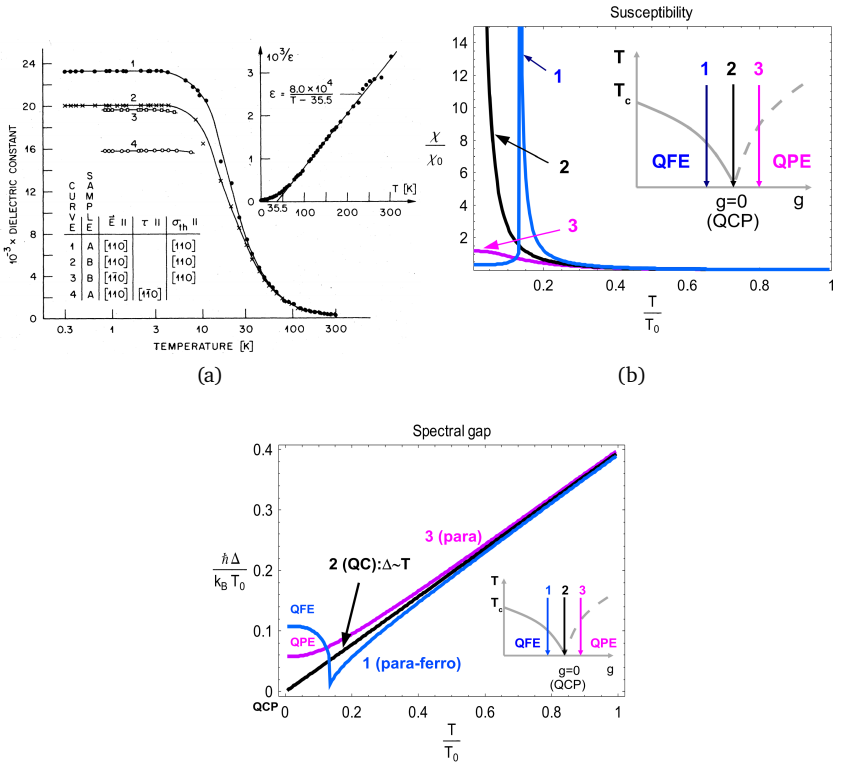

(a) (b)

(c)

Figure 2.11: (a) Temperature-dependence of real permittivity ε' of $SrTiO_3$ reported by ref. [34]. (b) Dielectric susceptibility and (c) spectral gap simulated from the mean-field Barrett model [35].

system are fixed in their equilibrium and do not contribute to the electric order, and the only ion behaves as an independent harmonic oscillator [46]. Only the mode-mode coupling of the soft transverse optical (TO) phonon mode (γ_c) is involved in this derivation [35]. It also assumes dispersion-free phonon excitations $\omega(g) = \tilde{\omega}_0$, where g is the renormalized tuning parameter[26], which is only invalid close to the QCP. Albeit there are conditions for many samples of interests, the sole employment Barrett's equation could provide the essence for understanding [46], *e.g.* TiO_2 [47], $KTaO_3$ [48], [49], $CaTiO_3$ [50], Pb-doped $CaTiO_3$ [51], $BaFe_{12}O_{19}$ [52]. Some of those are depicted in fig. 2.12.

Systems that deviated from Barrett equation were indeed encountered, for instance, $SrTiO_3$ [53]. A modern measurement reveals that at the lowest temperature, the $\varepsilon(T)$ of $SrTiO_3$ is not constant but dropping (fig. 2.13(a)) [31]. This deviation from Barrett's equation is most convinced to be originated from the coupling with long-wavelength acoustic phonons [31], [35], [54]. The theoretical simulation of $\varepsilon(T)$ of $SrTiO_3$ with consideration of acoustic phonons coupling is given in fig. 2.13(b), which agrees very well with the experimental results.

The coupling of polarization to strain, *i.e.* acoustic phonon, enters the free energy in the form of $-\eta\nabla\phi P^2$, in which η represents the coupling strength to the long-wavelength acoustic phonons, $\nabla\phi$ is the strain and P is the polarization [35]. The acoustic phonon acts to soften and reduce the quartic interaction between the optic phonons, hence the negative sign. The negative coefficient propagates into the dependence of permittivity as well, as χ is given by:

$$\chi(T)^{-1} = \Delta^2 = \left(\frac{\gamma_c}{4} - \tilde{\beta}\eta^2\right)T^2 \tag{2.29}$$

with

$$\tilde{\beta} = \frac{1}{3(\tilde{c}^2 - 1)}\left(1 - \frac{1}{\tilde{c}^3}\right)$$

where the first, positive, term is the component due to TO mode-mode

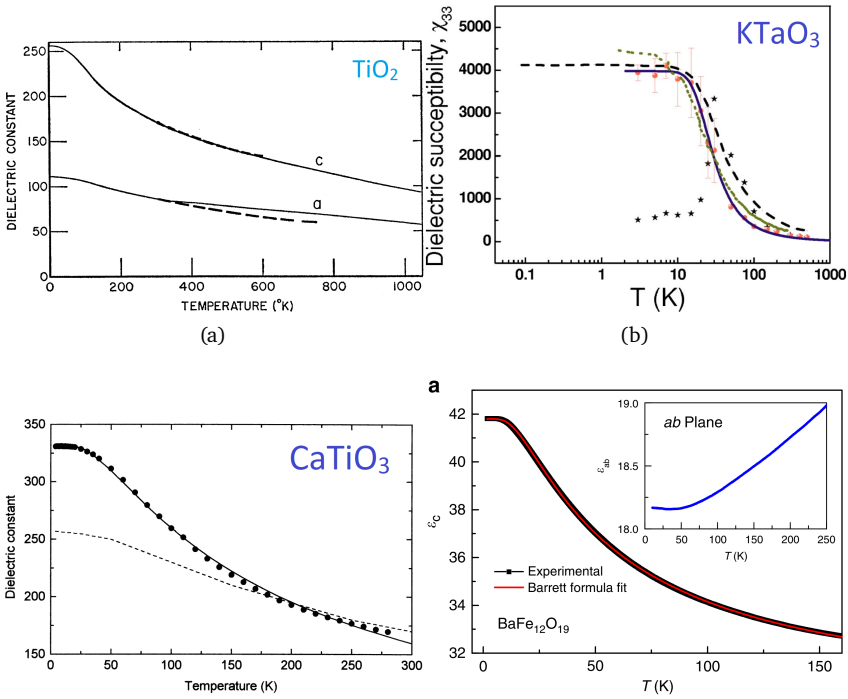

Figure 2.12: Temperature-dependence of the real permittivity ε' of (a) TiO_2 [47], (b) $KTaO_3$ [49], (c) $CaTiO_3$ [50] and (d) $BaFe_{12}O_{19}$ [52].

coupling and the second, negative, term is the component due to the coupling with acoustic phonon and $\tilde{c} = c_a/c_s$ is the ratio of the acoustic to the soft optical phonon velocities. Due to the opposite signs of the two components, a sign flip of the trend of $\chi^{-1} = 0$ can take place at sufficiently high $\eta > \eta_c$. The critical coupling strength η_c is given by:

$$\eta_c = \sqrt{\frac{3}{4}\left(\frac{\tilde{c}^3(\tilde{c}^2-1)}{\tilde{c}^3-1}\right)\gamma_c} \tag{2.30}$$

Figure 2.14(a) depicts the lines of $\chi^{-1} = 0$ with different η. At low η, $\chi^{-1} = 0$

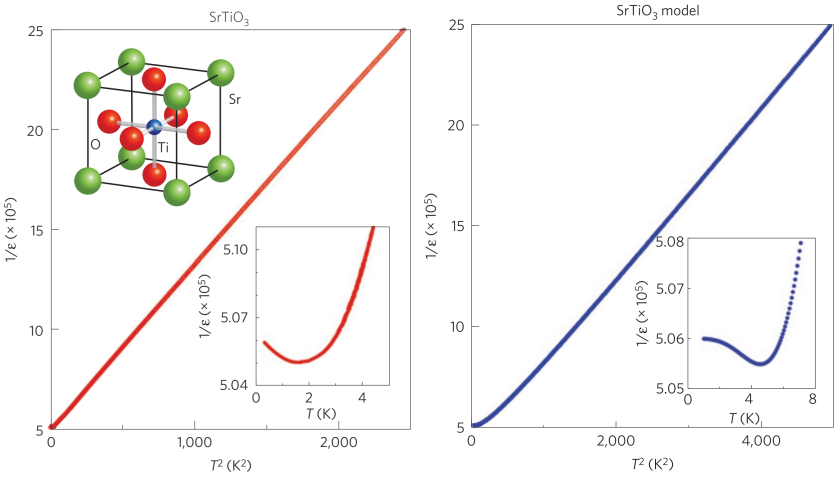

(a) (b)

Figure 2.13: (a) Experimental and (b) theoretical simulation of the inverse permittivity $1/\varepsilon'$ of $SrTiO_3$ from a more modern report in 2013 [31]. Instead of a saturated plateau, the permittivity exhibits a drop at the lowest temperature, which is not captured by the mean-field Barrett model.

only exists in $g < 0$, the classical phase, and it corresponds to the classical FE transition. The effect of η is the enhancement of T_C as the acoustic phonon assists in softening of the TO mode. At high $\eta \geq \eta_c$, the $\chi^{-1} = 0$ line meanders into the quantum phase ($g > 0$) but remains to end at $g = 0$ at $T = 0$, meaning that the system would temporally enter the FE state at finite temperatures, due to the strong softening by acoustic phonons, but the ground state is still dominated by the zero-point fluctuation because the acoustic phonon dies out in the absence of thermal excitations. Such that, for systems adjacent to the QCP in the quantum phase, the temperature dependence of χ^{-1} would follow a $-T^4$ relation below a local minimum and still saturate to a finite magnitude at the lowest temperature, as illustrated in fig. 2.14(b).

Apart from the saturating plateau at $T = 0$, the QPE nature can also

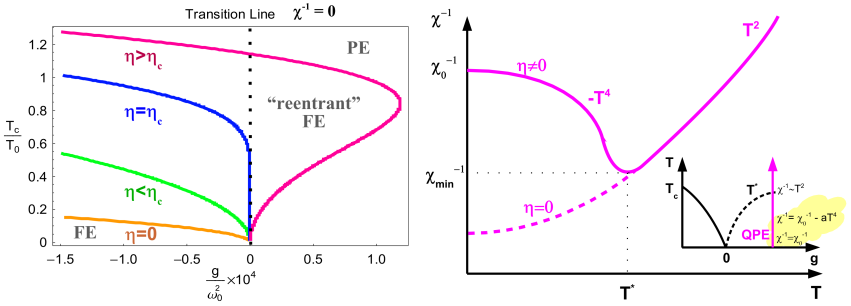

(a) (b)

Figure 2.14: Simulations of quantum ferroelectric transition included coupling with acoustic phonons [35]. (a) Transition line $T_c(g)$ for different acoustic coupling constant η. At sufficiently large η, a "reentrant" of the ferroelectric phase can be induced. (b) Schematic temperature dependence of the static dielectric susceptibility χ with and without long-wavelength acoustic phonon coupling.

be identified by the temperature dependence at finite temperatures. For systems inside the quantum phase and at low temperature, the susceptibility χ^{-1} follows [35], [55]:

$$\chi^{-1}(T) = a + \frac{5\varepsilon_0 k_B^2 b}{18\hbar c v} T^2 \propto T^2 \tag{2.31}$$

where a, b and c are parameters of the Ginzburg–Landau free-energy expansion in the polarization P at zero temperature, *i.e.* $f = (a/2)P^2 + (b/4)P^4 + (c/2)(\Delta P)^2$. An example is the doping series $(CH_3NHCH_2COOH)_3CaCl_{2(1-x)}Br_{2x}$ (TSCC) [55]. The susceptibility χ^{-1} of TSCC with three dopings ($x = 0.1, 0.9$ and 1) are plotted in fig. 2.15. The undoped and the lightly doped ($x = 0.1$) TSCC are ferroelectric materials and they follow Curie-Weiss equation (eqn. 2.27), as shown in fig. 2.15(a). Upon doping, the FE is suppressed as T_C shifted down and a saturation plateau is developed, accompanied by the exhibition of $\chi^{-1} \propto T^2$ (figs. 2.15(b,c)). At $x = 0.9$, a shallow minimum occurs in χ^{-1}, which fits well with the expected behaviour as the system is

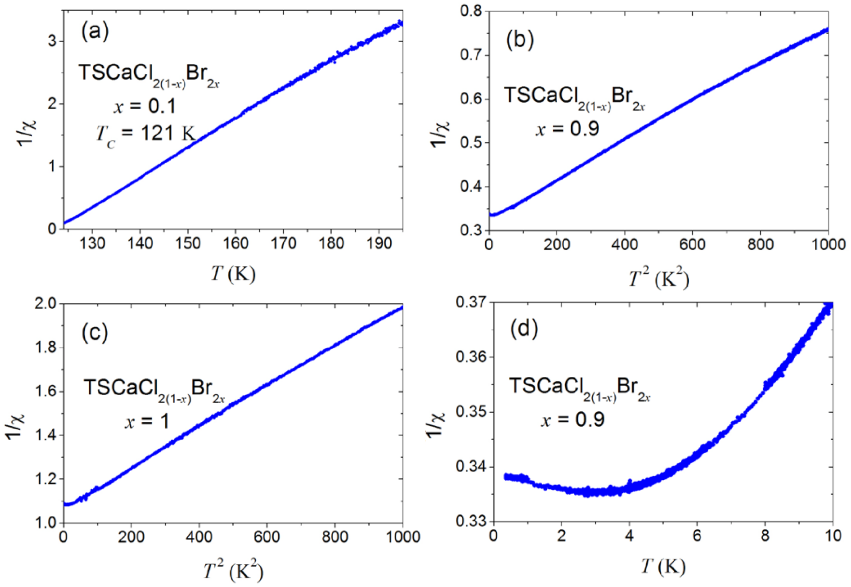

Figure 2.15: Temperature-dependence of inverse dielectric susceptibility $1/\chi$ in $(CH_3NHCH_2COOH)_3CaCl_{2(1-x)}Br_{2x}$ with $x =$ (a) 0.1, (b) 0.9 and (c) 1 reported in ref. ,[55]. (d) The base temperature plateau exhibit in $x = 0.9$.

transiting across the QCP.

Complete ferroelectric phase transition can be led by engineering the systems. On $SrTiO_3$, application of strain [56] and chemical substitution with Ca [57] or heavier oxygen isotope [58], both successfully brought the system into FE. The phase transition is justified by the variation of the critical exponent (fig. 2.16(b)). The oxygen-18 doping increases the masses, slows the lattice vibration and thus draws the soft mode to reach zero frequency at finite temperature. On the opposite, the application of pressure on $SrTiO_3$ [59] and Ba-doped $SrTiO_3$ [60] appears to be pushing the system further into the QPE phase, behaving more similar to the chemically akin $KTaO_3$ (fig. 2.16(d)) [61]. A comparative study of $SrTiO_3^{16}$ and $SrTiO_3^{18}$ under pressure explicitly demonstrated that $SrTiO_3^{18}$ under pressure behaves just

as $SrTiO_3^{16}$ [59]. Explanation for the counter effect of pressure is attempted by nonlinear core-shell coupling model [59], which suggests the anisotropic charge density at the oxygen is crucial for FE transition and the anisotropy is weakened due to the homogeneous pressure application.

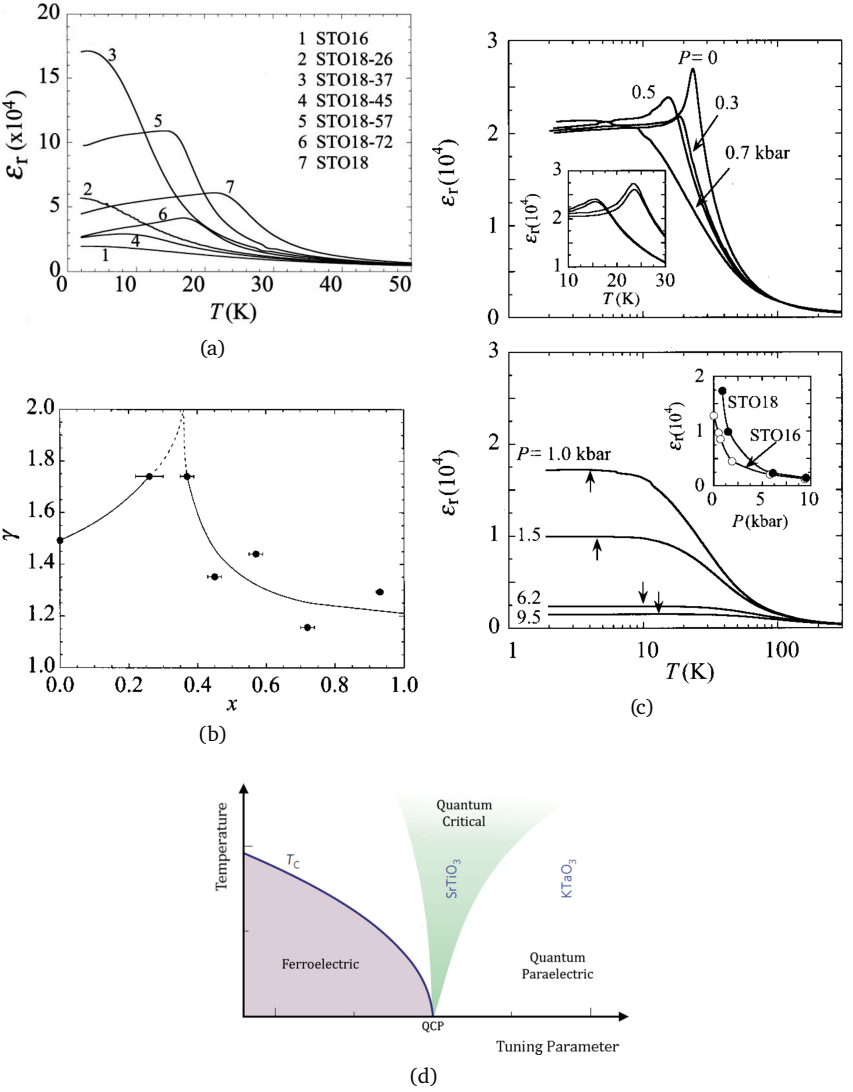

Figure 2.16: (a) Temperature dependences of dielectric permittivity for $SrTi(^{16}O^{18}_{1-x}O_x)_3$ [58]. (b) Critical exponent for $SrTi(^{16}O^{18}_{1-x}O_x)_3$ [58]. (c) Temperature-dependence of the dielectric permittivity for $SrTi^{18}O_3$ under low-pressure $P < 0.7$ kbar [59]. (d) Predicted phase diagram for $SrTiO_3$ and related compounds [31] obtained from ref. [61]. The "tuning parameter" can be realized through physical pressure application.

2.6 Conduction in solids

In solids, the itinerant electron is not the only mean for electric conduction. There are several other methods and carriers, which lead to separated dielectric consequences.

2.6.1 Hopping

Charge carriers experience the lowest potential at the ions with an opposite net charge. Adjacent ion sites are separated by potential barriers. When the kinetic energy of the charge carriers is more than the barriers, the charge carriers are delocalized, *i.e.* become mobile, and travel from ions and ions smoothly; when the kinetic energy of the charge carriers is less than the barriers, charge carriers can still tunnel through the barriers and perform conduction although it is, energetically speaking, localized. Later is named 'hopping' conventionally for the sake of visualization (fig. 2.17).

The probability of the charge carriers hopping from site A to site B, *i.e.*

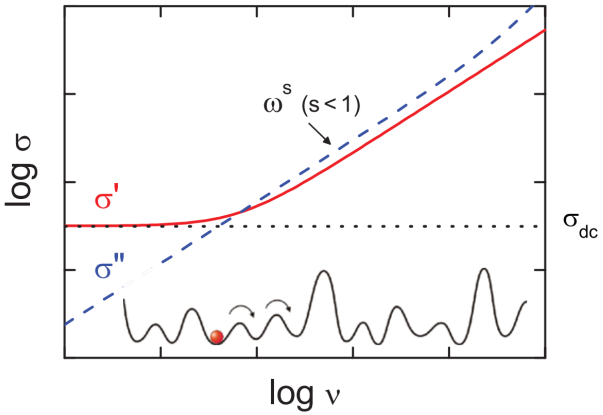

Figure 2.17: Schematic representation of the σ' (solid line) and σ" (dashed line) for hopping charge transport taken from ref. [23]. The inset is a schematic drawing of the hopping of the localized charge carrier in a disordered energy landscape.

P_{AB}, depends on more than the barriers and the energy difference between two states, but also the physical distance between two sites as the further away, the lower the hopping probability. In heterostructure, it is possible to be more favourable for hopping to further sites instead of hopping to the adjacent sites. In this case, variable-range-hopping occurred instead of the nearest-neighbour-hopping.

In the end, the difference in the hopping mechanism affects the temperature dependence of the conductivity:

$$\ln \sigma = -\left(\frac{T_0}{T}\right)^{\frac{1}{\gamma}} + \ln \sigma_0 \tag{2.32}$$

2.6.2 Ion migration

Under the application of external $\vec{E}$, charge-carrying ions (or even molecules) can sometimes, instead of being polarized about an equilibrium position, exhibit migration and propagate through the solids. Naturally, ions are not allowed to move freely within the lattice, so the migration is generally mediated by vacancies or defects due to structural imperfection or impurities. Figures. 2.18(a-b) illustrate the types of defects and the condition forming the defects for ion migration. The Schottky defects are on-site lattice stoichiometric vacancies formed because of the absence of composition element/ion. The Schottky defects can be interpreted as the intrinsic defect as the defects are induced after the fabrication of crystals and invariant to the measurement conditions. The Frenkel defects are interstitial spaces accommodating the propagating ions (and, subsequently, the original site for the propagating ion becomes a Schottky defect). The Frenkel defect can, in contrast, be interpreted as the extrinsic defect as the defects are induced by excitations, *e.g.* thermal excitation.

Besides the intrinsic interstitial spaces within the ideal lattice, additional interstitial sites can be formed by structural modulations and on the grain boundaries. Figures. 2.18(c-g) depict several common pathways to additional interstitial channels for ion migration.

The feasibility of ion migration can be quantified by accounting for the

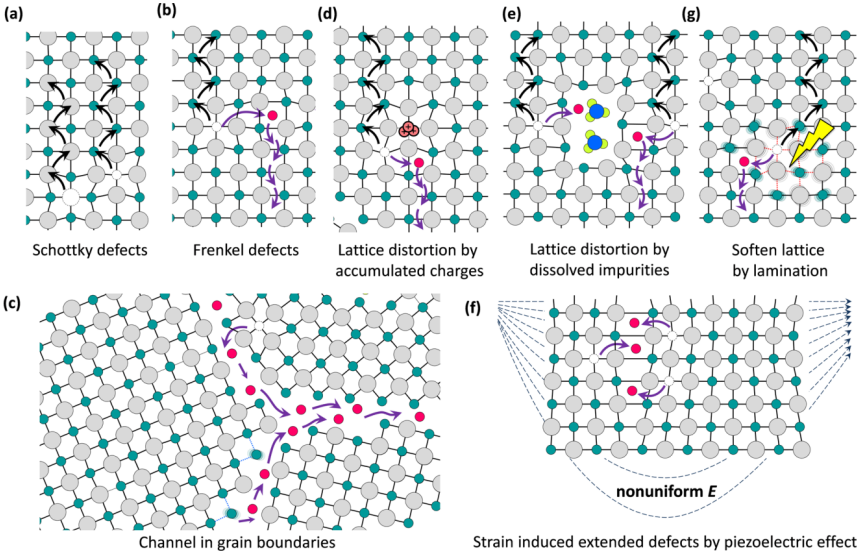

Figure 2.18: Schematic illustrations of (a) the Schottky defects, (b) the Frenkel defects and (c-g) system conditions which induces the defects. This figure is reproduced from Ref. [62].

activation energies of the two defects [63]. The activation energy for Schottky defect E_D represents the energy to create a mobile ion, whereas the activation energy for the Frenkel defect E_A represents the energy needed to create additional sites, apart from the intrinsic defects, for migrating ions to pass by. The conductivity due to ion migration σ_i is given by:

$$\sigma_i \propto r_m N_i \tag{2.33}$$

where $r_m \propto \exp\left(-\frac{E_A}{k_B T}\right)$ is the migration rate and $N_i \propto \exp\left(-\frac{E_D}{2k_B T}\right)$ is the

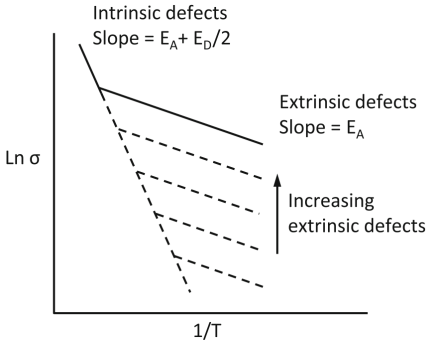

Figure 2.19: A schematic illustration of the ionic conductivity obtained from ref. [63].

number density of the migration sites, so the equation becomes:

$$\sigma_i \propto \exp\left(-\frac{E_A}{k_B T}\right)\exp\left(-\frac{E_D}{2k_B T}\right) \tag{2.34}$$

$$\sigma_i = A\exp\left(-\frac{E_A + E_D/2}{k_B T}\right) + C \tag{2.35}$$

Experimentally, E_A and E_D can be determined by measuring the temperature-dependence of the ionic conductivity down to a very low temperature. According to eqn. 2.35, the ionic conductivity will demonstrate a linear $\ln\sigma$-$1/T$ curve. Moreover, E_D is involved in the ion migration process only at sufficiently high temperature, when the thermal energy is enough to excite the locally stable ions and create the Frenkel defects. Below that temperature threshold, only the extrinsic Schottky defects exist and thus, only E_A is involved in the ionic conductivity. Therefore, the linearity in a $\ln\sigma$-$1/T$ plot shall exhibit a slope change across the temperature threshold. Figure. 2.19 is a schematic illustration for the ionic conductivity [63].

Chapter 3

Background

Hybrid organic-inorganic halide perovskite and water-confining beryl share the similar characteristic of strong polar ions preserve a high degree of freedom within the rigid framework. The granted freedom enables rich and high-amplitude dynamics of polar ions, so they are vastly responsive to external voltage or inter-dipole coupling and are subjected to delocalization with a low excitation threshold. Their spacious structure is also favourable for ionic transport and formations of charge order domains. These properties makes the hybrid system a fertile playground for occurrences of substantial ionic conduction and long-range charge orders.

3.1 Hybrid halide perovskite

Perovskite is an abundant structural class of chemical compounds with the chemical formula ABX_3. The freedom of composition is high; there have been single elements (*e.g.* Ca, Sr), inorganic and organic ions (*e.g.* Cs^+, K^+, $CH_3NH_3^+$) found on site *A*, halide anions (*e.g.* I^-, Br^-, Cl^-) and chalcogenide anions (*e.g.* O^-, S^-, F^-) found on site *X*. Perovskite families exhibit rich physical properties by varying the compositions, including those

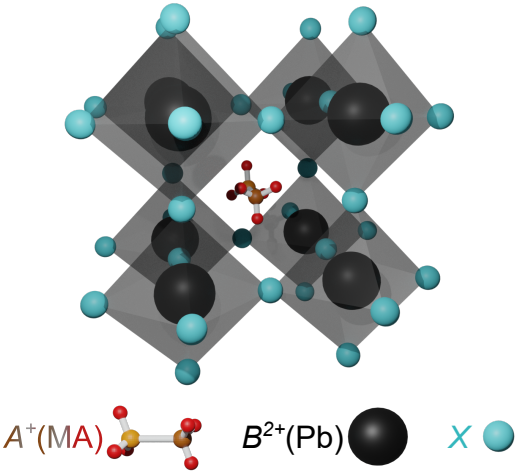

Figure 3.1: High-temperature cubic structure of ABX_3 (In this thesis, $A = CH_3NH_3^+$, B = Pb and X = I, Br or Cl). The organic subunits inside the inorganic cage have freedom of motions.

most fascinating ones, for example, colossal magnetoresistance [64], [65], ferroelectricity [66] and superconductivity [67].

An example of the perovskite structure is depicted in fig. 3.1. The B^{2+} and X^- ions would form an orthorhombic cage-like unit cell as the A^+ ion sits inside. Besides orthorhombic, tetragonal, cubic, and rhombohedral cages are also found but less common. Structural phase transitions between the aforementioned phases are frequently found in perovskite compounds. Nonetheless, the picture of A^+ ion contained by a cage made of B^{2+} and X^- ions is robust among the perovskite structured family.

In the scope of this thesis, the three halide analogues of $CH_3NH_3PbX_3$ (X = I, Br and Cl) are selected for a comparative study.

3.1.1 Motivations

Among the numerous members of perovskites, hybrid organic-inorganic halide perovskites (HOIP) particularly stood out in the recent decades be-

X	$T_{\text{cubic}\rightarrow\text{tetragonal}}$	$T_{\text{tetragonal I}\rightarrow\text{tetragonal II}}$	$T_{\text{tetragonal}\rightarrow\text{orthorhombic}}$
I	330 K	/	162 K
Br	236 K	155 K	148 K
Cl	178 K	/	172 K

Table 3.1: Structural transition temperatures of $CH_3NH_3PbX_3$ reported by ref.[72], [73].

cause of its outstanding photovoltaic properties. In 2009, methylammonium lead iodide $CH_3NH_3PbI_3$ (MAPI) has been deployed as visible-light sensitizers on fabricating photoelectrochemical cells in attempt to discover an organic (*s.t.* cheap) material with balanced light absorption and photovoltaic generation [68]. The energy harvesting efficiency of a MAPI solar cell is surprisingly good and even surpasses the established light harvester agent at the time [69], [70]. MAPI was, therefore, immediately promoted to be one of the most promising next-generation solar energy harvesting materials and so, subsequently, immerse researches are incentivized, including the pursuit of the fundamental physical nature. Besides MAPI, researches on other hybrid organic-inorganic halide perovskites (*e.g.* halide analogue with $X =$ Br or Cl, other organic cation formamidinium $HC(NH_2)_2^+$) are collaterally triggered [71].

3.1.2 Crystal structure of $CH_3NH_3PbX_3$ ($X =$ I, Br or Cl)

All three of the $CH_3NH_3PbX_3$ (MAPX) are in the cubic structure phase at high temperatures (fig. 3.1). Heat capacity and dielectric measurements (fig. 3.2) found that they all undergo structure transitions when being cooled: from cubic phase to tetragonal phase and from tetragonal phase to orthorhombic phase [72], [73]. All of the transitions are of the first order, so hysteresis will be found between cooling and warming. The transition temperatures of each halide compound during cooling are listed in table 3.1.

From the calorimetry and infrared vibrational spectroscopy analysis [72], these phase transitions are of the disorder-order type, referring to the ordering of MA^+ ion with respect to the C-N axis. This suggestion is supported by

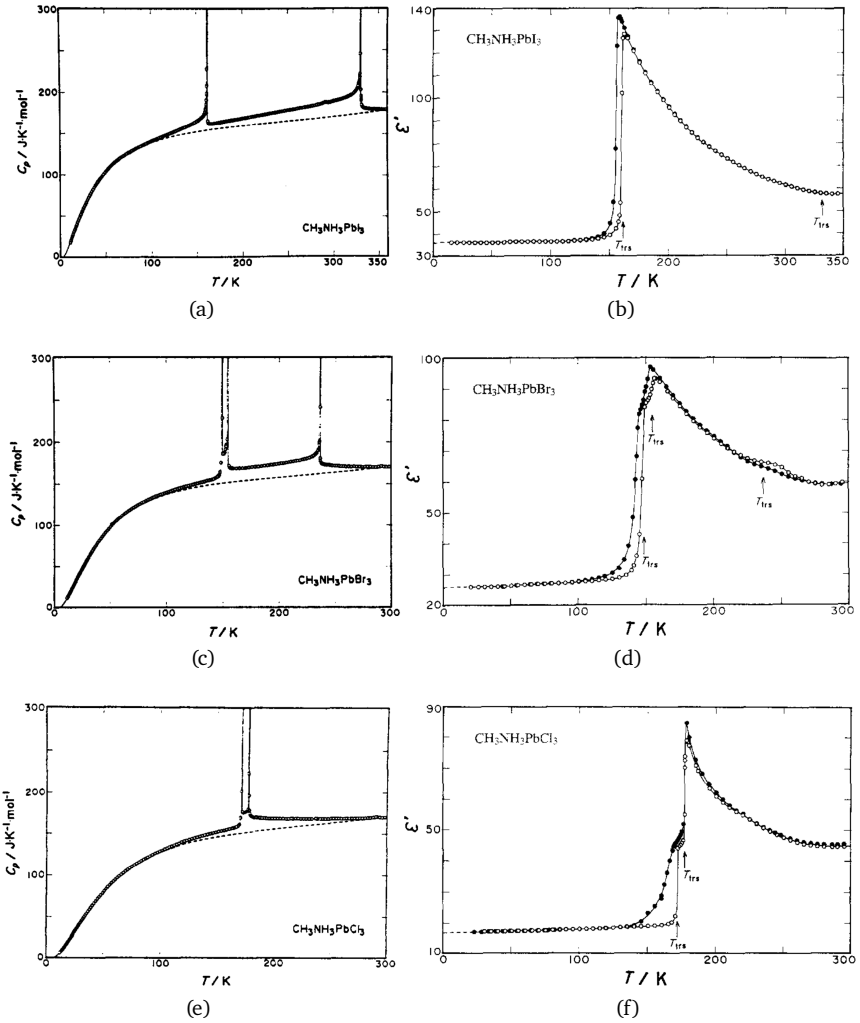

Figure 3.2: Molar heat capacity (left) and real dielectric permittivity (right) of MAPX with (a),(b) $X = \mathrm{I}$, (c),(d) $X = \mathrm{Br}$ and (e),(f) $X = \mathrm{Cl}$ reported by ref. [72], [73].

nuclear magnetic resonance (NMR) and nuclear powder diffraction (NPD) measurements on $CH_3NH_3PbI_3$, as they indicated MA^+ ion is disordered in the inorganic cage in cubic and tetragonal phases and is ordered in the orthorhombic phase [74]–[76].

It is pretty consistent with the experimental evidence that the high-temperature cubic and tetragonal phases are disordered, but the details of ordering in the low-temperature orthorhombic phase is still under debates and uncertain. Other dielectric measurements with much improved base temperature were motivated to examine the motions of MA^+ cations in the orthorhombic phase [77], in which frequency-dependent dielectric loss peaks were observed around $T = 60$ K (fig. 3.3), suggesting a glassy structure. The NPD and elastic neutron scattering (ENS) experiments also did not rule out but suggested a substantial dynamic disorder down to at least 70 K [76], [78]. It has been commented that these disorders might originate from some subtler and more complex molecular motions than the rotation around C-N axis of MA^+ molecules, for example, coupling between MA^+ cations and the Pb-X framework [77]. More background regarding the MA^+ cation's molecular motions is documented in sec. 3.1.4.

Apart from reduction in temperature, the structural transformations could also be brought out by the application of physical pressure. Early pressure studies were done merely up to 0.6 GPa, but the structural triple point is already captured [79]–[81]. The $T - p$ phase diagrams of MAPX are given in fig. 3.4. The phase diagrams are quite deviated between different halides. For $X = \mathrm{I}$, a pressure-induced phase appears between tetragonal and orthorhombic phases beyond 0.1 GPa. The territories of the new phase expand rapidly and completely supplant the tetragonal phase at 0.35 GPa. The low-temperature orthorhombic phase is also being suppressed by the new phase slowly; for $X = \mathrm{Br}$, the tetragonal phase with space group P4/mmm perishes soon after 0.1 GPa; for $X = \mathrm{Cl}$, the tetragonal phase (also with space group P4/mmm) perishes after 0.1 GPa and only the cubic to orthorhombic transition remains with rising transition temperature.

Conspicuous changes are exhibited in the dielectric permittivity across the structural transformations. Figure. 3.5 depicts the dielectric permittivity

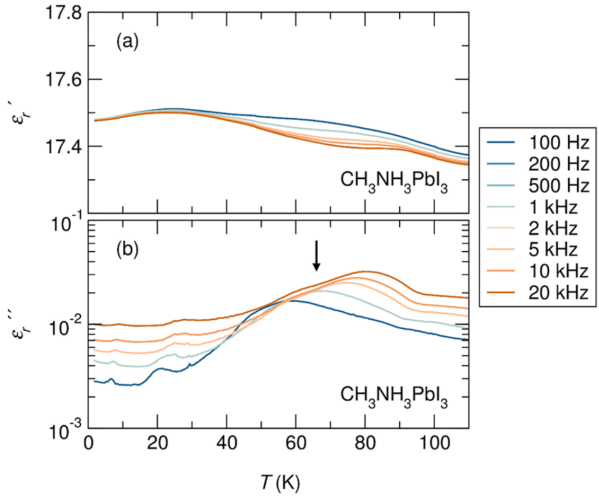

Figure 3.3: Low-temperature (a) real and (b) imaginary parts of the relative permittivity of MAPI reported by ref. [77].

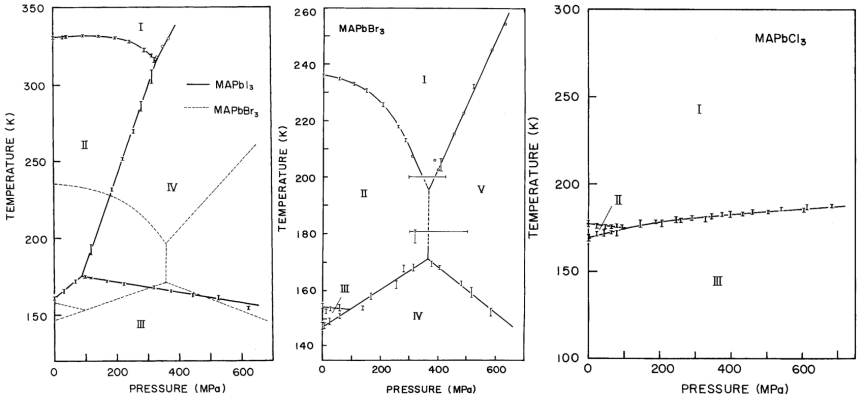

(a)

Figure 3.4: $T-P$ phase diagram of MAPX (start from the left, $X =$ I, Br and Cl) reported by ref.[80], which is in total agreement with an eariler study ref.[79].

under pressure (up to 0.6 GPa) data reported by ref. [80]. Subtle but noticeable polarization anisotropy of the transition is found in $X = \mathrm{I}$ and Br, which was missed by the earlier dielectric report [73]. No measurement on [110] is done on $X = \mathrm{Cl}$ sample by this report, so the anisotropy in chloride sample is unknown but likely to also exist. The shapes of the transitions of $X = \mathrm{I}$ and Br are consistent, whereas the transition in $X = \mathrm{Cl}$ during warming behaves differently between the two reports. In the later report [80], the warming transition has the same shape as cooling's with a hysteresis; whereas in the earlier report [73] (fig. 3.2(f)), the separation of the warming transitions is significantly narrower than the cooling cycle and so the cubic-to-tetragonal transition even takes place at a lower temperature than cooling.

Apart from dielectric measurements, neutron diffraction (ND), X-ray diffraction (XRD), resistivity measurements have also been performed and up to higher pressure to probe the evolution of structure-property relations of the MAPX series.

In the case of MAPB, ND measurements found that MAPB has a phase transformation from cubic $Pm\bar{3}m$ to distorted cubic $Im\bar{3}$ (with Pb-X-Pb angles) at 1 GPa and amorphizes at around 3 GPa (fig. 3.6) as the organic cations lose long-range orientational ordering and therefore suggest the energy gain for orientational ordering is low and the phase transitions are mainly driven by the volume reduction [81], [82]. XRD measurements were done up to 34 GPa. Deviated from the ND report, the XRD measurements observed the cubic $Im\bar{3}$ phase only existed between 0.4 and 1.8 GPa and an orthorhombic $Pnma$ structure was found afterwards. In addition, the structure will be amorphized at 4 GPa, which is attributed to the tilting of $PbBr_6$ octahedra and the loss of the long-range ordering of MA cations. This amorphization is also found to be reversible, as the structure recovered upon pressure release, which suggests a memory effect in the MAPB compound. Amorphization raises the resistivity by 5 orders of magnitude.

In the case of MAPI, ND measurements reported a $Fmmm$ to $Im\bar{3}$ transition at 0.3 GPa and also an amorphization at around 3 GPa [82]. The amorphous phase maintained up to 48 GPa. Although the degree of amorphization is severe, signalled by the broadening of diffraction, some Bragg reflections

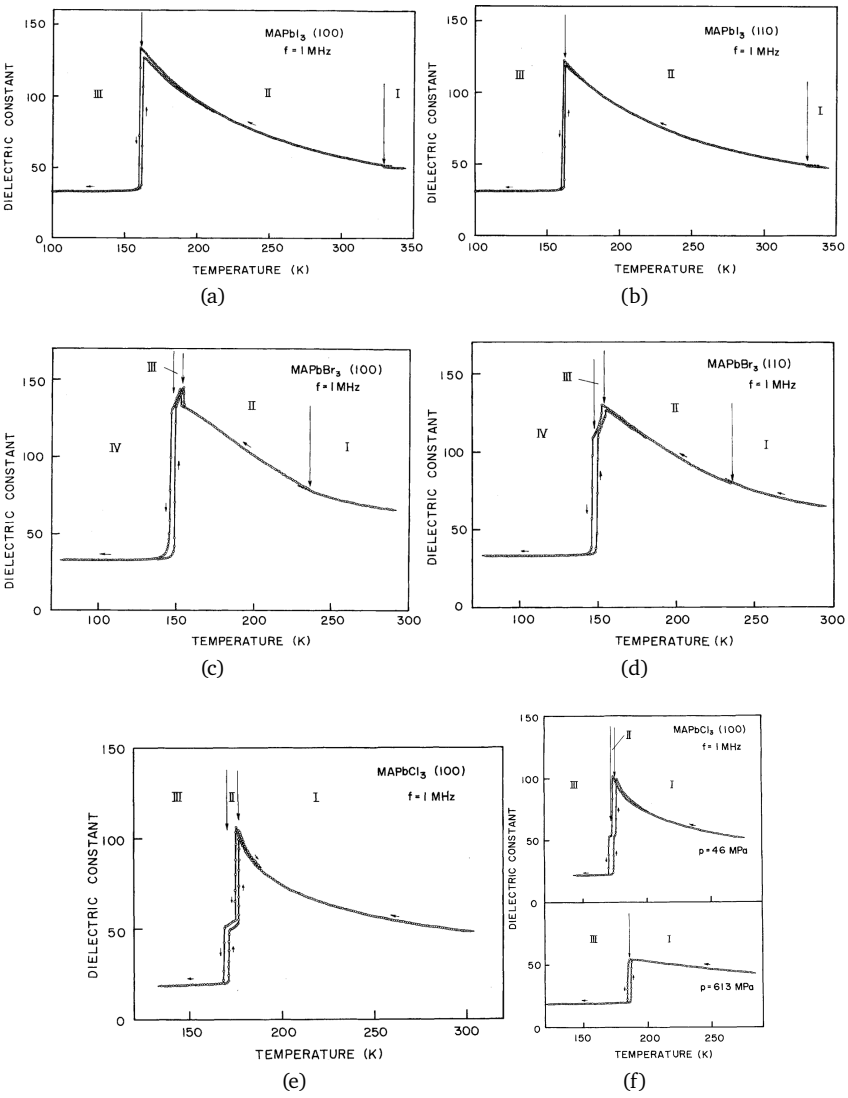

Figure 3.5: Temperature-dependence of the real dielectric permittivity of MAPX with (a-b) $X = \mathrm{I}$ along [100] and [110] direction, (c-d) $X = \mathrm{Br}$ along [100] and [110] direction, and (e-f) $X = \mathrm{Cl}$ along [100] direction under ambient, 46 MPa and 613 MPa reported by ref.[80].

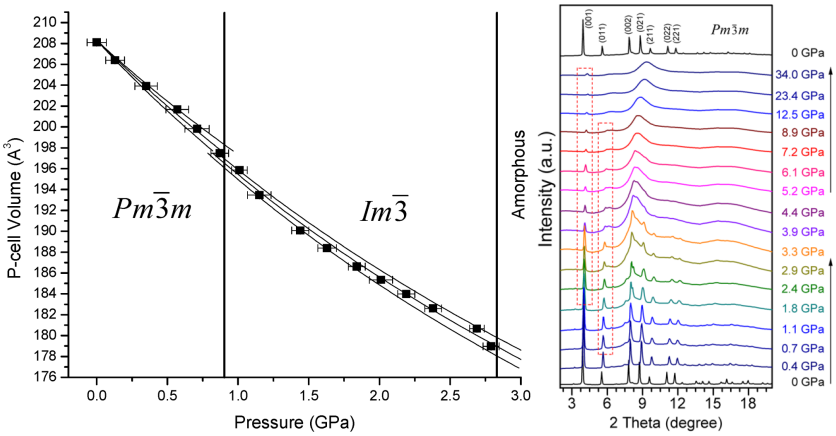

Figure 3.6: (a) Pressure-dependence of the volume of MAPB reported by ref. [81]. (b) XRD patterns under pressure. [85].

remain discernible, meaning a certain degree of crystallographic long-range order persists through the amorphous phase.

In the case of MAPC, XRD measurements recorded a isostructural transition of cubic $Pm\bar{3}m$ at 0.8 GPa followed by a orthorhombic transition at 2.0 GPa [83]. There exists only one other report to the author's best knowledge. In the other report [84], slow transition kinetics and coexistence of phases are evidenced by time dependent of PXRD patterns. Such that, no uniform structure is established in MAPC under pressure.

3.1.3 Ion migration in $CH_3NH_3PbX_3$ (X = I, Br or Cl)

The electrical conduction in $CH_3NH_3PbX_3$ has also been extensively measured since the resistivity and polarization in solids also decide the photoharvesting performance. A significant ionic migration is identified in $CH_3NH_3PbX_3$ which also leads to a gigantic DC dielectric permittivity.

The existence of influential ionic migration was first speculated by the

hysteresis observed in photocurrent measurements on $CH_3NH_3PbI_3$ solar cells. As depicted in fig. 3.7(a), after the light pulse excitation, there is a slow rise following the immediate steep gain in the photocurrent, a signature of ionic charge transport [86]–[88]. The same delayed, slow growth is also observed in DC polarization measurement (fig. 3.7(d)). The origin of this slow response could be mechanisms other than ionic migration [89]–[91], for example, ferroelectricity [91] or the charge-trapping effect [92]. However, experimental results like neutron scattering [93] and piezoresponse force microscopy measurements [94] both indicate that ferroelectricity is unlikely to present in $CH_3NH_3PbI_3$. Nonetheless, concurrently, a divergence in dielectric permittivity exhibits in DC (fig. 3.7(c)), which is entirely consistent with the ions migration picture [77], [88], [95], [96], as mobile charge-carrying ions travel to and accumulate on the electrical surfaces. This DC polarization also decays as temperature drops, which disproofs the idea of ferroelectric or dipolar ordering. However, other mechanisms which could lead to the same divergence of ε' at DC, for instance, grain boundary- and electrode-polarization or electron accumulation [18], are not excluded.

Iodide ion I^- is determined to be the major transporting ions by experiments and computations. Quantum mechanical calculation reveals the prevalence of ionic over electronic disorder in $CH_3NH_3PbI_3$ and equilibrium concentration of I^-, Pb^{2+} and $CH_3NH_3^+$ vacancies, suggesting a Schottky-type vacancy-mediated ionic diffusion [97]. A subsequent first principle calculation estimated the activation energies and diffusion coefficients for all ions and found a high energy barrier for migration of Pb^{2+} and a relatively significantly lower diffusion coefficient for $CH_3NH_3^+$. X-ray diffraction and energy-dispersive X-ray spectroscopy on artificial chemical potential gradients structure with $CH_3NH_3PbI_3$ (fig. 3.7(b)) identified only I^- ion is mobile [95]. Given the existence of substantial diffusing I^- ions, the gigantic polarization at low frequency is henceforth believed to be the stoichiometric polarization due to I^- ions accumulation [95].

Nonetheless, other ions' migration like MA^+, Pb^2+ and H^+ is not ruled out. From first-principles calculations, MA, Pb and H are all eligible for migration with an activation barrier of 0.5, 0.8 and 0.5 eV, respectively, whereas I^-

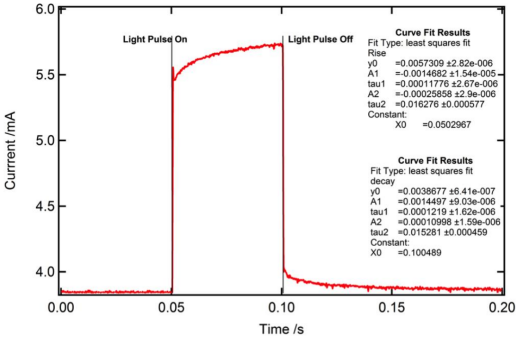

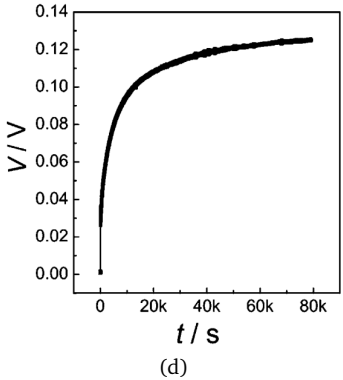

Figure 3.7: (a) Transient current dynamics of perovskite devices. Slow reaction times of current after light pulse indicates ionic diffusion processes. [86]. (b) Flow directions of the charged ion species in a Pb|$MAPbI_3$|AgI|Ag cell under electrical bias [95]. (c) Frequency-dependence of real permittivity ε' of $MAPbI_3$ [95]. The gigantic divergence at low frequency is the signature of stoichiometric polarization due to ion migration. (d) DC polarization curve for a C|$MAPbI_3$|C solar cell [95]. The delayed build-up voltage is a sign of mixed, ionic and electronic, conduction.

has a much smaller barrier 0.1 eV [98]–[100]. The slow photoconductivity response in MAPI is of the order of 1 ms to 1 s [87], so it is likely to be a high-amplitude vibration mode, *e.g.* MA^+ ion translational hopping. Given the similar activation barrier, H^+ may similarly perform the migration in the MAPX crystal. A H^+ vacancy is found to be the major detrimental non-radiative recombination centre, *i.e.* the major bottleneck for high photovoltaic performance, by first-principles calculations [101]. Therefore, ionic diffusion might be a crucial limiting factor for light-harvesting ability as well.

Ion migration also has a negative impact on stability. The degradation in MAPX is in the form of breaking down of PbI_3^- network and formation of PbI_2. Frequent migration of MA^+ and I^- ions both thus promote the break-down progress and reduce the structure stability [102].

3.1.4 $CH_3NH_3^+$ cation motion in $CH_3NH_3PbX_3$ (X = I, Br or Cl)

The $CH_3NH_3^+$ (MA^+) cation and its dipole moment are not restricted tightly in a definite position and direction inside the inorganic PbX_3^- octahedra framework and, instead, multiple degrees of freedom are granted. Under different conditions, MA^+ has been suggested to perform a rotation around C-N dipole axis [93], [103], [104], a "wobbling-in-a-cone" small degree in-plane rotational vibration [105], a jump-like tunneling reorientation [93], [104]–[108], a free isotropic reorientation in high-temperature cubic phase [75] of the dipole with respect to the PbX_6 lattice cages, and a translational tunneling between adjacent cages [103], [109], [110].

All of the aforementioned motions are exhibited in the high-temperature cubic phase. The geometric symmetry requires orientation disorder from the MA^+ dipoles [108]. NMR measurements and crystallographic analysis additionally report that the exact position of MA^+ is undeterminable in high-temperature cubic phase [109], [110]; thus a translational tunnelling between adjacent cages is suggested. Free isotropic reorientation has once been suggested in the early report [75]. Although not conclusively disproved, the validity of free orientation has been abandoned given the

[1] Inferred by ref. [93]

Motion	Method	Year	Time	Frequency	Ref.
Vibration modes of MA^+ cation	FTIR	2015	< 30 fs	> 30 THz	[111]
Small amplitude reorientation	2D IR	2015	~300 fs	3.33 THz	[105]
In-cage reorientation	NMR	1985	~200-400 fs	2.5-5 THz	[74]
	mm-wave interfero -meter	1987	5.37 ps	186 GHz	[112]
	NMR & NQR	1991	0.1 ps	10 THz	[75]
	MD	2013	3.14 ps	318 GHz	[113][1]
	ab initio & IR	2014	4-6 ps	167-250 GHz	[107]
	QENS	2015	14 ps	70 GHz	[93]
	2D IR	2015	3 ps	333 GHz	[105]
(Unidentified)	Dielectric	2017	1 ns	1 GHz	[108]

Table 3.2: Motions observed experimentally within the MAPX single crystals.

sizeable hydrogen bonding between the amine-group and halides anions of the inorganic network [114]. Instead, from the calculation and experimental observations, the MA^+ dipole is evidenced to perform 12-fold tunnelling reorientation (fig 3.8a) within the inorganic cage [93], [104]–[108]. The estimations of the residence time for this reorientation is ranged from 3 ps to 10 ns, which are provided by different experimental methods like ultrafast 2D vibrational spectroscopy [105], QENS [93] and dielectric spectroscopy [108]. The estimations of the energy barrier for exciting this reorientation also fall into a range of 13.5 meV to 100 meV [73], [74], [93], [107], [114], [115]. Therefore, the in-cage reorientation of MA^+ is viable at temperatures as low as about 160 K. Ultrafast 2D-IR vibrational anisotropy and ab initio MD additional identified a subtler small degree rotational vibration of MA^+ dipole (fig. 3.8(a)) with the estimated residence time of about 300 fs

[105]. Because of the lower amplitude of vibration and faster residence time, this subtle vibration should process a smaller excitation barrier, thus should retain at a lower temperature. The self-rotation along C-N axis of MA^+ dipole (fig. 3.8(a)) does not affect the symmetry and has little effect on the hydrogen bonding to the surroundings, so such motion is always eligible. The molecular motion of MA^+ cation and corresponding characteristic time is summarised in tbl. 3.2.

These motions of MA^+ cations are restricted or forbidden in the lower temperature phases. In the tetragonal phase, all allowed motions are preserved, but the rate is slower because of the fewer thermal excitations and less orientation sites for MA^+ due to the reduction in geometric symmetry [103]. Furthermore, in the low-temperature orthorhombic phase, below 160 K, both the symmetry and excitation energy are further reduced. The translational tunnelling between cages is absent, meaning a localization of MA^+ cations in cages and the exact location of $CH_3NH_3^+$ can now be determined by experimental means. The reorientation inside cages of MA^+ dipoles is forbidden [103], although the *Pnma* space group rules out the possibility of polar ordering, antipolar ordering is possible and has been suggested by NPD results [76], in which MA^+ cations are seemingly ordered antiferroelectrically (AFE) in the [010] crystal direction. The small amplitude vibration of C-N axis shall always be allowed once there is sufficient thermal excitation. Although the equilibrium direction of C-N axis is pinned, the rotation along C-N axis is still free [74], [93], [103], [104].

The motions of $CH_3NH_3^+$ have an effect on the photo-induced electron-hole pair recombination, and so the photovoltaic performance. In MAPI, both valence and conduction bands are formed by the orbitals from the inorganic ions, so the photo-induced electron-hole pairs reside within the cage framework. Although MA^+ cation does not directly involve in the pair formation, its positive charged dipole could electrostatically assist in pair separation (fig. 3.8b), hence extends the recombination lifetime and improve the light-harvesting efficiency [104]. This interaction requires MA^+'s positive charge's wave function to overlap with the photo-induced electron's wave function, that is, an alignment of MA^+ dipole towards the electron, so a rapid

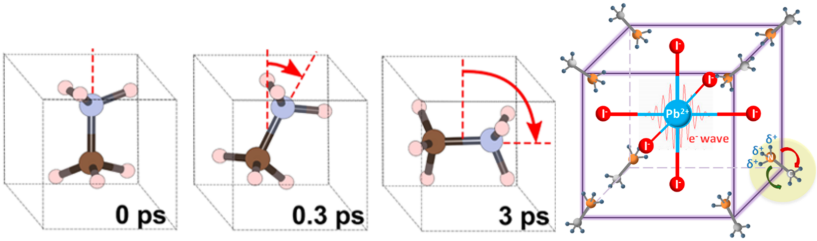

(a) (b)

Figure 3.8: (a) The illustration of MA^+ dipole' motions obtained from Ref. [105]: the C-N axis self-rotation (left), small amplitude C-N axis vibration (middle) and large amplitude tunnelling mediated reorientation (right). (b) Schematic depiction of MA^+ cations and the anionic PbI_3^- framework obtained from Ref. [104].

reorientation of MA^+ is favourable [104]. From the studies of fornamidinium (FA^+) and guanidinium substitution, this enhancement of carrier lifetime by cation-electron interaction is suggested to be generic in the perovskite structure and the motion of cation is not necessarily slower for a bulkier cation (or stronger electrostatic confinement of the cation in the cage), as FA^+ is bulkier but reorients faster than MA^+ [116], [117]. One last note, the substitution of halide ion also affects the organic cation's degrees of freedom [118].

3.2 Confined water

Water, with the chemical formula H_2O, molecules possess extremely large electric dipole moment, which enables long-range dipole-dipole interaction and thereby eligible for long-range ordering, for example, ferroelectricity. However, such an electric ordering has never been realized. In liquid water, the couplings of molecules are dominated by the stronger and shorter-range hydrogen bond, which does not align the dipole moments. In solid state, *i.e.* ice crystal in which the oxygen atoms are ordered, the hydrogen atoms are not fixed but are continuously undergoing frustrated fluctuation within experimentally accessible timescales [119], [120].

Before, the examination on the electric ordering of water molecules due to dipole-dipole interactions is approached by reorienting the intermolecular hydrogen couplings with the use of surface effects. Various designs have been attempted to fabricate low-dimension confined-water systems, for instance, quasi-1D ice confined in carbon nanotubes [121], [122], 2D monolayer ices grown on substrates [123]–[125] and 1D water chains [126]. From these experimental breakthroughs, ordering of oxygen atoms and unified polarization of dipoles are successfully but limitedly observed, so the reliability remains controversial. An incontrovertible corroboration of ferroelectric water is still lacking.

Instead of navigating, it is feasible, and perhaps better, to suppress or weaken the robust hydrogen coupling. The hydrogen bonding is a short-range effect with an interaction length 1-3 Å, whereas the electric dipole-dipole has a much longer interaction length 10-100 Å. Hydrogen coupling would be completely absent and electric dipoles coupling would dominate if the water molecules are confined with an optimal separation.

3.2.1 Beryl

Beryl crystal is a member of the gemstone family with the chemical formula $Be_3Al_2Si_6O_{18}$. The space group is $P6/mcc$ and the crystal structure is depicted in fig. 3.9(a). SiO_4 tetrahedra bond hexagonally via linkages with

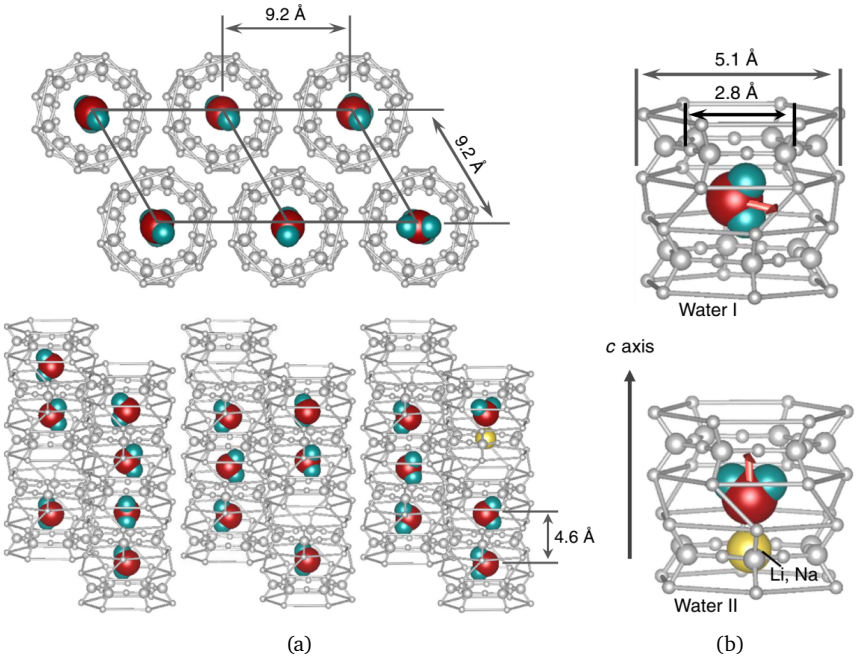

Figure 3.9: (a) Beryl crystal lattice with water molecules confined. (b) Depictions of type-I and type-II water molecules. Figures are reproduced from Ref. [14]

tetrahedrally coordinated Be ions and octahedrally coordinated Al ions, and form a six-membered ring. Rings then stack along the crystallography *c*-axis and construct nano-channels, whose cross-section is modulated by bottlenecks of 2.8 Å, the ring of Si atoms, separating cages of 5.1 Å in diameter, the ring of O atoms.

By synthesizing beryl crystals in an aqueous environment, water molecules could be trapped inside the cages. Due to the small sizes of H_2O molecules, of diameter 2.75 Å, up to four H_2O molecules can present inside the same cage. The H_2O molecules are distributed over the cages statistically.

Hydrogen bondings are supposed to be sufficiently suppressed between H_2O molecules from different cages, as cages within the same channel is

separated by 4.6 Å, whereas the distance between adjacent channels is 9.2 Å[14]. Unfortunately, strands of H_2O molecules inside the same cage would still be coupled strongly by hydrogen-bonding and prohibit the cross-case dipole-dipole interaction, and on the other hand, the empty cages have no dipole moment to interact with. Only the cages occupied by a single H_2O are participating in the inter-cage dipole-dipole coupling.

There are two possible orientations of the isolated H_2O molecule in cages: the dipole moment is aligned perpendicular (type-I) or parallel (type-II) to the c-axis (fig. 3.9(b)). Type-I has six polarization directions as it is the case of free H_2O molecule submitting to the six-fold potential imposed by the hexagonal symmetry. Type-II, on the other hand, can rotate freely along c-axis as it is formed when an impurity alkali ion (Li^+ and Na^+) is trapped at the bottleneck, which attract the oxygen ion due to Coulumb interaction. Since a positive ion presents, the dipole moment in type-II is rotated and is absent from coupling with in-plane neighbouring type-I dipoles, and only the weak van der Waals interaction between water molecules and crystal framework remains [14].

Type-I H_2O molecules are interacting strongly via dipole-dipole interaction (fig. 3.11) and, thereby, a ferroelectric ordering is predicted to form in a sea of type-I H_2O molecules. The interaction energy of a pair of dipoles can be expressed by the following equation [127]:

$$U_{\text{d-d}} = p^2 r^{-3} \tag{3.1}$$

where dipole moment of H_2O $p = 1.85$ D [128]. Using the spacing r mentioned earlier, the interaction energy between adjacent cages along the same channel and nearest cages in adjacent channels are estimated to be $U_{\text{d-d}} \approx 22$ meV and $U_{\text{d-d}} \approx 3$ meV, which respectively correspond to temperature $T \approx 260$ and 30 K. It is thus hypothesized to observe ferroelectric orderings in the vicinity of these temperatures in a beryl crystal filled with sufficient type-I H_2O molecules.

Instead of complete ferroelectric transition, incipient ferroelectricity is observed in the measurements of water-confined beryl [14]. A Curie-Weiss-

like temperature dependence (eqn. 2.27) is observed in the real dielectric permittivity ϵ' for the polarization $E \perp c$ (fig. 3.9(a)), but no complete transition occurs down to the base temperature of 30 mK. The macroscopic dipoles ordering nature is further evidenced by a softening of excitation in THz spectroscopy (fig. 3.10(c)). Such a soft excitation is always found in ferro- or antiferro-electric transition and in which the excitation would fully freeze out, *i.e.* frequency decreases to 0 Hz, at the transition temperature. Similar to the transition in dielectric permittivity, no complete freezing is observed on this soft excitation. This phenomenon is classified as the incipient ferroelectricity or quantum paraelectricity [46], in which quantum effects are present to suppress the ferroelectric phase transition and stabilize the paraelectric phase. Both the Curie-Weiss divergence in $\epsilon'(T)$ and soft excitation in THz measurements are absent from polarization $E \parallel c$ or in water-free beryl crystal (also $E \perp c$), indicating that those behaviours are originated, not form the beryl gemstone crystal lattice or type-II H_2O but, from the type-I H_2O molecules confined in the nanocages. A schematic map of the type-I H_2O interactions is illustrated in fig. 3.11.

One possible identity of the suppressing quantum effect is the rotational quantum tunneling of type-I H_2O dipoles in the six-fold potential well. The occurence of quantum tunneling was discovered by a neutron scattering experiment [129]. Seven peaks in the dynamical structure factor spectrum have an inverse temperature-dependence (fig. 3.12(a)), the opposite of vibrational motions, which is a characteristic signature of quantum tunneling motions. Additionally, the proton momentum distribution exhibit a six-fold interference pattern (fig. 3.12(b)), which is the consequence of coherently distributed (tunneling) ground state of a proton between the six equivalent minima of the crystal potential from beryl structure.

The dynamics of the interacting type-I H_2O dipoles are modelled as rigidly librating and rotating dipoles in a six-fold squared cosine potential [14],

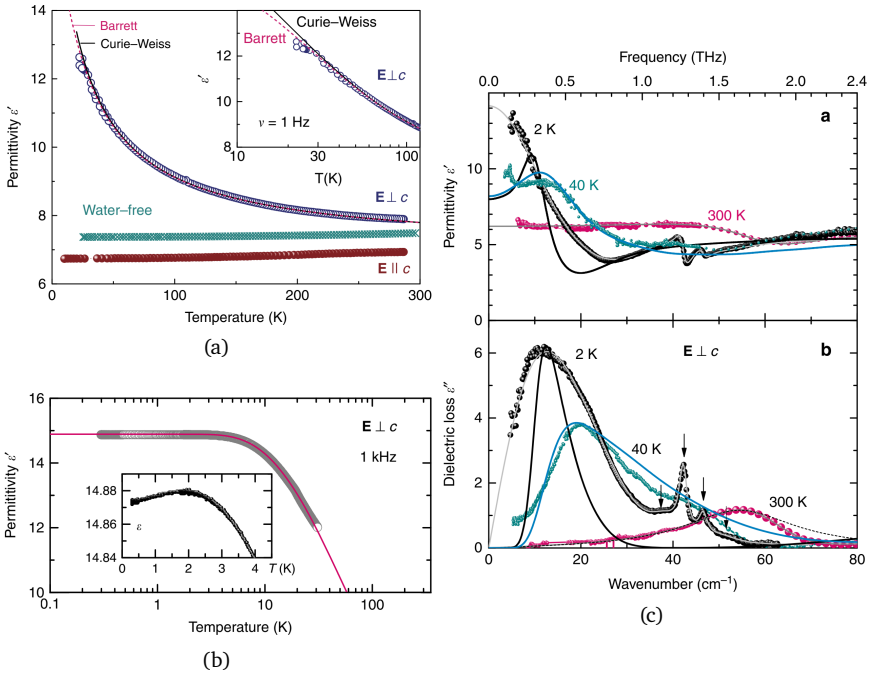

Figure 3.10: (a) Dielectric permittivity ε' of beryl crystals. (b) Low temperature ε' for $E \perp c$. (c) Temperature evolution of the dielectric permittivity and losses. Figures are reproduced from Ref. [14].

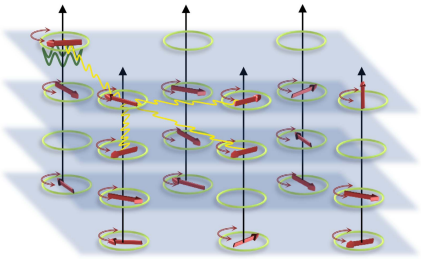

Figure 3.11: Illustration of the network of type-I waters' dipole moments in a beryl crystal. Figures are reproduced from Ref. [14].

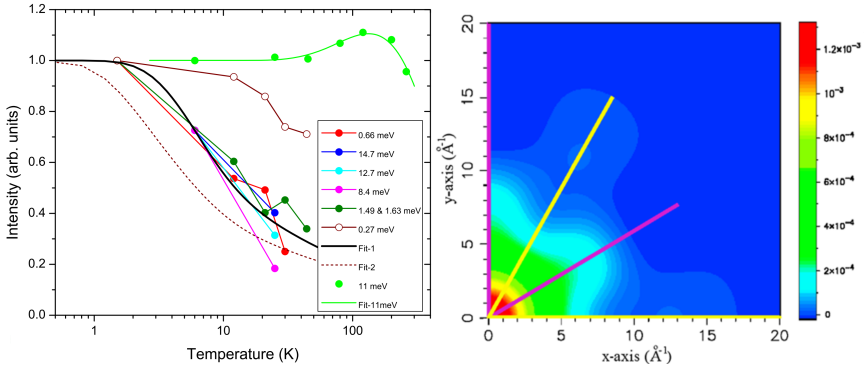

(a) (b)

Figure 3.12: (a) Inelastic neutron scattering spectra of water in beryl. (b) Projection of water proton momentum distribution in beryl. Figures are reproduced from Ref. [129].

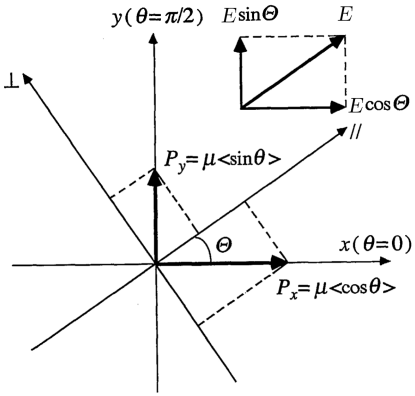

Figure 3.13: The configuration of librator-rotator model of H_2O dipoles in rotational potential. Figures is modified from Ref. [130].

[130]. The system's Hamiltonian is given by:

$$V(\theta) = -A\cos^2 3\theta \tag{3.2}$$

$$H = H_0 + H_1 \tag{3.3}$$

$$H_0 = \frac{1}{2I}L^2 - \frac{A}{2}(\cos 6\theta + 1) \tag{3.4}$$

$$\begin{aligned} H_1 = & -[\mu^2\gamma\langle\cos\theta\rangle + \mu\xi\cos\Theta]\cos\theta \\ & + \frac{1}{2}\mu^2\gamma\langle\cos\theta\rangle^2 \\ & -[\mu^2\gamma\langle\sin\theta\rangle + \mu\xi\sin\Theta]\sin\theta \\ & + \frac{1}{2}\mu^2\gamma\langle\sin\theta\rangle^2 \end{aligned} \tag{3.5}$$

The unperturbed term H_0 consists of the kinetic component with a moment of inertia I, an angular momentum L, and the potential component from a six-fold well (eqn. 3.2) with the depth A. The perturbation term H_1 takes use of the dipole moment magnitude μ, assumed scalar molecular field constant γ, and the inclination angle Θ between the external field E and the $\theta = 0$ axis (fig. 3.13). Afterwards, through a series of theoretical treatments, the dielectric permittivity $\varepsilon'(\omega)$ is estimated:

$$\varepsilon'(\omega) = 1 + 4\pi N\frac{\phi(\omega)}{1-\gamma\phi(\omega)} \tag{3.6}$$

where $\phi(\omega)$ is the polarizability of the dipoles (for details, please read ref. [14]). Fitting of eqn. 3.6 to THz data estimated that the depth of the crystal potential well $A = (1.41 \pm 0.05)$ meV, coupling of the H_2O dipole to the mean-field generated by other dipoles $\mu^2\gamma = (1.33 \pm 0.11)$ meV [14].

Confined D_2O systems can also be created using the same synthesis recipe but in deuterated water. D_2O, in principle, behaves exactly like H_2O electronically only with a heavier atomic mass. The infrared absorption spectra of H_2O and D_2O are reported by Ref. [131] and reproduced in fig. 3.14. The D_2O spectra resemble a lot with the H_2O one but shifted to a lower wavenumber, which is due to the hindered vibration of heavier mass. With

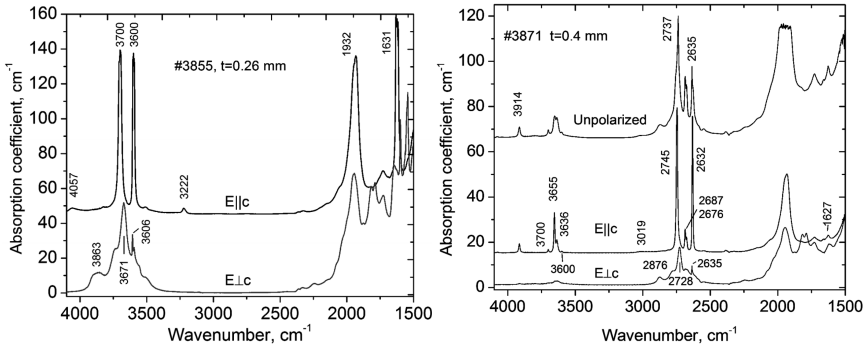

(a) (b)

Figure 3.14: (a) Polarized infrared absorption spectra of H_2O molecules in the beryl structure. (b) Polarized and unpolarized infrared absorption spectra of D_2O molecules in the beryl structure. Figures are reproduced from Ref. [131].

heavier mass, it is also expected to lower the frequency of the soft mode and thus lead the system closer to the full ferroelectric transition.

Besides substituting H_2O with D_2O, the application of external pressure may also be beneficial to the formation of ferroelectric order. External pressure could bring the water molecules even closer and enhance the dipole-dipole interaction so that the quantum fluctuation is overcome and suppressed. Although beryl structure is rigid, as the axes are only shrunk by 1% at 5 GPa (fig. 3.15), preliminary changes in ε' of water-confining beryl are expected to be induced by 10 GPa of external pressure because the dipole moment of H_2O is large and the quantum fluctuation shall not be too pronounced.

Finally, the existence of type-II H_2O dipoles is also a convincing obstacle to ferroelectricity. The reasoning is that the alkali ion coordinates beyond the neighbouring H_2O molecules and from a chemically correlated cluster, that is neither ordered nor paraelectric. Less alkali ion impurity, namely less type-II H_2O concentration, should also promote the realization of ferroelectricity in this confined water system.

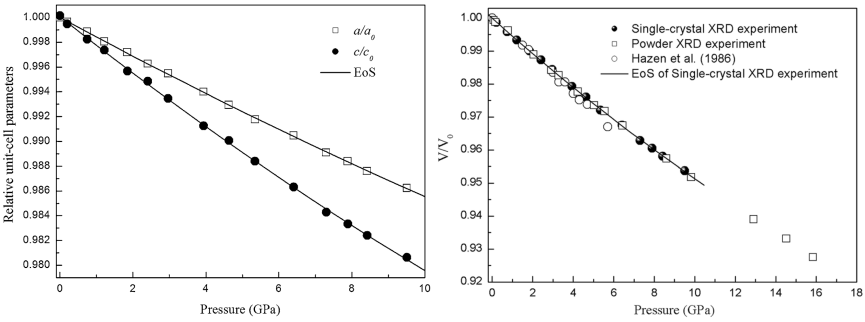

(a) (b)

Figure 3.15: (a) Axial compresion a/a_0 and c/c_0 (b) volume under physical pressure obtained from single-crystal X-ray diffraction measurements. Figures are reproduced from Ref. [94].

Chapter 4

Experimental Methods

Dielectric spectroscopy refers to measurement techniques determining the interaction between electromagnetic (EM) radiation and matters. Depending on the operation frequency range, different electronic setups have to be deployed (fig. 4.1(a)).

In this thesis, a pressurized setup is developed to measure the dielectric properties of samples from ambient pressure up to 8 GPa within 10^{-2} to 10^{8} Hz.

4.1 Ambient pressure

For radio-frequency (Hz-MHz), the technique being used is the auto-balance bridge method [18], [22]. The equivalent circuit is shown in fig. 4.1(b). The sample is sandwiched between a capacitor and a fixed and known complex voltage U_s^* is applied across, which result in a complex current I_s^*. I_s^* collides with another current flow I_c^*, generated through a fixed and known impedance Z_c^* and a controllable amplitude-phase generator U_c^*, at point P_i. The residue current I_0^* is monitored and U_c^* is adjusted until I_0^* becomes zero, *i.e.* the bridge is balanced. In the balanced state, the sample

complex impedance is calculated:

$$Z_s^*(\omega) = \frac{U_s^*(\omega)}{I_s^*(\omega)} = \frac{U_s^*(\omega)}{U_c^*(\omega)} Z_c^*(\omega) \tag{4.1}$$

Temperature control between room temperature to 4 K is performed by commercial helium-flow cryostats bought from CryoVac GmbH & CO KG KONTI , and commercial temperature controllers, Lakeshore Model 336 and Model 340. A custom-made holder is designed and manufactured for inserting the sample / pressure cell deep into the cryostat.

Measuring instruments employed in this thesis are the Agilent 4294A precision impedance analyzer (with ideal operation frequency range from 40 Hz to 110 MHz and alternating voltage signal level from 5 mV to 1 V_{rms} [133]) and Novocontrol Alpha-A High-Resolution Impedance Analyzers (with ideal operation frequency range from 3 μHz to 40 MHz and alternating voltage signal level from 100 μV to 3 V_{rms} [134]). However, from the in-house calibrations and test measurements, data near the high operation limit would be severely spoiled by the spurious contribution from the fixtures, even if compensation is performed (sec. 4.1.1). Therefore, since a custom-made holder is present in the measurements, the frequency window is reduced to 40 Hz-10 MHz for Agilent 4294A and 1 mHz-10 MHz for Novocontrol Alpha-A.

4.1.1 Compensations

The raw signal received by the network analyser is contaminated by the contributions from the fixtures, cables and connectors, for example, residual impedance, admittance and electrical length [132]. To eliminate these unwanted effects and acquire the pure signal from the samples, signals from test objects of two electrical limits are collected and are compensated in the analysis of actual data.

An equivalent circuit for the measurement setup is illustrated in fig. 4.2(a). The residuals of the circuit are assumed to be represented by the L/R/C/G components, namely, residual impedance and stray admittance. These resid-

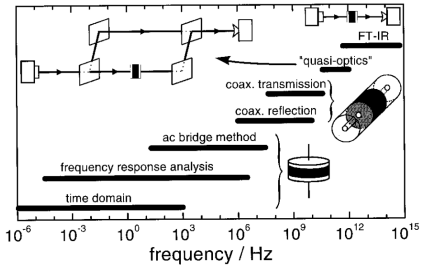

(a)

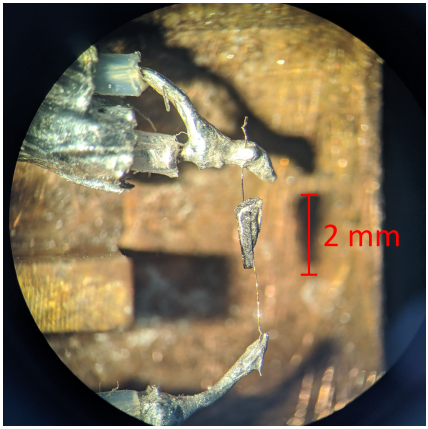

(c)

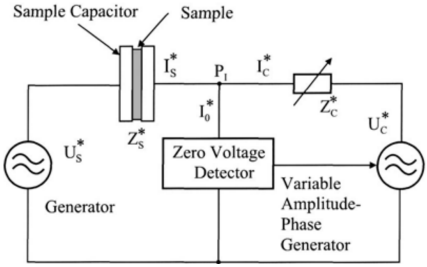

(b)

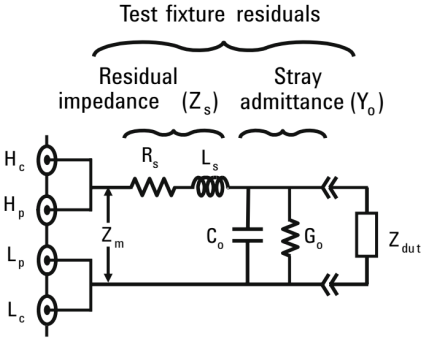

(d)

Figure 4.1: (a) Methods that are available for the board range dielectric spectroscopy (reproduced from ref. [22]). (b) Equivalent circuit diagram of the auto-balancing bridge method (reproduced from ref. [18]. (c) a photo of the setup measured in this thesis at ambient conditions. (d) [132].

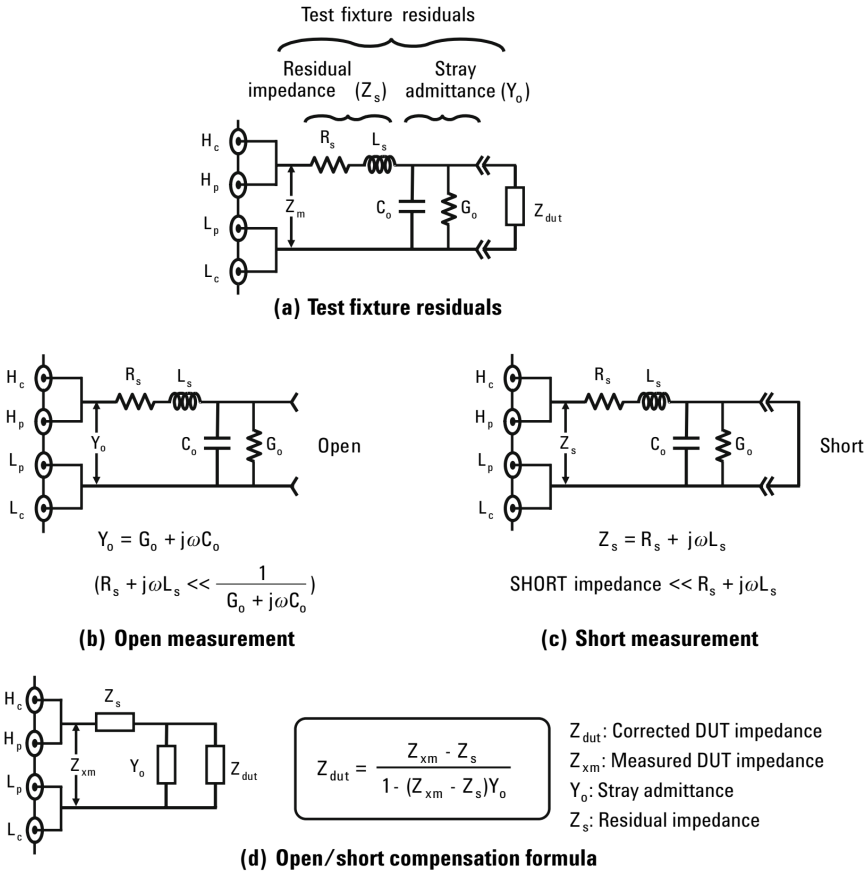

Figure 4.2: Equivalent circuits of (a) test fixture residuals, (b) open compensation, (c) short compensation and (d) simplified test fixture residuals. The figures are reproduced from ref. [132].

ual components are determined from the results of open (fig. 4.2(b)) and short (fig. 4.2(c)) compensations. Correction of the estimation to sample impedance is then performed with the use of the equation provided in fig. 4.2(d).

For the sake of practical convenience, the equation is hence separated in real and imaginary parts in terms of $A_{o/s}$ (the parameters obtained primarily from compensation measurements) for readily applications:

$$R_{\text{dut}} = \frac{\begin{array}{c}(R_{\text{xm}}-R_s)[1-G_o(R_{\text{xm}}-R_s)+\omega C_o(X_{\text{xm}}-X_s)] \\ -(X_{\text{xm}}-X_s)[G_o(X_{\text{xm}}-X_s)+\omega C_o(R_{\text{xm}}-R_s)]\end{array}}{\kappa} \tag{4.2}$$

$$X_{\text{dut}} = \frac{\begin{array}{c}(X_{\text{xm}}-X_s)[1-G_o(R_{\text{xm}}-R_s)+\omega C_o(X_{\text{xm}}-X_s)] \\ +(R_{\text{xm}}-R_s)[G_o(X_{\text{xm}}-X_s)+\omega C_o(R_{\text{xm}}-R_s)]\end{array}}{\kappa} \tag{4.3}$$

$$\kappa = \begin{array}{c}(1-G_o(R_{\text{xm}}-R_s)+\omega C_o(X_{\text{xm}}-X_s)^2 \\ +(G_o(X_{\text{xm}}-X_s)+\omega C_o(R_{\text{xm}}-R_s))^2\end{array} \tag{4.4}$$

4.1.2 Intensive physical quantities calculation

The geometric factor of the sample is estimated by assuming a uniform cross-section geometry, *e.g.* a cylinder or orthorhombic with area A and electrodes' separation d (fig. 4.3). Thus, the intensive physical quantities, such as dielectric permittivity ε^*, are calculated via the following equations:

$$\varepsilon'(\omega) = \frac{d}{A}\frac{C(\omega)}{\varepsilon_o} = \frac{d}{A}\frac{1}{\varepsilon_o\omega}B(\omega) \tag{4.5}$$

$$\varepsilon''(\omega) = \frac{1}{\varepsilon_o\omega}\sigma'(\omega) = \frac{d}{A}\frac{1}{\varepsilon_o\omega}G(\omega) \tag{4.6}$$

There are two inappropriacies from this estimation model. First, the crystal might not be in an ideal cylindrical or orthorhombic shape, so the geometric factor is not as straightforward as d/A in the estimation. Second, some field lines on the edge are not penetrating the crystals but are neglected from the estimation (fig. 4.3). Nonetheless, these errors are minor because the former only affects the numeric prefactor and won't be deviated more than an order and the latter can be avoided by not covering the entire surfaces of

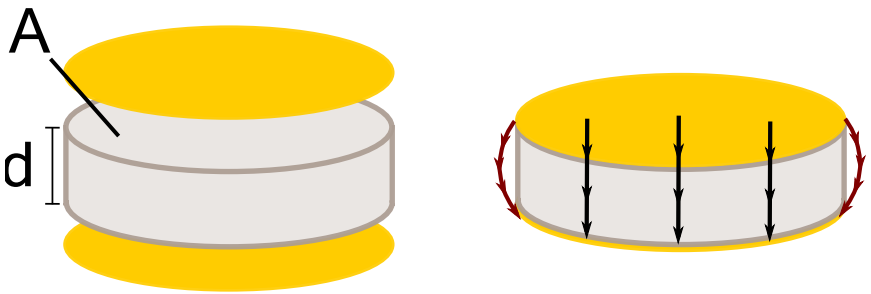

Figure 4.3: Schematic drawings of the electrodes on the sample. Electric fields lines are illustrated on the right figure. The stray field lines which do not penetrate through the sample are coloured dark red to indicate them as a minor source of error since these are neglected in the quantities calculation.

the crystal with electrodes but leave the boundaries.

4.2 Under pressure

4.2.1 Diamond anvil cells (DAC)

Diamond anvil cells (DAC) are employed to apply pressure because of its adequately high operating pressure range, in order of 1-100 GPa. A DAC consists of two opposing diamond anvils, a gasket and the cell body (fig. 4.4(a)). The operation principle of a DAC relies on the highest hardness of opposing diamonds to maximally amplify and secure pressure with the help of the comparably hard gasket.

4.2.1.1 Diamond anvils

Anvils are blocks of material with a flattened top surface. In DACs, the amplification of pressure is directly proportional to the surface area ratios between the top and bottom surfaces of the anvils.

Nowadays, diamond anvils are mostly artificially synthesized (high-pressure, high-temperature technique) and the dimensions can be carefully controlled. The smaller the culet, the top surface of an anvil, the higher pressure it can reach with the trade-off of space for operation and step size. The size of

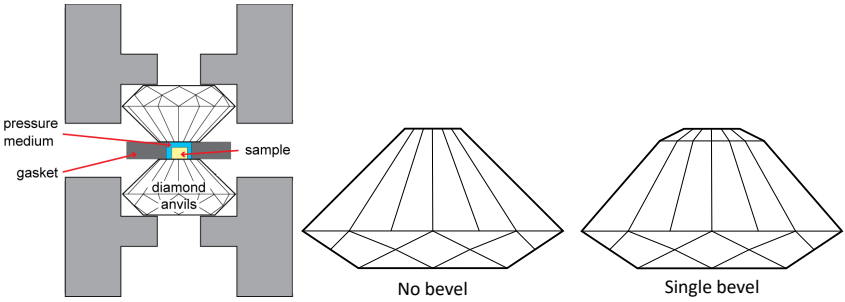

Figure 4.4: (a) Schematic depiction of the operation principle of a diamond anvil cell. (b) Side-views of diamond anvils with no bevel (left) and with a single bevel (right).

Targeted pressure ceiling	Culet size (diameter)
$<$ 20 GPa	500-1000 μm
20 - 100 GPa	100-500 μm
$>$ 100 GPa	$<$ 100 μm (with bevels)

Table 4.1: Typical culet size and pressure ceiling relation.

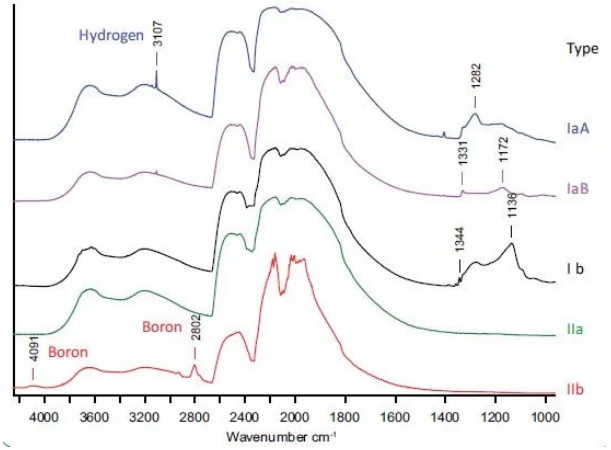

Figure 4.5: FTIR spectra of different diamond types reproduced from Ref. [135].

anvil is thus chosen depending on the targeted pressure range. The typical relation is listed in tbl. 4.1 .

Apart from the primitive design of a straight hypotenuse, bevel(s) is(are) often made on anvils to relieve the force at the culet edge. As illustrated in fig. 4.4(b), the angle at the culet edge is reduced with bevels. This can greatly improve the bearing-force limit of the anvil, so both the pressure ceiling and lifespan are enhanced.

Diamonds are classified into several type due to their nitrogen content. Figure. 4.5 shows the FTIR spectra of each diamond types. Nitrogen content is reflected by the absorption between 1000 - 1500 cm^{-1}. Therefore, for op-

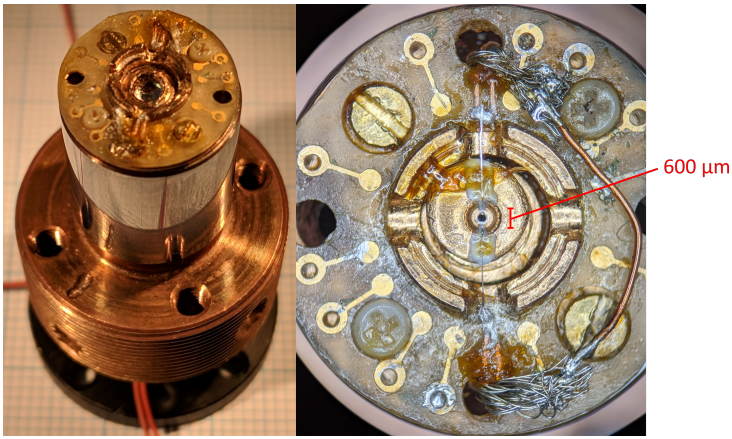

(a) (b)

Figure 4.6: (a) Photo of the DAC deployed in this study. (b) Top view at the gasket level inside the DAC.

tical (particularly IR) measurements, usage of type-II diamonds is necessary. For dielectric (and other non-optical measurements), either type of anvils are usable.

In this thesis, the diamond anvils (including the entire cell body) are commercial products from Almax Easylab (fig. 4.6). They are of type Ia with a culet of 600 μm in diameter with a single bevel up to 700 μm at 8°.

4.2.1.2 Gasket

The cavity for pressurization is provided by a hole in the centre of the gasket, which is sealed by the opposing diamonds from the two sides during application of pressure. The hole diameter is advised to be shorter than 1/3 of the culet diameter; otherwise, the pressure ceiling is reduced.

As the component responsible for pressure confinement, the gasket also has to have very high hardness but is not brittle as a diamond is. Several options of materials can be found across the literature, and the decision is made

Gasket materials	Usage
T301 stainless steel (work-hardened)	All-purpose
Re / W	Ultrahigh pressure (> 100 GPa)
Inconel / Re	High temperature
cBN / MgO / Al_2O_3	Electrical
BeCu	Magnetic

Table 4.2: Material options for the gasket. The table serves as a rudimentary overview. Actual gaskets frequently consist of adjustments tailor-made for the measurements, for example, composite gasket.

depending on the measurement technique and the material's availability [136]. An overview is listed in tbl. 4.2.

In this work, beryllium copper (BeCu) was deployed as the gasket material because of its availability at the time. BeCu has high enough hardness to withstand pressure up to 15 GPa. The insulation was tackled by modification around the cavity, which is explained in detail in the later section sec. 4.2.2.

4.2.1.3 Pressure medium

The cavity is filled with a pressure medium to redistribute the force and so provide a hydrostatic pressure. A substance with zero shear strength would be ideal. In practice, mediums from gases to solid powder can be chosen depending on the technique, chemical properties of the sample and availability.

Gas media are necessary when ultrahigh pressure is aimed, for example, inert gases and nitrogen. Auxiliary instruments are required because a high gas density inside the cavity can only be realized in a low temperature and high gas pressure environment. The filling process is ill-controlled as it takes place deep inside the cryostat and gas chamber, which leads to a higher failure rate even for experienced user.

Solid media are the most manageable option, for example, NaCl and

Medium	Hydrostaticity	Concerns	Main usage
Gas *e.g.* He, Ne	Nearly ideal	Filling requires specific tools	Ultrahigh pressure (>100 GPa)
Liquid *e.g.* water, methanol/ ethanol	High	Chemically active, Volatile	High pressure
Oil *e.g.* Daphne, Glycerin	Good	Solidification	Normal (0-15 GPa)
Solid *e.g.* NaCl, CsI	Acceptable	Inhomogeneity	Optical measurements

Table 4.3: Options for pressure medium. In practice, the optimal choice is conditional, depending on the sample's chemical properties, experiment settings and availability of instruments.

CsI. The downside is relatively lower hydrostaticity. Nonetheless, it can be improved by perfect balanced padding of the medium around the sample piece. Also, in some cases, a stagnant solid is needed. For instance, solid media is used in IR reflection measurement to press the sample against the anvil, so no reflection through the medium is involved.

Liquid media are the balance between gas and solid, so they are the most practical. The achievable hydrostaticity varies vastly among kinds of liquid. The highest hydrostaticity liquids include mixtures of light-molecule solvent (*e.g.* 4:1 methanol/ethanol, 16:3:1 methanol/ethanol/water) and water. The drawbacks are high volatility and low chemical inertness. More manageable and applicable choices include daphne oil, glycerin oil and silicon oil. However, these oils often begin solidification at moderate pressure, about 5 GPa, and the hydrostaticity decays from that point onwards.

In this work, Daphne oil was picked as the pressure medium. It is because the targeted maximum pressure was beyond 5 GPa but not as high as 10 GPa.

Besides, modification of cavity and wires arrangement pose a need of time for careful manual operation, so low volatility is also desirable.

4.2.2 Gasket preparation

A series of procedures are developed to optimize the endurance and integrity of the pressurized cavity, so a higher pressure can be reached and the lifespan of the DAC can be prolonged [137], [138]:

4.2.2.1 Preindendation

The original state of a gasket is in simple plate shape (fig. 4.7(b)). Before the hole drilling, the gasket is first compressed by the diamond anvils to avoid deformation during the pressurization for actual measurements. The gasket is inserted into the DAC and compressed by the diamond anvils with a force sufficient to reach the target pressure (*c.f.* sec. 4.2.5.1). The compressed region of the gasket is thinner but denser and hardened (fig. 4.7(c)), and is going to maintain its shape until a greater force is applied. By doing so, a deformation of the pressurized cavity during the measurement is prevented.

4.2.2.2 Hole drilling

The pressure cavity needs to be uniform and smooth, so minimum pressure inhomogeneity is built up on the inner surface, which would turn into a bottleneck for the pressure limit. Since hard materials are chosen for the gaskets, traditional mechanical drilling is difficult to guarantee the integrity of the hole. Therefore, the electrical discharge machining (EDM) technique is adopted. More advanced techniques include laser and focused ion beam drilling, which have an additional advantage of being applicable to insulating materials.

The mechanism of EDM makes use of the electrical discharge process that appears between electrodes when they are subjected to a substantially huge voltage difference [139]. Fig. 4.8(a) illustrates the schematic design of an EDM machine. The workpiece, *i.e.* the gasket in our case, is electrically

(a)

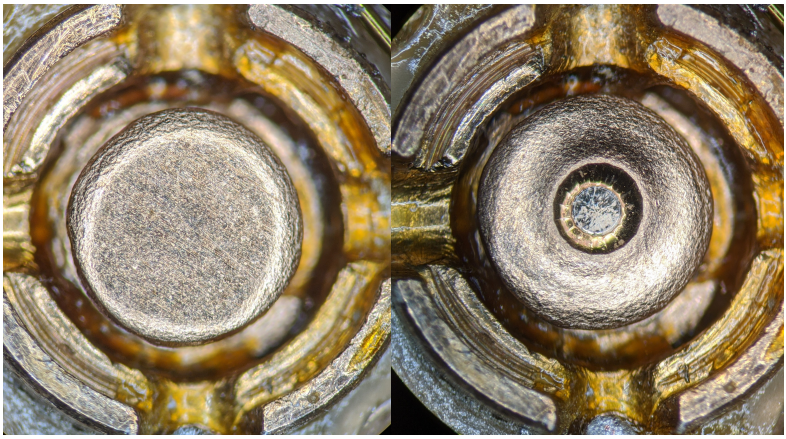

(b) (c)

Figure 4.7: (a) A schematic sideview sketch of the gasket before and after pre-intendation. (b)-(c) A photo of the gasket before (left) and after (right) pre-intendation.

connected with the fixture that is connected to the positive terminal of the pulse generator, while the negative terminal is connected to a drilling tool with the desired shape, so a sufficient voltage difference is built up between the workpiece and the drilling tool. The electric field between electrodes intensifies when the electrodes are brought closer. When the separation drops to a threshold, the spark gap, an electrical discharge will occur across the spatial gap. The discharge spark is focused onto a tiny region, the sharpest point on the workpiece's surface, so strong heating is generated at that point and vaporizes that portion of material. The same discharge sparking repeats whenever the separation between two points from each electrodes is below the spark gap, and thereby a volume in the shape of

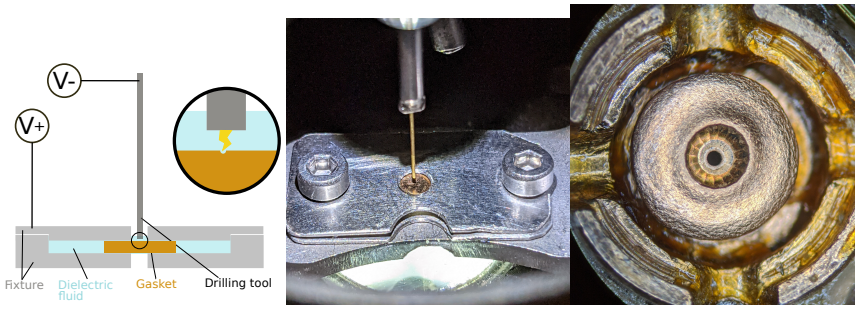

(a) (b) (c)

Figure 4.8: (a) A schematic sketch of an EDM setup. (b) A photo of the actual EDM setup employed in this study. (c) A photo of the EDM-drilled and pre-indented gasket.

the drilling tool is burnt off from the workpiece. To improve the efficiency, the electrodes are immersed in non-conductive dielectric fluid to prevent discharge towards the environment, remove burnt-off material via the flow induced by the discharge, and absorb heat from the machining.

In the case of our setup, a cylindrical cavity with a diameter of about one-third of the diamond culet is aimed, so the drilling tool is chosen to be a tungsten rod with a diameter of 250 μm. The outlook of the actual station and the drilled gasket are shown in fig. 4.8(b) and fig. 4.8(c).

4.2.2.3 Channels for wires

The idea of conducting dielectric spectroscopy under pressure is to enclose the sample and the capacitor inside the pressurized cavity of the DAC. The outlook and top view of the DAC are depicted in fig. 4.6. Coaxial cables were inserted through the cell body and were opened right outside the gasket seat (fig. 4.6(b)), so the length of unshielded wires was minimized for the maximum protection of the signal.

In the geometry of a dielectric measurement, a physical connection is present. Wires from the contacts need to go across the border of the pressur-

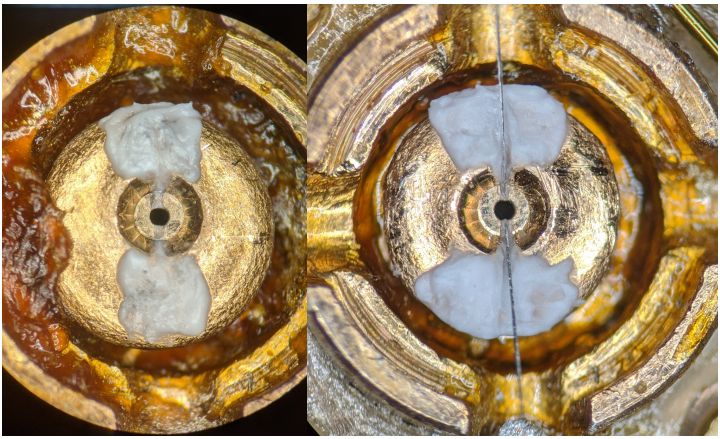

(a) (b)

Figure 4.9: (a) A photo of the gasket with channels carved and filled with insulating epoxy. (b) A photo of the gasket with platinum trails installed on the channels.

ized cavity to transport the signal. In order to prevent conductive connections between wires and the gasket, an insulating channel is made on the wall of the cavity.

Among the literature and commercial products, there exists the adaptation of sputtered leads embedded on the diamond anvils [140], [141]. In which cases, insulation of the leads from the metallic gasket is installed on the anvil with high precision, so no defect is introduced onto the gasket, which would result in higher expected pressure and stability. However, the preparation difficulty is not dramatically reduced since the electrical connection between the sample and leads has to be done on the small culet surface.

The idea adopted in this thesis is to carve a trench from the pressurized area and fill the trench with an insulating but also hard material. The carving is performed by EDM or by hands. The width and depth of the trench are minimized as soon as successful insulation is ensured to maximumly preserve the integrity of the cavity (fig. 4.9(a)). The trench is filled with hard epoxy

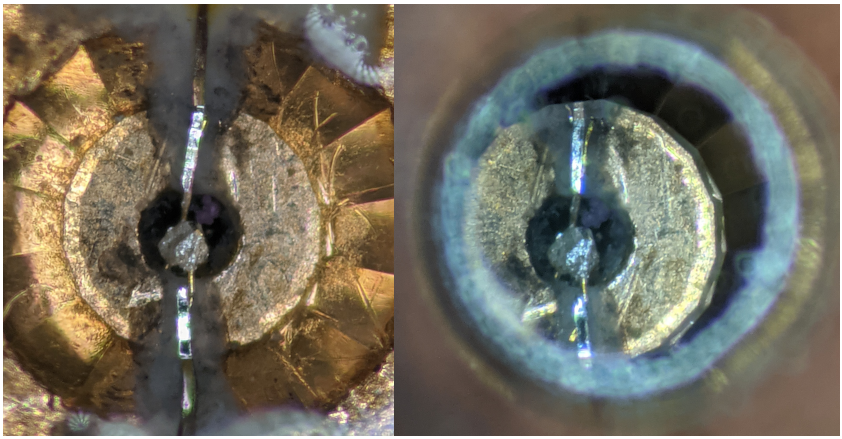

(a) (b)

Figure 4.10: (a) The cavity with sample and ruby spheres inserted, ready for cell closure. (b) The pressurized cavity after cell closure.

resin, a mixture of epoxy Stycast 1266 and alumina powder in this study, to restore the shape of the cavity.

A common failure of the DAC is the connection lost due to the cut of wires at the border of the pressurized area. To reinforce the connection across the border, a thin strip of platinum foil is laid on top of the insulating material (fig. 4.9(b)).

4.2.3 Cell filling and closure

After careful insertion of the sample with metallic contacts fall firmly onto the platinum tracks, ruby spheres are also inserted beside the sample and the cavity is then completely filled with a pressure medium. Figure. 4.10(a) depicts the cavity ready for closure, where the sample, ruby spheres and medium are in place.

During the closing of the DAC, it is advised to keep monitoring the cavity since some problems might occur, for instance, displacement of wires from

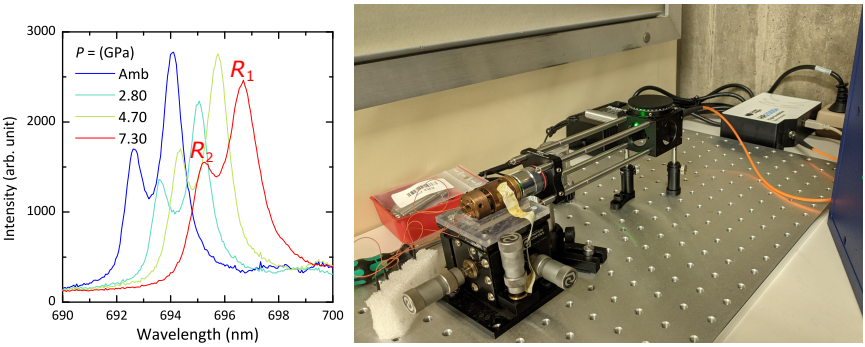

(a) (b)

Figure 4.11: (a) The ruby fluorescence spectra under pressure. Both R_1 and R_2 peaks shift to higher wavelength with higher pressure and the relation $P(\lambda)$ of R_1 is given by Eqn. 4.7. (b) A photo of the ruby determination station.

the platinum trails and trapping of air bubbles. A successful DAC closure, as depicted in fig. 4.10(b), should have a firm contact between wires and the platinum trails, no air bubble and a clear view of the ruby spheres.

4.2.4 Pressure determination

The pressure inside the cavity is determined by the ruby fluorescence. Ruby has strong fluorescence peaks R_1 and R_2 at ≈ 694 and 692 nm at ambient conditions. The peak wavelength of R_1 is found to shift approximately linearly with pressure. The relation is given by the following equation [142], [143]:

$$P(\lambda) = \frac{A}{B}\left[\left(\frac{\lambda}{\lambda_a}\right)^B - 1\right] \tag{4.7}$$

where $A = 1904$ GPa, $B = 7.665$ for hydrostatic conditions and λ_a is the ruby fluorescence R_1 line wavelength at ambient pressure. Since the ruby spectrum can be measured precisely, the accuracy of pressure determination is high. Fig. 4.11(b) shows the station for ruby fluorescence measurement.

4.2.5 Setup characterisation

4.2.5.1 Torque to pressure relation

The method of force application of the particular DAC in this thesis is through screw-tightening. The fine control of applied force is conducted using a torque screwdriver. Such that, a record of torque on the screws, *i.e.* applied force, and the resultant pressure was documented for the future cell preparation (*c.f.* sec. 4.2.2).

Fig. 4.12 plots the pressure-torque relation $P(\tau)$ of one of the measurement cycles. This setup used a pre-intended BeCu gasket with thickness of 100 μm (from 500 μm) and the diamond anvils specified in sec. 4.2.1.1 [1]. The pressure inside the cavity starts to build when the torque applied on the tightening screws exceeds $\approx$ 12 cNm. The pressure rises linearly with torque at low pressure and experiences a drop in slope at high pressure ($>$ 4 GPa) mainly because of the emergence of deformation of the cavity. With records similar to this, it is now known that a preindentation with more than 40 cNm is required for reaching 6 GPa, and likewise for estimations with any targeted pressure.

4.2.5.2 Compensation

Compensations are also performed in DAC measurements (*c.f.* sec. 4.1.1). Figures. 4.13-4.15 plot the compensation data inside DAC. There is no apparent temperature-dependence nor pressure-dependence from the DAC setup. Also, the magnitude of the stray capacitance (fig. 4.13(d)) is in the order of 1 pF, which is orders of magnitude lower compared to the most of the interested dielectric materials whose capacitance are in general above the order of 1 nF.

[1] It is important to note that a different record should be referenced if any of the followings is changed: gasket material, gasket's initial and final thickness, culet's diameter, and anvil's bevels.

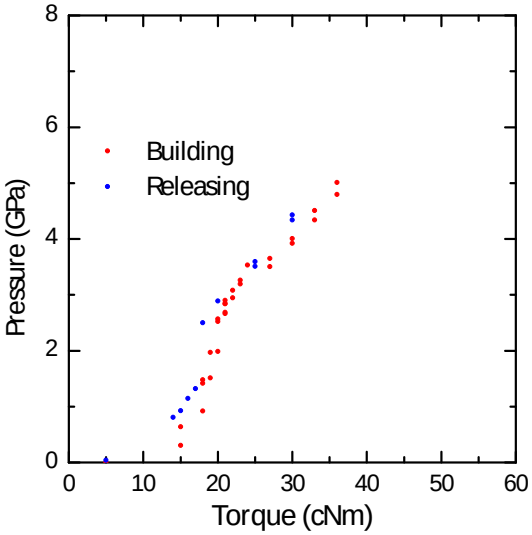

Figure 4.12: The pressure and torque relation of one pressure cycle. This DAC consists of a BeCu gasket of 100 μm (pre-intended from 500 μm) and the diamond anvils with culet of 600 μm with single-bevel up to 700 μm at 8°(as specified in sec. 4.2.1.1).

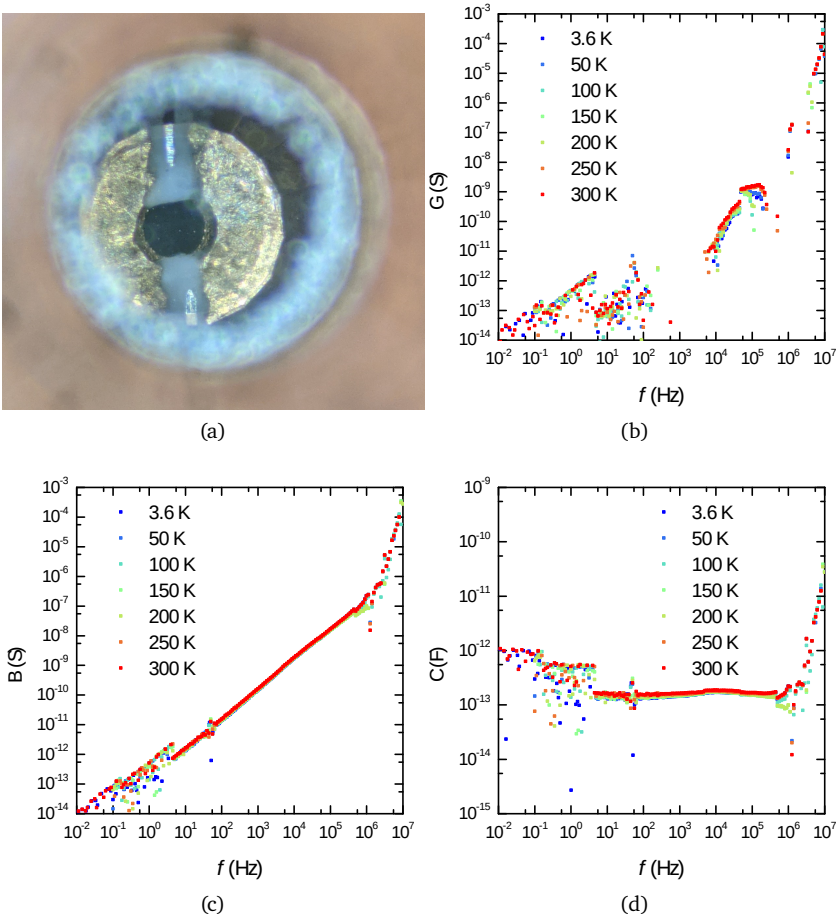

Figure 4.13: Open compensation of DAC: (a) photo of the cavity of an open-circuited DAC. (b)-(d) frequency dependence of conductance G, susceptance B and capacitance C at ambient pressure.

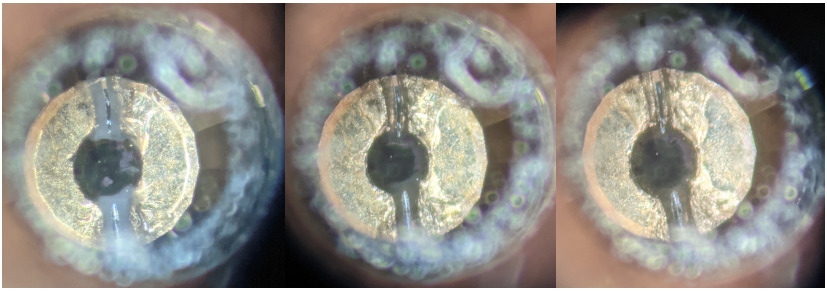

(a) (b) (c)

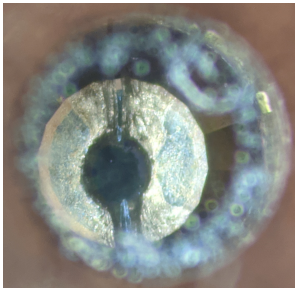

(d)

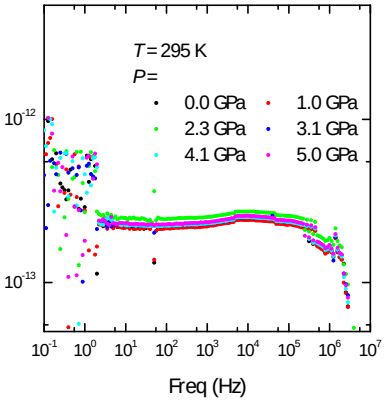

(e)

Figure 4.14: Open compensation of DAC under pressure: (a)-(d) photos of the cavity at 0, 2.3, 4.1, 5 GPa. (e) pressure evolution of the capacitance C at room temperature.

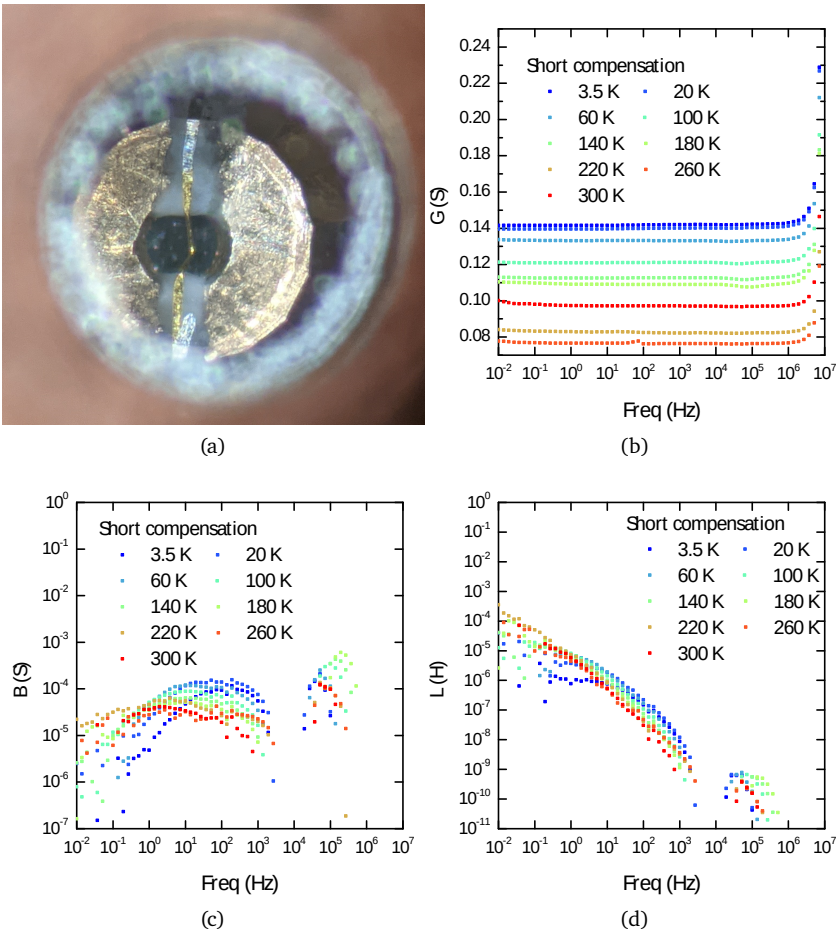

Figure 4.15: Short compensation of DAC: (a) photo of the cavity of a short-circuited DAC. (b)-(d) frequency dependence of conductance G, susceptance B and inductance L.

Chapter 5

Hybrid perovskite $CH_3NH_3PbX_3$ (X = I, Br, Cl)

5.1 Sample preparations

Hybrid inorganic-organic halide perovskite samples presented in this study were provided by Dr. Márton Kollár and Dr. Endre Horváth from Laboratory of Physics of Condensed Matter, Institute of Physics (IPHYS), École Polytechnique Fédérale de Lausanne (EPFL). The method of crystal synthesis is solution growth [144]. Figure. 5.1 depicts the photos of the high quality $CH_3NH_3PbX_3$ (MAPX) single crystals. The crystal dimension is about 3 mm×3 mm×3 mm for each halide. No x-ray diffraction experiment was done on our crystals; nonetheless, by comparing the crystal's shapes and the dielectric spectra with the literature [80], the crystallographic direction could be reliably identified.

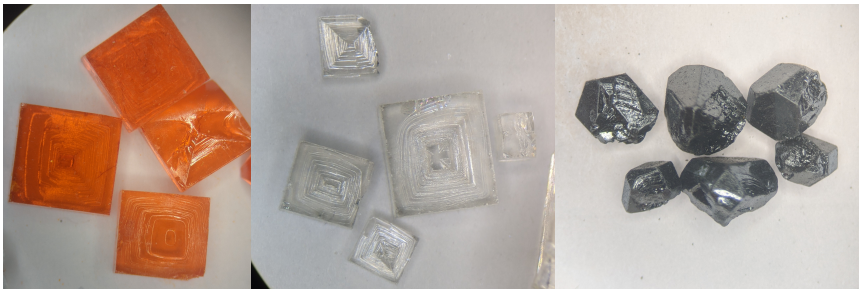

(a) (b) (c)

Figure 5.1: High-quality, sharply-edged single crystals of (a) MAPB, (b) MAPC and (c) MAPI synthesised and provided by collaborators.

5.2 Dielectric properties of MAPX at ambient pressure

In this section, the properties of $CH_3NH_3PbX_3$ series (X = I, Br or Cl) at ambient pressure are presented. These measurements were not solely conducted by the author of this thesis, but the results of these jointed projects are briefly summarised here to set up the foundation for the expectations of the the measurements under pressure, which are presented in the later section (sec. 5.3).

5.2.1 $CH_3NH_3PbBr_3$ (MAPB)

The real permittivity (ε') of MAPB from all three axes at ambient pressure is plotted in fig. 5.2. Three transitions take place at around 145 K, one more than what has been observed by literature. The nature of the additional transition is unclear. Another discovery is a relaxation behaviour at low temperature of about 25 K in all three axes. The detailed study on MAPB at ambient pressure was documented in ref. [145]. The temperature dependence of the relaxation time is found to be linear [145], implying non-glassy nature of the relaxation.

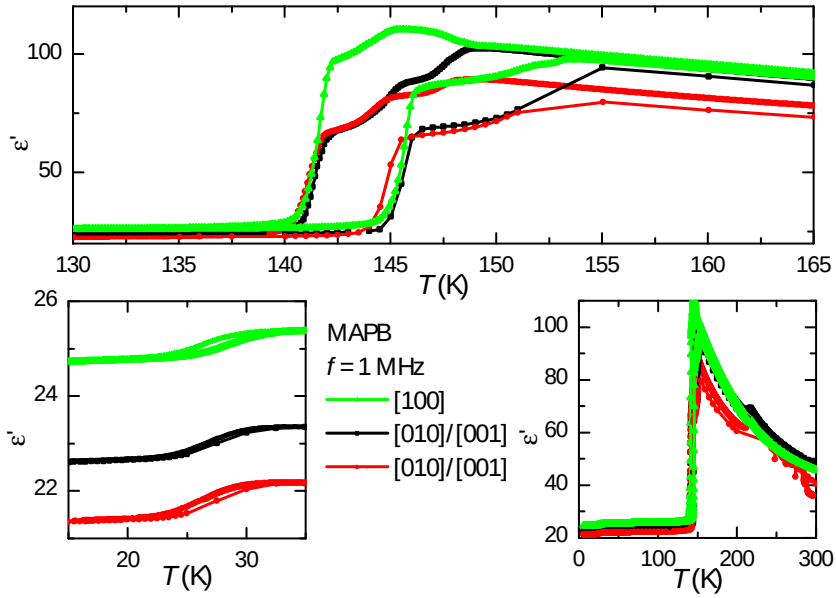

Figure 5.2: Real permittivity of MAPB from all axes at ambient pressure with $f = 1$ MHz. Three consecutive structural transitions are observed around 145 K, one more than literature [79], [80]. At unreported low temperature, a relaxation feature is found at 25 K for all 3 axes.

5.2.2 $CH_3NH_3PbCl_3$ (MAPC)

Figure 5.3 displays the temperature and frequency dependences of the real permittivity ε' of MAPC. Two structural transitions are identified at 184 K and 178 K (fig. 5.3(b)). No relaxation behaviour takes place at low temperatures. At high temperatures, a stoichiometric polarization is observed, as clearly seen in the frequency spectra (fig. 5.3(c)).

5.2.3 $CH_3NH_3PbI_3$ (MAPI)

Figure 5.4 exhibits the temperature and frequency dependence of ε' of MAPI. In agreement with the literature, one structural transition is found

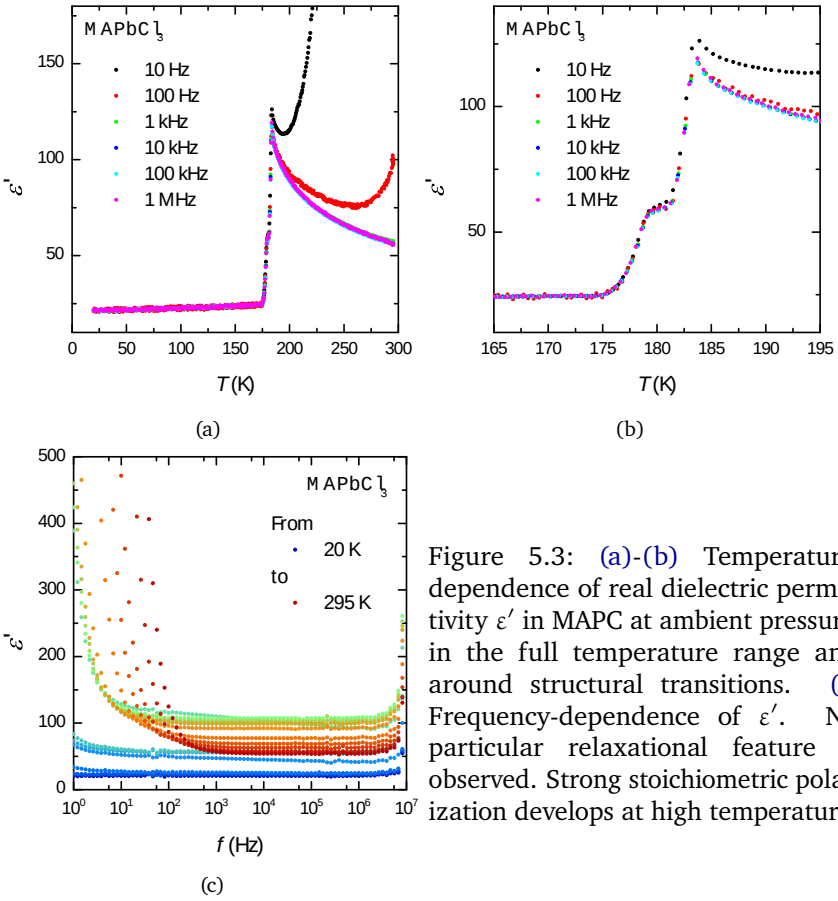

Figure 5.3: (a)-(b) Temperature-dependence of real dielectric permittivity ε' in MAPC at ambient pressure, in the full temperature range and around structural transitions. (c) Frequency-dependence of ε'. No particular relaxational feature is observed. Strong stoichiometric polarization develops at high temperature.

at 163 K (fig. 5.4(b)). No significant frequency dependence is noticed at either low temperatures or around structural transitions (fig. 5.4(c)). At high temperatures, the strong stoichiometric polarization due to ion migration is observed [95].

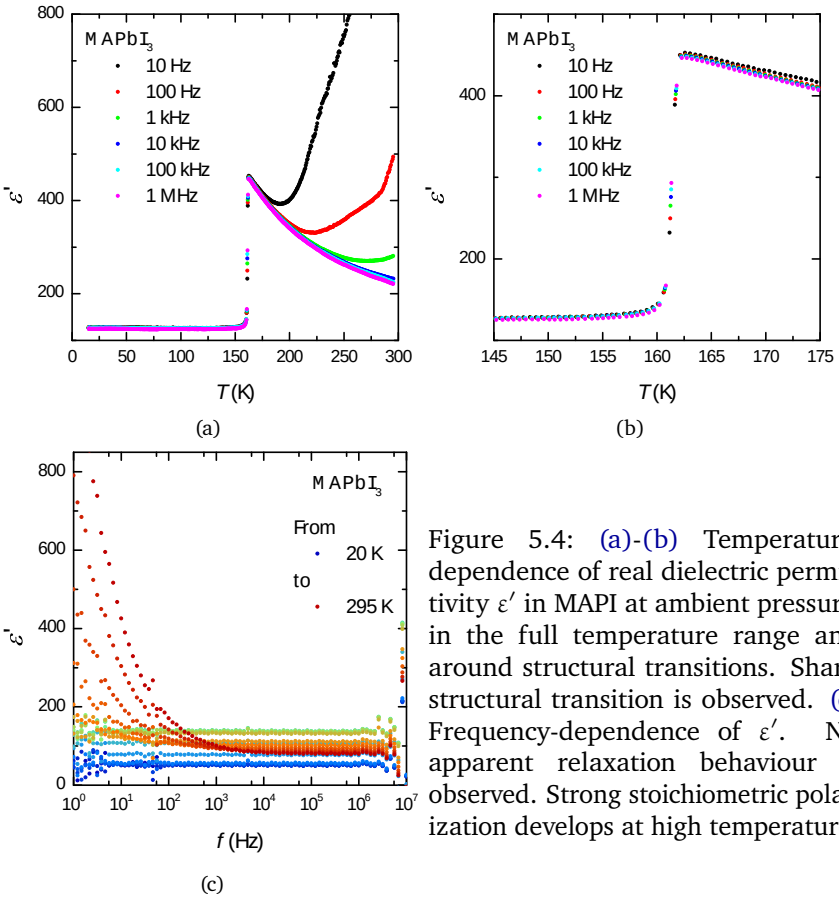

Figure 5.4: (a)-(b) Temperature-dependence of real dielectric permittivity ε' in MAPI at ambient pressure, in the full temperature range and around structural transitions. Sharp structural transition is observed. (c) Frequency-dependence of ε'. No apparent relaxation behaviour is observed. Strong stoichiometric polarization develops at high temperature.

5.2.4 Expectations towards MAPX under pressure

The sharp drop in ε' at an intermediate temperature in every halide is certified to be the result of structural transitions; therefore, the evolution of structures should be easily traced via dielectric measurement under pressure. It is expected for the transition temperature to enhance with pressure because the low-temperature phase is more distorted, an orthorhombic phase.

Accompanied by the transition into the distorted structural phase, ionic motion and dipole reorientation are expected to be reduced because of the reduced freedom. Such that the stoichiometric polarization at high temperatures, which is due to ion migration, and the overall polarizability, the magnitude of ε', are supposed to be suppressed by pressure.

Finally, at high pressure, amorphization is repeatedly reported in the literature. With a detailed trace of structural evolution, it is looking forward to discerning the relationship between structure and the nature of the claimed amorphization.

5.3 Dielectric properties of MAPX under pressure

In the following section, full sets of the temperature dependence of the dielectric properties of MAPX under pressure are displayed. Special features in individual halide and collective behaviours among halides are briefly highlighted and discussed here, whereas the focused analysis is summarized and discussed in the later section (sec. 5.4).

5.3.1 $CH_3NH_3PbI_3$ (MAPI)

The full set of the temperature dependence of dielectric parameters of MAPI at several frequencies and multiple pressure are depicted in fig. 5.5. These data were measured by Agilent 4294A precision impedance analyzer. Because of the limited size of sample crystal in DAC and the capability of the analyzer, the noise level of data below 10 kHz or above 100 kHz exceeds the tolerance for analysis.

There is no significant frequency dependence except at high temperatures and around the structural phase transition. The high-temperature frequency dependence features an enhancement in both ε' and ε'' towards the static limit and rapidly decays as temperature drops. There are more than one possible source for these features, such as the ubiquitous electrode polarization (*c.f.* sec. 2.2.1) and the literature suggestion stoichiometric polarization (Ref. [95]) due to ion migration. The distinct difference between the two is the behaviours under pressure, for which the former would retains while the latter might vary. A more detailed and accurate examination of the pressure-dependence of this high-temperature feature is conducted by subsequent re-measurements using the Novocontrol Alpha-A High-Resolution Impedance Analyzer, whose data are exhibited together with the analysis in the later section (sec. 5.4.2).

The conductivity in MAPI is below 0.1 $\mu\Omega$ cm^{-1} at ambient and high temperature and drops hugely when temperature drops or pressure increases. These observations match with the literature that ordinary resistivity measurement is not applicable.

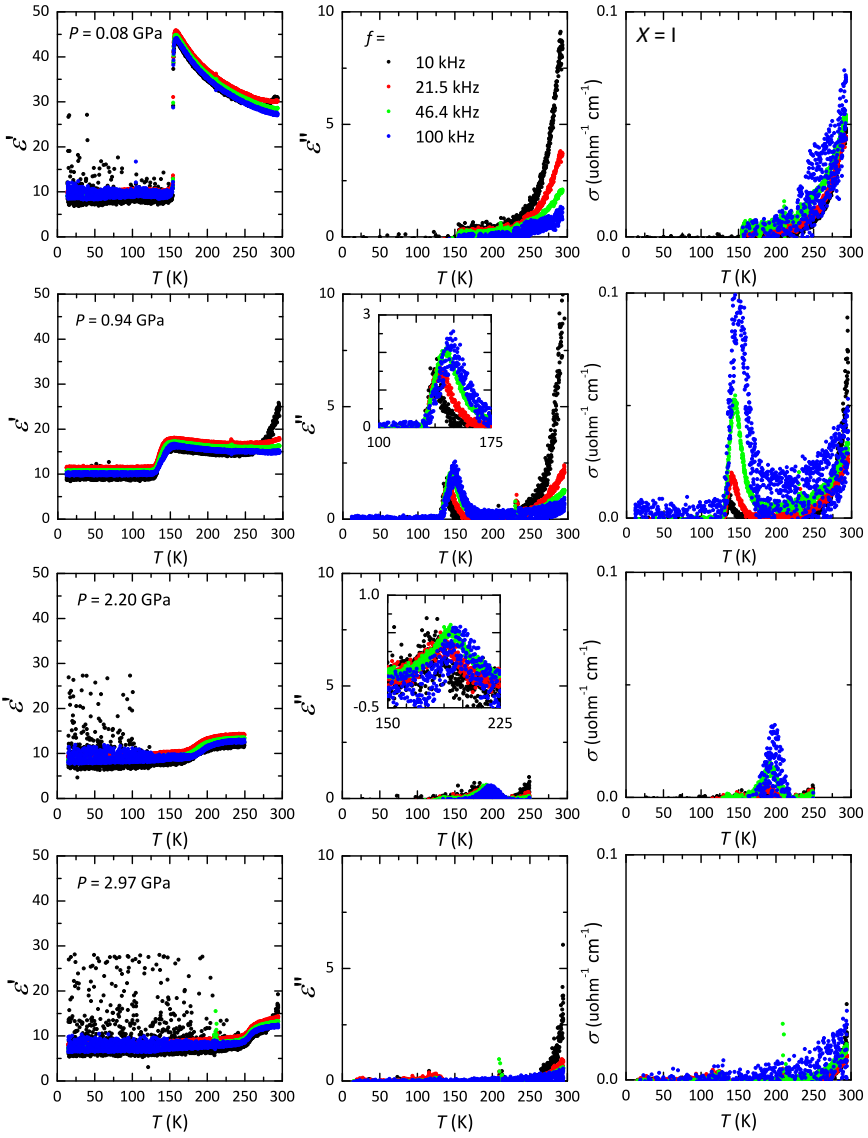

Figure 5.5: Dielectric properties ε', ε'' and σ of MAPI from 10 kHz to 100 kHz at $P =$ (a-c) 0.08, (d-f) 0.94, (g-i) 2.20 and (j-l) 2.97 GPa. Low-temperature phase demonstrates both frequency- and temperature-independence in every property, which can be interpreted as a complete localization of charge carrier and fixation of an electric dipole, and its transition temperature is stabilized by pressure beyond 3 GPa. Read texts for more analysis of the subtle features.

The heights of the paraelectric Curie-Weiss like divergence in ε' at high temperature and the step-like structural transition are gradually suppressed as pressure rises. These indicate a reinforced restriction of the reorientation of MA^+ or ion delocalization. The low-temperature value of ε' is constant throughout all pressure points, which suggests a fully frozen nature of all ions in the low-temperature orthorhombic phase.

Besides the distinct drops in ε', the structural phase transitions are accompanied by the appearance of peaks in ε'' and σ. At low pressure, those features in ε'' and σ would have been heavily masked by the divergence from higher temperature due to ion migration. Therefore, and to be consistent with the former literature, the drops in ε' is elected to be the cursor for locating structural transitions. The discussion on the pressure evolution of the structural phases in MAPI is documented in sec. 5.4.1.

The peaks in ε'' exhibit some shifts at different frequencies. This creates a misleading impression of a relaxor nature of the transition. However, the transitions are authenticated rigorously by literature to be a structural phase transition and so it is frequency independent. Indeed, the low-temperature sides of all peaks from different frequencies coincide at the same temperature, which is the frequency-independence structural transition point. The shifting of high temperature sides of those peaks is the result of superposition with a relaxation, presumably a dipole reorientation, which has a relaxation time of the order of ns at room temperature [108].

5.3.2 $CH_3NH_3PbBr_3$ (MAPB)

Fig. 5.6 displays the full set of the temperature dependence of dielectric parameters of MAPB from 10 kHz to 1 MHz and from ambient to 2.7 GPa. MAPB shares a handful of behaviours with MAPI when being subjected to pressure. The shared features are: suppression of paraelectric Curie-Weiss like divergence in ε', enhancement of structural transition temperature, absence of frequency-dependence, suppression of high-temperature static ε' and ε'', the significant reduction in conductivity, and overlaid relaxation on transition.

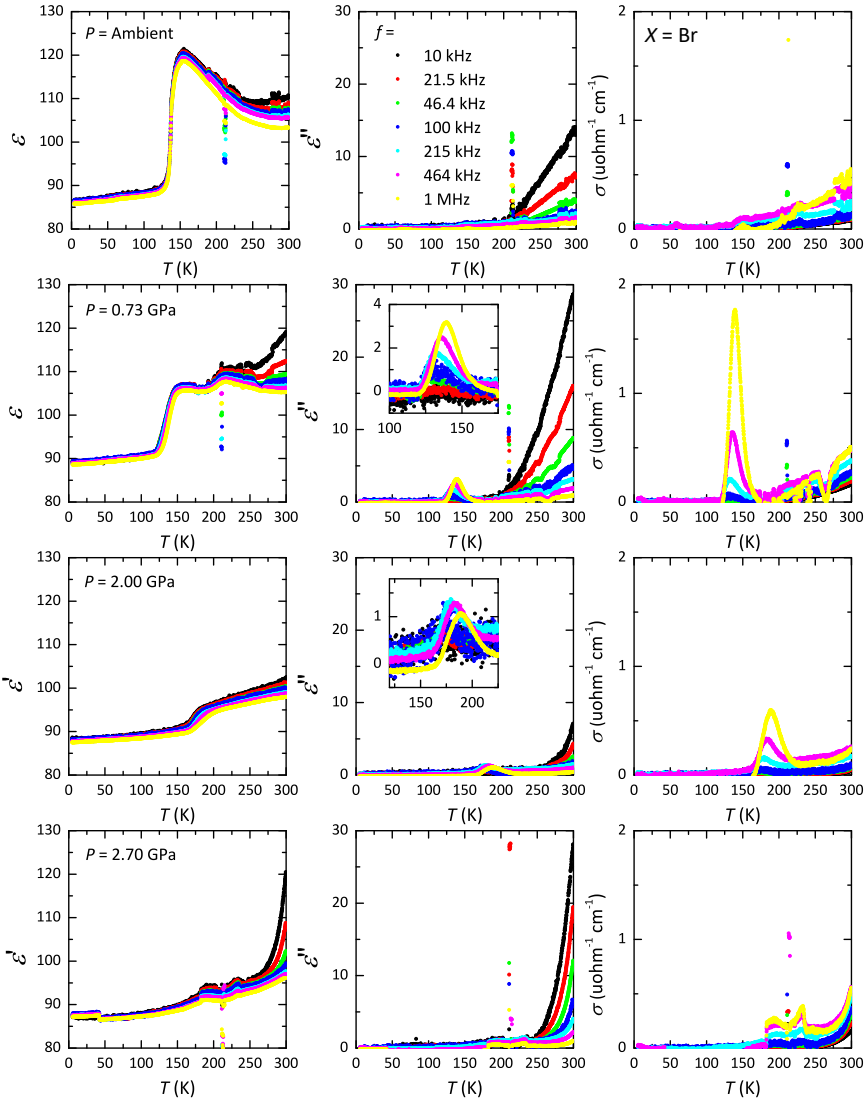

Figure 5.6: Dielectric properties ε', ε'' and σ of MAPB from 10 kHz to 1 MHz at P = (a-c) 0.00, (d-f) 0.73, (g-i) 2.00 and (j-l) 2.70 GPa. Similar to MAPI, the low-temperature phase, which demonstrates no apparent temperature- or frequency-dependence, is gradually stabilized by pressure to room temperature. The distinct discrepancy from MAPI is the addition of cubic-to-tetragonal transition, which is stabilized at early 1 GPa. The rest of features are mostly in accordance with MAPI (see the texts).

The noise level of data of MAPB is remarkably improved compared to those of MAPI. This discrepancy is due to the condition of the wires connection around the pressurized cavity, which is inconsistent because the cavity is newly wired for every new pressure cell.

MAPB crystallized in cubic phase at room temperature, so two structural transitions occur. The magnitude of ε' reduced after the first cubic-to-tetragonal transition is much less than that after the tetragonal-to-orthorhombic transition. This implies that the polarizable units, presumably mainly MA^+ cation, preserve most of the freedom in the tetragonal phase but lose it entirely in the orthorhombic phase.

5.3.3 $CH_3NH_3PbCl_3$ (MAPC)

Fig. 5.7 is the full set of the temperature dependence of dielectric parameters of MAPB from 10 kHz to 1 MHz and from ambient to 2.0 GPa. MAPC also share the same set of features as between MAPB and MAPI: suppression of paraelectric Curie-Weiss like divergence in ε', enhancement of structural transition temperature, absence of frequency-dependence, suppression of high-temperature static ε' and ε'', a significant reduction in conductivity, and overlaid relaxation on transition. These features are common through the MAPX series.

The noise level in MAPC is similar to that in MAPB. The structural transitions are clearly identified at every pressure point till they are stabilized to room temperature. Both transitions are broadened with pressure rises, especially the tetragonal-to-orthorhombic transition, as its shape becomes shoulder-like at pressures above 1 GPa. The broadening of transition could be an indication of the inhomogeneity of structural phases among the crystal.

In contrast to MAPB, the magnitude of ε' drops more through the cubic-to-tetragonal transition than through the tetragonal-to-orthorhombic transition. This observation suggests that the polarizable units in MAPC are already restricted in the tetragonal phase.

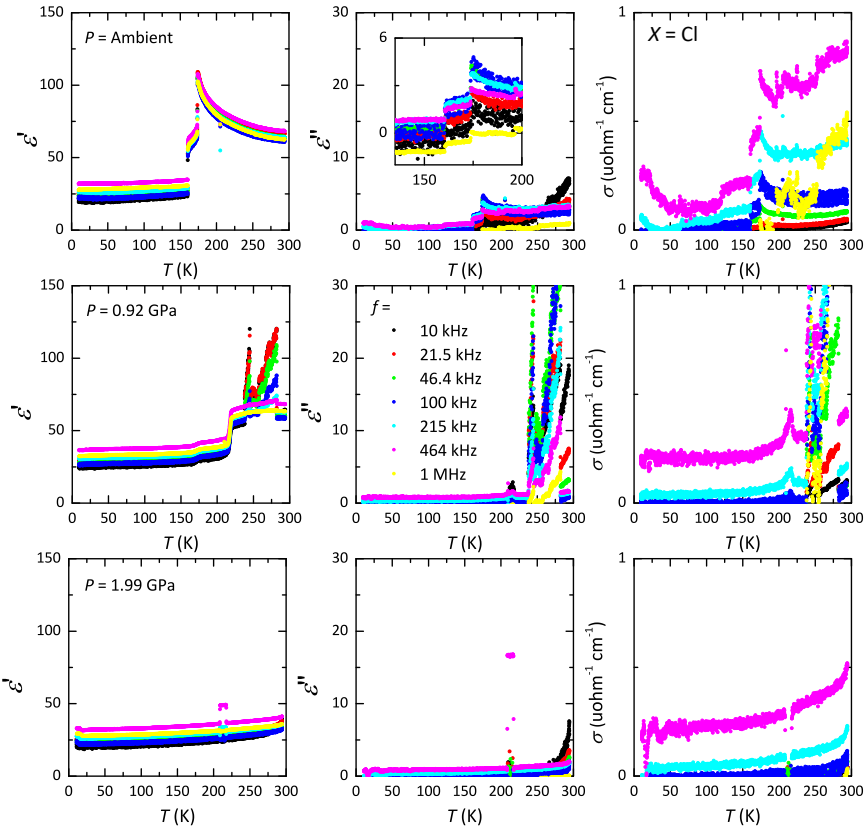

Figure 5.7: Dielectric properties ε', ε'' and σ of MAPC from 10 kHz to 1 MHz at P = (a-c) 0.00, (d-f) 0.92 and (g-i) 1.99 GPa. Most of the behaviours are in accordance with those in MAPI and MAPB. MAPC has the earliest stabilization pressure of structural phases among the three. See texts for the detailed analysis of the subtle features.

5.4 Focused discussions

5.4.1 Structure of MAPX under pressure

Figure 5.8 depicts the temperature-dependence of the real dielectric permittivity ε' of MAPX under pressure. The drops corresponding to the structural transitions are slightly broadened compared to the ambient pressure measurements (*c.f.* sec. 5.2) because of the reduced sample size and reduced signal magnitude. Nonetheless, the transitions remain clearly seen and reliably identified. For all halides, the structural transition temperature is gradually increased and the paraelectric divergence at high temperature is gradually suppressed as applied pressure rises. The pressure evolution of the phase transitions of MAPX, after the incorporation of IR spectroscopy data provided by [147], are summarized and plotted in fig 5.9.

For $X = \mathrm{I}$, there are, in total, three structural phases identified, which are tetragonal $I4/mcm$, orthorhombic $Imm2$ or cubic $Im\bar{3}$ (referred as "intermediate phase"), and orthorhombic $Immm$ phases. The transition from tetragonal $I4/mcm$ into the intermediate phase were only captured below $P = 0.2$ GPa, 3 pressure points, but its linear projection to room temperature matched well with the IR data as it will be stabilized at $P = 0.6$ GPa. The transition from intermediate phase into low temperature orthorhombic phase $T_{\mathrm{O}}^{\mathrm{I}}$ has a rather complex layout in low pressure-regime. It first exhibits a dome-shape with a peak at 180 K at 0.25 GPa, followed by a valley at 160 K at 1 GPa. Beyond that, $T_{\mathrm{O}}^{\mathrm{I}}$ rises monotonically with pressure and is stabilized to room temperature at $P_{\mathrm{I}}^{*} = 3.2$ GPa

For $X = \mathrm{Br}$, four structural phases are identified, which are cubic $Pm\bar{3}m$, cubic $Im\bar{3}$, tetragonal $I4/mcm$, and orthorhombic $Pnma$. The transition into low-temperature orthorhombic $Pnma$ phase $T_{\mathrm{O}}^{\mathrm{Br}}$ shares the similar feature as in I-compound, a dome-shape at low-pressure regime with the peak at 180 K at 0.5 GPa and the valley at 150 K at 0.75 GPa. The orthorhombic phase expands slightly towards low pressure as $T_{\mathrm{O}}^{\mathrm{Br}}$ is stabilized at room temperature at earlier pressure of $P_{\mathrm{Br}}^{*} = 2.6$ GPa. Compared to that of $X = \mathrm{I}$, a cubic $Pm\bar{3}m$ phase emerges from the high temperature and expels the

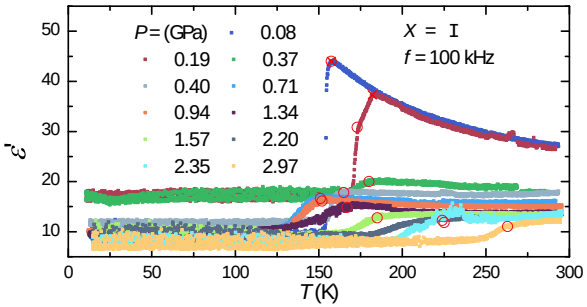

(a)

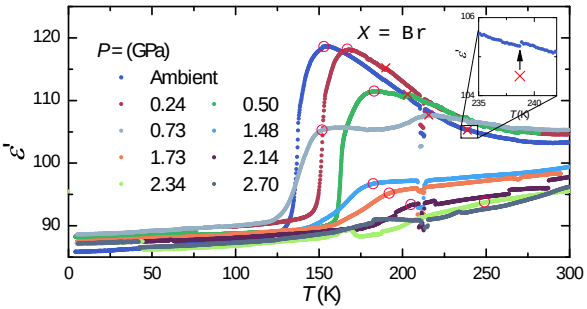

(b)

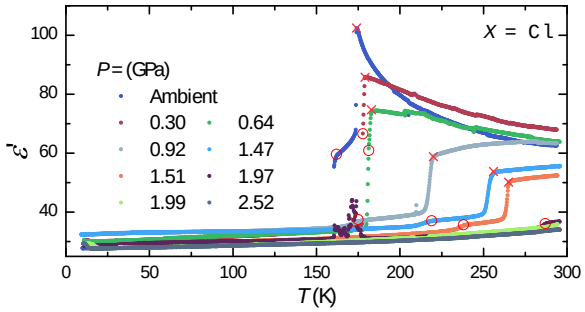

(c)

Figure 5.8: Temperature dependence of ε' of MAPX, $X =$ (a) I ($f = 100$ kHz), (b) Br and (c) Cl, with $f = 1$ MHz at pressures below the stabilization of the low-temperature phase. Identified structural transition is denoted with "×" or "o" symbol, although the transitions behind the same symbol can be different (for details, see the phase diagrams in fig. 5.9).

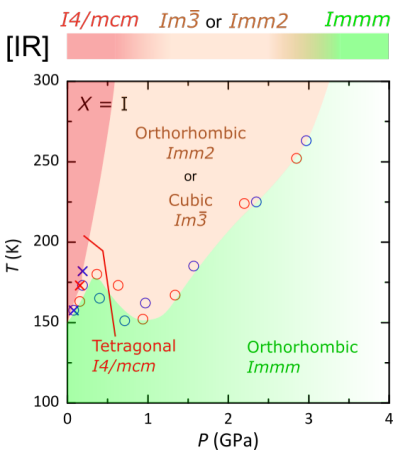

(a)

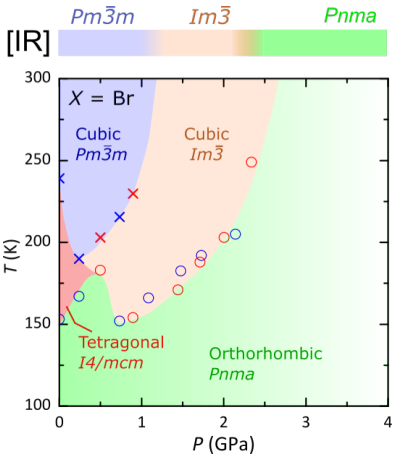

(b)

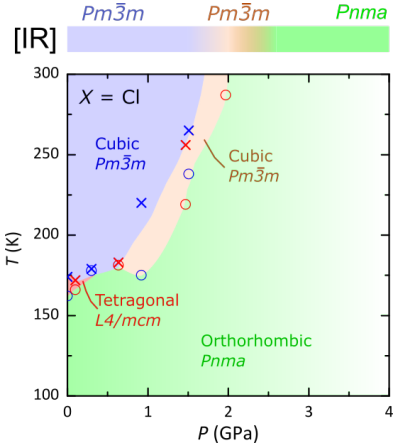

(c)

Figure 5.9: Structural phases diagrams of MAPX with X = (a) I, (b) Br and (c) Cl. Blue and red symbols represent cooling and warming processes, respectively. Structural phases at room temperature determined by infrared measurement from ref. [146], [147] is included for coherent analysis. Structural phases labelled were gathered from the literature as the most probable phases. The high-pressure end is coloured with fading colour to represent the possible amorphous state which is not ruled out by the dielectric study.

tetragonal and cubic $Im\bar{3}$ phase. The transition away from high temperature cubic $Pm\bar{3}m$ phase T_C^{Br} is dropping with pressure at low-pressure regime when transforming into the tetragonal phase. Across the peak of the dome of orthorhombic phase and transition of the intermediate phase from tetragonal $I4/mcm$ to cubic $Im\bar{3}$ phase, T_C^{Br} becomes increasing with pressure and is stabilized to room temperature at 1 GPa.

For $X = \mathrm{Cl}$, there are also four structural phases identified, which are cubic $Pm\bar{3}m$, isostructural cubic $Pm\bar{3}m$, tetragonal $L4/mcm$, and orthorhombic $Pnma$ phases. Following the trend observed from $X = \mathrm{I}$ to Br, the high-temperature cubic $Pm\bar{3}m$ and low-temperature orthorhombic $Pnma$ phases further develop towards each other and squeeze the intermediate tetragonal and isostructural cubic phase. The tetragonal phase is very narrow and seemingly closed at early pressure of 0.4 GPa. The isostructural transition within the two cubic $Pm\bar{3}m$ phases is stabilized at 1.6 GPa. The dome-shape in orthohombic phase persists and the transition T_O^{Cl} is quickly stabilized to room temperature at $P_{Cl}^* = 2$ GPa.

In summary, a trend of enhanced stabilization of low-temperature orthorhombic phase and reinforcement of high temperature cubic phase is observed across the halide series of MAPX from heavier I^- to lighter Cl^- ions. The cubic phase is expanded to a lower temperature and high pressure while the orthorhombic phase transition pressure P^* drops from 3.2 GPa to 2 GPa from $X = \mathrm{I}$ to Cl.

5.4.2 Ion migration in MAPX under pressure

The frequency-dependence of real dielectric permittivity $\varepsilon'(f)$, imaginary dielectric permittivity $\varepsilon''(f)$ and AC conductivity $\sigma(f)$ of MAPX at room-temperature under different pressure are displayed in figures 5.10, 5.13, and 5.11, respectively. A gigantic divergence at low frequency is observed in $\varepsilon'(f)$ in all halides, which has been evidently attributed to the stoichiometric polarization due to substantial ion migration. The percentage growth, *i.e.* $\varepsilon'(f \to 0)/\varepsilon'(f \to \infty)$, is more than 1000% in both $X = \mathrm{I}$ and Cl but and 500% in $X = \mathrm{Br}$, hence qualified as a severe extrinsic polarization. However,

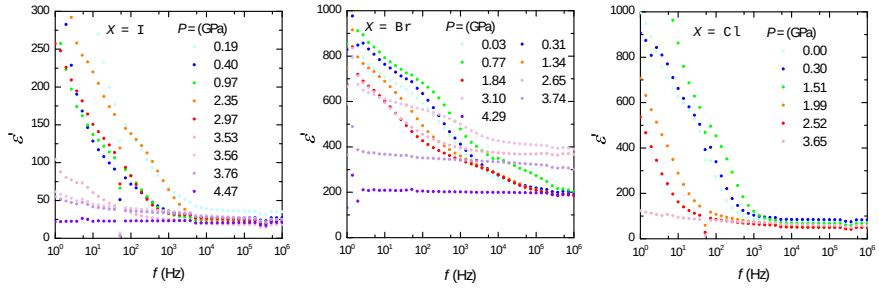

(a) (b) (c)

Figure 5.10: The frequency-dependence of real permittivity ε' of MAPX, $X =$ (a) I, (b) Br and (c) Cl. In all halides, the severe stoichiometric polarization that occurs at ambient pressure is progressively diminished and completely negated at sufficiently high pressure.

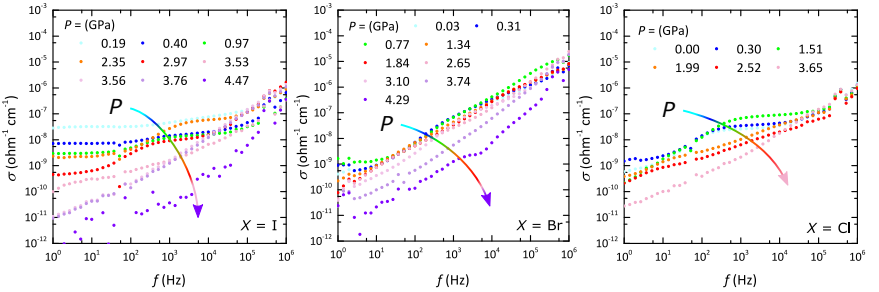

(a) (b) (c)

Figure 5.11: The frequency-dependence of AC conductivity σ of MAPX, $X =$ (a) I, (b) Br and (c) Cl. In all halides, the magnitude of σ is decreasing as pressure rises, and drops below 1 nS cm^{-1} at high pressure, which indicates the reduction of both electronic and ionic conductions.

the magnitude of the growth does not directly reflect the severity of ion migration as it is a cooperative result between the crystal and the artificial conductive electrodes.

No apparent behaviour is seen at high frequencies in $\varepsilon'(f)$ nor $\varepsilon''(f)$ in any halide, *i.e.* no relaxation is taking place at the high frequency domain. In the intermediate frequency range (∼100 Hz to ∼10 kHz), in $X = \mathrm{Br}$ and Cl, a step-like/peak-like feature can be identified on top of the stoichiometric/conduction divergence in the $\varepsilon'(f)/\varepsilon''(f)$ spectrum, which implies the occurrence of a relaxation mode. Concurrently, a distorted peak-like feature can be found in $\sigma(f)$ around the same frequency range. Discussions around this emerged relaxation are documented in the later section (sec. 5.4.3).

The magnitude of $\sigma(f)$ drops by three or more orders after 4 GPa is applied. At ambient pressure, the electronic and ionic conductivities are both estimated to be in the order of 1 nS cm^{-1} [95]. As the total conductivity drops below 1 nS cm^{-1}, this guarantees that both electronic and ionic conductions are significantly suppressed under pressure. The reduction in conduction is simultaneously indicated by the drop in f^{-1} background in $\varepsilon''(f)$ under pressure. Since the drop in σ happens concurrently with the suppression of divergence in ε', the validity of stoichiometric polarization is further solidified.

The low-frequency divergence in $\varepsilon'(f)$ is gradually suppressed by pressure in every halide. The frequency-dependence is completely flattened out at $P_{\mathrm{flat}} = 4.5$, 4.3, 3.8 GPa for $X = \mathrm{I}$, Br, Cl respectively. The degree of stoichiometric polarization is quantified by elementarily accounting the ratio between ε' at low and high frequencies, *i.e.* $R_{\mathrm{im}} = (\varepsilon'_{\mathrm{low}} - \varepsilon'_{\mathrm{high}})/\varepsilon'_{\mathrm{high}}$ (fig. 5.12). Abrupt changes in R_{im} occur across structural phase transitions, which implies the correlation between structures and ion migration. Once the system transformed into the high pressure orthorhombic phase, R_{im} reduces sharply and monotonically and completely disappears at P_{flat}. This full suppression of stoichiometric polarization is a direct indication of the absence of ion migration inside the crystals in the orthorhombic phase. Since P_{flat} is reduced along with the halide series from $X = \mathrm{I}$ to $X = \mathrm{Cl}$, it is reinforced that X^- ion is the major migrating ion and subsequently the major

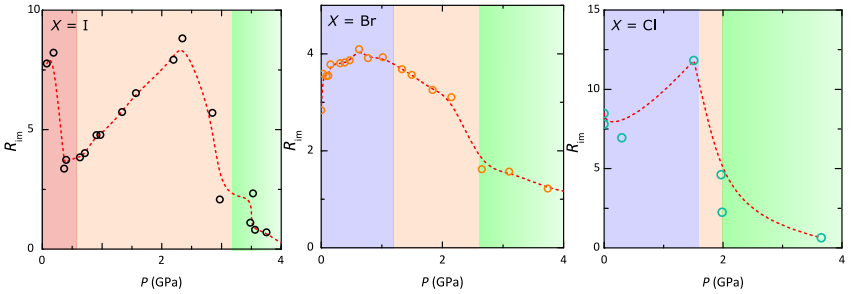

Figure 5.12: The pressure-dependence of the quantified stoichiometric polarization R_{im}, $X =$ (a) I, (b) Br and (c) Cl. The color codes represent the corresponding structural phases as indicated in fig. 5.9. Abrupt changes occur across structural phase transitions, which indicates the relationship between structures and ionic motion. Inside the high pressure orthorhombic phase, R_{im} reduces sharply and approaches zero. It implies that the ion migration is completely suppressed in the orthorhombic phase.

source of the stoichiometric polarization in MAPX.

In summary, the stoichiometric polarization due to ion migration in MAPX is observed to be completely suppressed by pressure. X^- ion is further evidenced to be the major migrating charge carrier because of the trend in P_{flat} along the halide series, where P_{flat} reduces from $X =$ I to Cl. It is thus conceivable that the smaller halide ion, or mimicking the effect of external pressure, would lead to less ion migration, and subsequently higher stability [102].

5.4.3 Disappearence of kHz relaxation in MAPX under pressure

As displayed in fig. 5.13, there is a shoulder feature exhibited by the ε'' around $f = 1$ kHz at a low-pressure range in every halide, which is the signature of a relaxation mode superimposed on the f^{-1} background due to conduction. Similarly, there is a step-like feature superimposed on the stoichiometric polarization in ε' (fig. 5.10) around $f = 1$ kHz, but not as

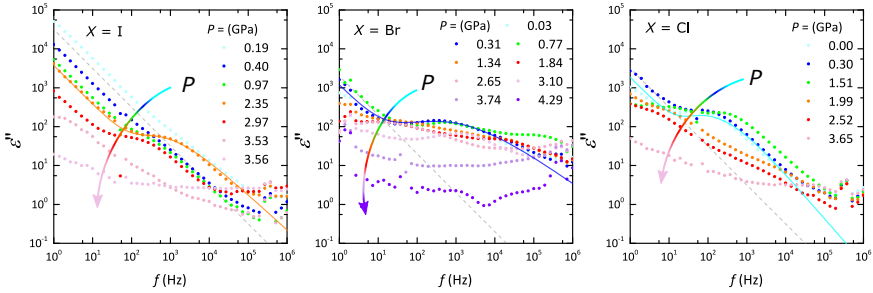

(a) (b) (c)

Figure 5.13: The frequency-dependence of imaginary permittivity ε'' of MAPX, $X =$ (a) I, (b) Br and (c) Cl. In all halides, a relaxation feature occurs at 1 kHz in the intermediate phases and is absent in the high-pressure orthorhombic phase. Because of its slow relaxation time, it is attributed to the translational motion within the cage or hopping motion between cages of the MA^+ cation.

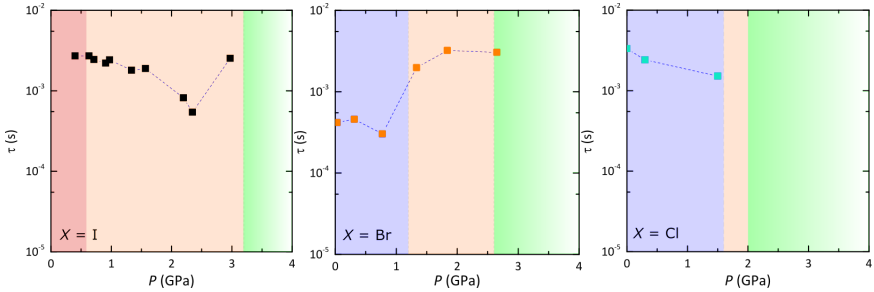

(a) (b) (c)

Figure 5.14: The pressure-dependence of the relaxation time of the anonymous relaxation at kHz in MAPX with $X =$ (a) I, (b) Br and (c) Cl. The color codes represent the corresponding structural phases as indicated in fig. 5.9. The abrupt change in relaxation time is observed across phase transitions. The disappearance of this relaxation mode inside the orthorhombic phase is a sign of complete loss of freedom for the corresponding dipolar unit, which is most likely the MA^+ cation.

noticeable as in ε'' plots. The characteristic response time τ of this relaxation was determined by the Navriliak-Negami equation (eqn. 2.20).

Figure. 5.14 illustrates the pressure-dependence of the relaxation time τ of the relaxation mode in every halide. The relaxation time τ in every halide is not demonstrating any significant pressure-dependence and prominent changes have only happened across a structural phase transition, indicating a close correlation between the relaxation and the lattice structure. On top of that, the relaxation mode is consistently absent once the system enters the orthorhombic phase, meaning the loss of the degree of freedom responsible for this relaxation mode in the orthorhombic phase.

Table. 5.1 listed the motions of MA^+ cation in MAPX reported by literature and the inclusion of the newly noticed mode in kHz. The speeds of motions of MA^+ cations are best benchmarked by the in-cage reorientation of the MA^+ cation, as it is the most researched motion, and its frequency is in the order of GHz. The kHz relaxation ought to be a slower motion than the reorientation of the whole MA^+ cations. It is worth mentioning the possibility that this motion belongs to X^- or Pb^{2+} ions. X^- ion is ruled out because of the equal magnitude of τ among all three halides, where the masses of X^- varies substantially. Pb^{2+} ion is unavoidably possible, but the activation energy for Pb^{2+} delocalization is the highest and it is, in turn, unlikely to maintain a uniform structure if both building blocks of the cage, Pb^{2+} and X^- ions, are not localized. By elimination, this kHz relaxation mode is eligible for translational vibration within or between the inorganic PbX_3^- cages of MA^+ cations. Therefore, by stabilizing the crystal structure of MAPX, or any hybrid perovskite, the migration of MA^+ is expected to be forbidden, which in turn, could provide higher structural stability.

5.4.4 Validity of amorphization

Fig. 5.15 depicts the dielectric properties of MAPX at pressures higher than the stabilization of low-temperature orthorhombic phase P^*, which coincide with the literature amorphization pressure (3, 2.7, 2.4 GPa for X = I, Br

[1] Inferred by ref. [93]

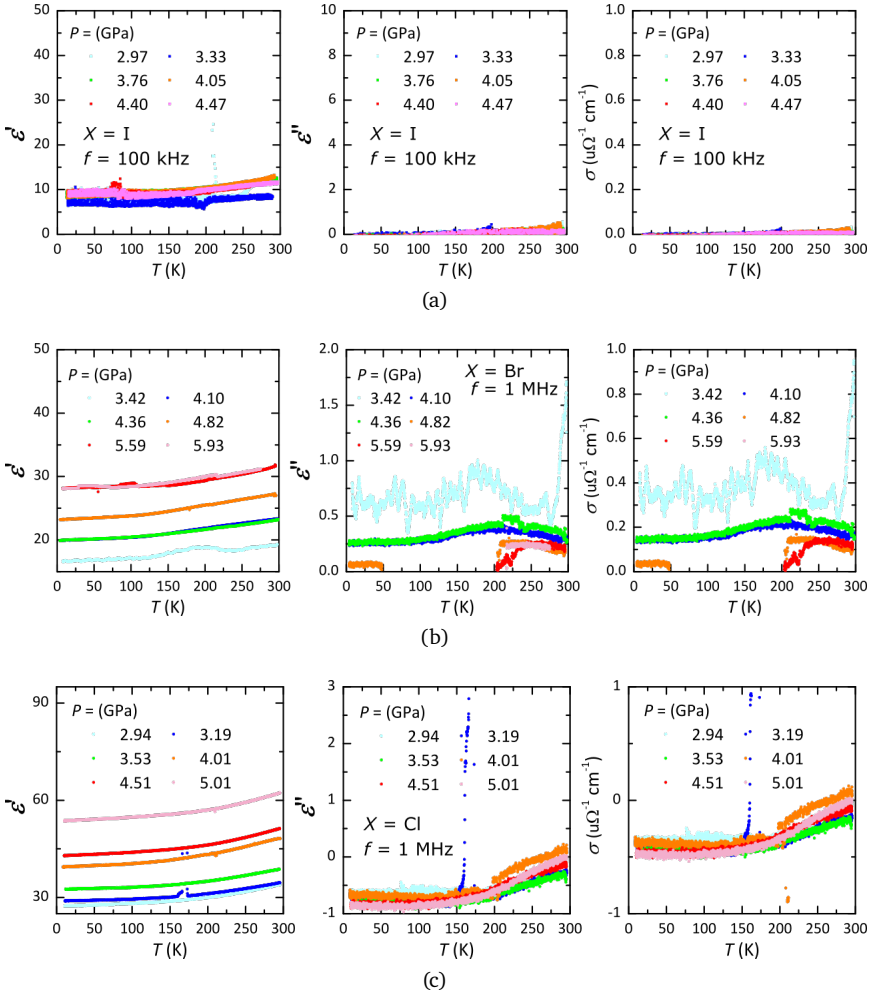

Figure 5.15: The temperature-dependence of dielectric properties at high pressure beyond P^* of MAPX with $X =$ (a) I, (b) Br and (c) Cl. No apparent anomaly, *e.g.* gain in ε' or relaxational behaviour, can be discerned at pressures beyond P^*. The absence of anomalies suggests that the system does not undergo amorphization, which destroys periodic lattices and creates rooms for ionic motion, but an inhomogeneous distortion instead.

Motion	Method	Year	Time	Frequency	Ref.
Vibration modes of MA^+ cation	FTIR	2015	$<$ 30 fs	$>$ 30 THz	[111]
Small amplitude reorientation	2D IR	2015	~300 fs	3.33 THz	[105]
In-cage reorientation	NMR	1985	~200-400 fs	2.5-5 THz	[74]
	mm-wave interferometer	1987	5.37 ps	186 GHz	[112]
	NMR & NQR	1991	0.1 ps	10 THz	[75]
	MD	2013	3.14 ps	318 GHz	[113][1]
	ab initio & IR	2014	4-6 ps	167-250 GHz	[107]
	QENS	2015	14 ps	70 GHz	[93]
	2D IR	2015	3 ps	333 GHz	[105]
(Unidentified)	Dielectric	2017	1 ns	1 GHz	[108]
Translation in/between cage(s)	Dielectric	2021	1 ms	1 kHz	this thesis

Table 5.1: Motions observed experimentally within the MAPX single crystals, with the addition of the kHz motion observed in this thesis.

and Cl respectively). None of the ε', ε'' or σ exhibits noticeable pressure-dependence up to 4.5-6.0 GPa. Same for every halide, ε' demonstrates a smooth and slight increase with temperature, which should be the result of thermal excitation on MA^+ cation. A significant gain in magnitude in ε' happens in X = Br and Cl, but not in X = I till 4.5 GPa. This gain is suggestive of a promoted freedom of MA^+ for polarization and a potential sign for amorphization. The gain appears after 3.5 GPa and 3.2 GPa for X = Br and Cl respectively, about 1.5 GPa above P^*. Such that it could be that the same gain would be exhibited in X = I beyond 4.7 GPa, which is barely missed by the pressure cycle. However, amorphization is not the

only possible source of the gain. The physical modification of electrodes, thus modifying the geometric factor, could lead to a wrong estimation of intensive physical parameters, so a gain in ε' is obtained. Fig. 5.16 contains the photos of the sample cavities of MAPX under low and high pressure. At high pressure, the thickness of the cavity is squeezed and below the thickness and the sample plus electrodes, so the electrodes are compressed and the area is increased and the thickness is reduced. In this case, more polarization will be picked up between the electrodes, so the estimation with the old geometric factor d/A would result in a larger ε'. More details about artificial effects are discussed in the later section (sec. 5.4.5).

Meanwhile, σ does not show any signature which supports the appearance of amorphization. In the earlier section (sec. 5.4.2), it is shown that the ionic migration/conduction is suppressed because of the stabilization of the structure. Amorphization would break free of the restriction and create domain walls and disorders for hopping conduction, so an enhancement in σ is expected when amorphization happens. As depicted in the right column of fig. 5.16, no apparent pressure dependence is exhibited by any halide at high pressure.

Given the coincidence of the literature amorphization pressure (3, 2.7, 2.4 GPa for $X =$ I, Br and Cl respectively) with the stabilization pressure of orthorhombic phase P^* (3.2, 2.6, 2 GPa for $X =$ I, Br and Cl respectively) and the abnormal reversibility, it is plausible that the observed amorphous state is actually, instead of amorphization, the orthorhombic phase with inhomogeneous distortions.

5.4.5 Effect of pressure cycle on MAPX

Drastic enhancement of ε' is seen at high pressure in $X =$ Br and Cl, which is most likely coming from an artificial modulation on the metallic contacts instead of an intrinsic response. Because of the shrinking of the sample cavity under pressure, the metallic contact is possibly forced against the crystal and so its contact area is increased, leading to over-calculated intensive physical properties like ε'. This argument is evidenced by the retained growth in ε'

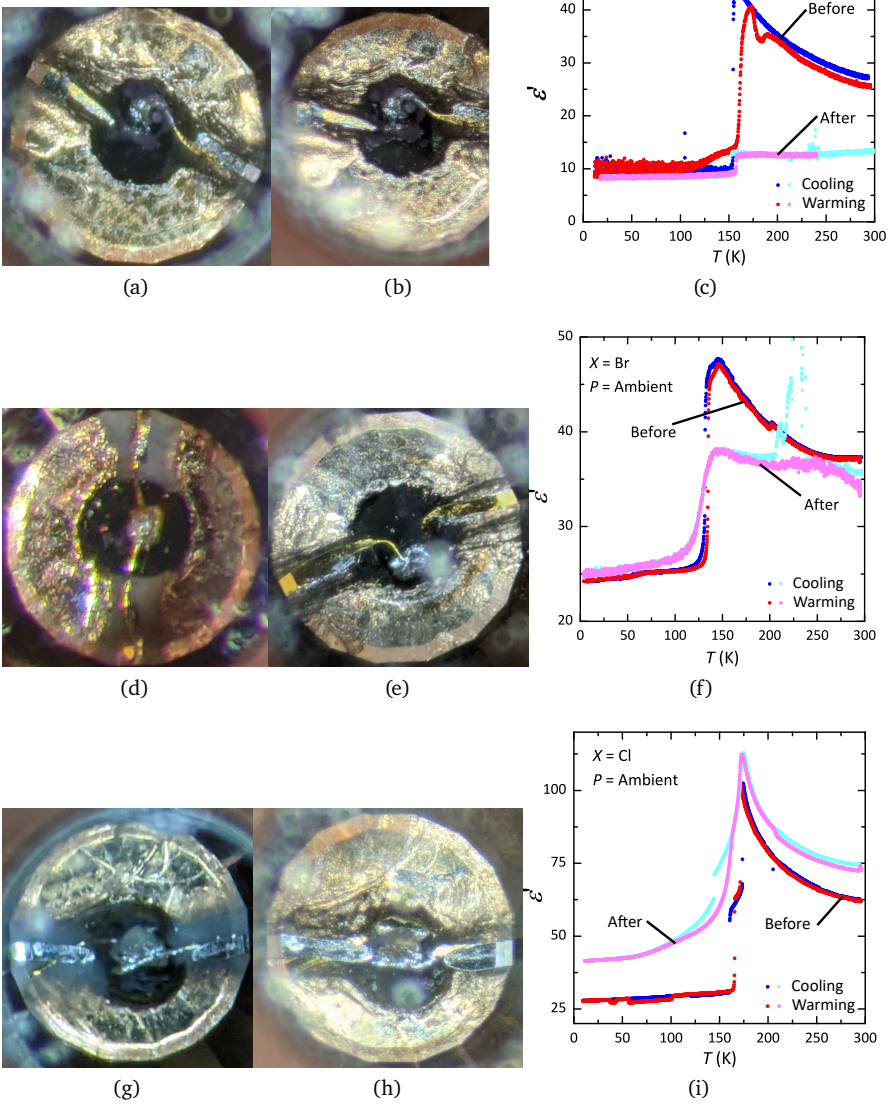

Figure 5.16: Photos of the pressurized cavity before (left) and after (middle) pressurization, and (right) Temperature dependence of ε' at ambient pressure before and after pressure-cycle for MAPX with $X =$ (a)-(c) I, (d)-(f) Br and (g)-(i) Cl.

after depressurization (fig. 5.16).

The pressure cycle has altered the crystal structure, as indicated by the changes in the transition landscape. The transition feature in all three halides has been altered after the pressure cycle in the formats of reduction in amplitude and broadening. These observations can be attempted to explain using the inhomogeneous distortions picture. Upon pressure release, no perfect recovery is undergone because the backward transition pressure is also diverse among the crystal. It results in an irregularly arranged lattice compared to the original as-growth condition. Diverse unit cells are thus created instead of uniform cubic or tetragonal units, which leads to the broadening of transition due to the diverse environment of the atomic sites and reduction of ε' due to reduced symmetry. This idea is supported by the trend from $X = \mathrm{I}$ to Cl, in which the alternation grows from Cl to I (fig. 5.16). This trend aligns with the width of the intermediate phase before the orthorhombic phase of each halide (fig. 5.9). The intermediate phase is where inhomogeneous transitions happen, *i.e.* the period for distortion creation, so the thinnest phase in Cl causes the least distortion among the crystal and thus provides the best recoverability after the pressure cycle.

5.5 Conclusion

The dielectric properties of $CH_3NH_3PbX_3$ ($X = \mathrm{I}$, Br, Cl) under physical pressure have been systematically probed up to 5 GPa. The pressure evolutions of crystal structure, ions motion and migration are determined.

The complete structural phase diagrams of all halides are resolved. For each halide, a complex diagram is exhibited in the low-pressure regime (below 1 GPa) as structural transitions emerge, vanish and evolve non-monotonically in this region. Beyond that pressure range, a stabilization of low-temperature orthorhombic phase to room temperature is exhibited consistently by all halides. The stabilization pressure P^* is 3.2, 2.6 and 2 GPa for $X = \mathrm{I}$, Br and Cl, respectively.

The significant ion migration can be fully negated by high pressure of 4 GPa.

A gradual suppression of the DC divergence of real dielectric permittivity ε' is observed as pressure rises. The DC divergence in ε' is identified by literature as the result of stoichiometric polarization; thus its disappearance indicates the suppression of ion migration. The divergence is fully flattened at $P = 4.47$, 4.29 and 3.65 GPa for $X =$ I, Br and Cl respectively.

A new relaxation at range of kHz is discovered among the $CH_3NH_3PbX_3$ series. The pressure evolution of this relaxation mode is traced, and this mode experiences little or no shift in relaxation time in the cubic or tetragonal phase but suddenly disappears upon transition into the orthorhombic phase in every halide. Through comparison with every relaxation recorded by literature, it is suggested that this kHz relaxation is the translational motion within or hopping motion between the inorganic cages of the organic MA^+. The disappearance in the orthorhombic phase implies the loss of freedom of the MA^+, namely the localization of the organic cation.

The nature of the amorphization is evidenced to be a heterogeneous structural distortion. The pressure ceiling in this study reaches beyond the amorphization pressure endorsed by previous studies. Following the increase of physical pressure, no abrupt transition in dielectric properties is observed. Instead, it is noticed that the structural transition feature is gradually broadened, indicating an inhomogeneous transition among the crystals. Considering the bizarre reversibility of the claimed amorphization and the observed heterogeneity in the crystals under pressure, it is rather more plausible that the amorhization is, in fact, a pressure-induced structural distortion due to the inhomogeneous transitions on the crystals.

Chapter 6

Confined water

6.1 Sample preparations

The beryl crystals were provided by the Prof. Boris Gorshunov's group from The Moscow Institute of Physics and Technology. Besides H_2O-containing beryl, deuterated beryl, namely D_2O-containing, was also synthesized. Figure 6.1 depicts the photos of the beryl crystals used in this study. Hereafter, the normal and deuterated beryl are named beryl-H and beryl-D for simplicity.

Some infrared characterizations on the crystals were done by the Prof. Boris Gorshunov's group before sending us the crystals. The polar impurity will be bounded with the water molecule and shifts the water dipole's vibration mode. The relative concentration of impurity can thus be estimated from the transmission spectrum. Figures 6.1(c) and 6.1(d) show the transmission contour on beryl-H and beryl-D crystals. A concentration gradient is clearly observed in the beryl-D sample and the impurity concentration is almost zero at the edge. Impurity is hypothesized to be one of the hindrances for the electric ordering, so this batch of the crystal provides an ideal condition for further investigation.

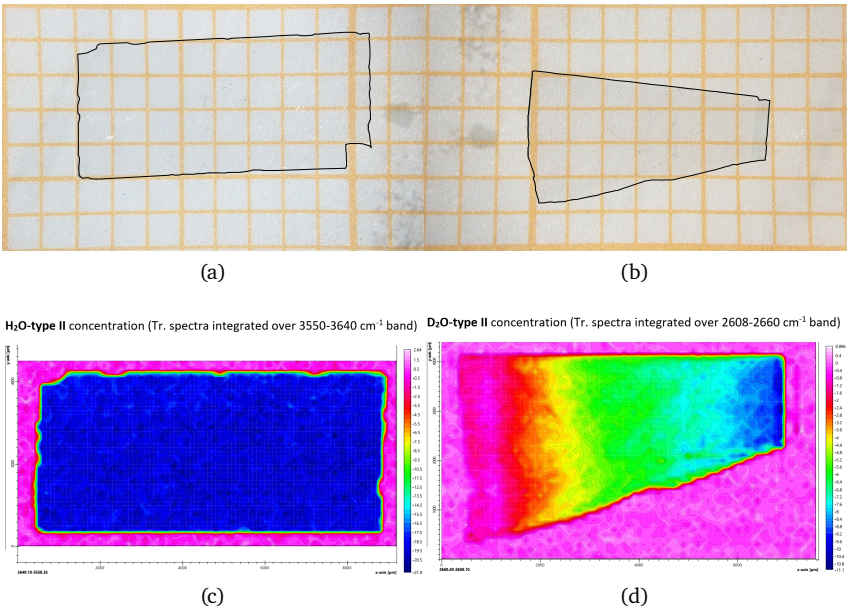

Figure 6.1: Above: Photos of (a) H_2O- and (a) D_2O-containing Beryl crystals obtained from Prof. Boris Gorshunov's group from The Moscow Institute of Physics and Technology. A black line is drawn to frame the shape of crystals as their colour is almost transparent and difficult to see. Below: Contour plots of the integrated Infrared spectra of type-II water vibration mode for (c) beryl-H (3550-3640 cm^{-1}) and (d) beryl-D (2608-2660 cm^{-1}). The higher transmission, the less water-II content.

6.2 Ambient pressure

The properties of ambient pressure beryl-H have been comprehensively studied in the literature. In this study, the ambient pressure measurements aim to clarify the effect of the substitution of D_2O and type-II water molecule concentration.

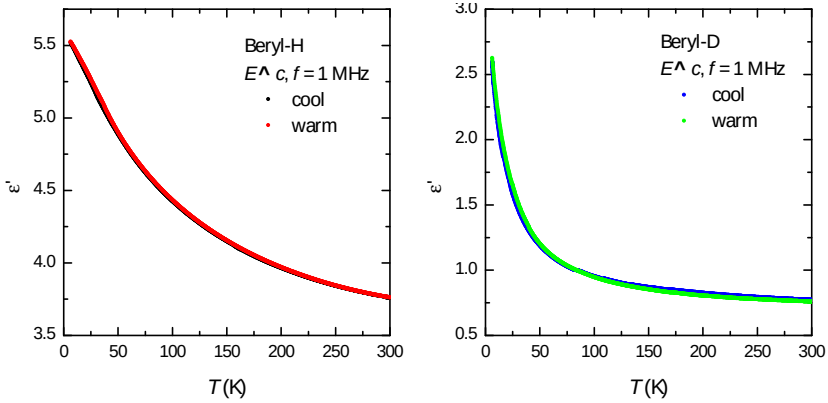

(a) (b)

Figure 6.2: Temperature-dependence of ε' at $f = 1$ MHz and $E \perp c$ upon cooling and warming of (a) beryl-H and (b) beryl-D.

6.2.1 Hysteresis

Figure 6.2 displays the temperature dependence of ε' upon cooling and warming of beryl-H and beryl-D. As shown in the plots, there is no apparent hysteresis in either beryl-H or beryl-D. hysteresis is the shift in critical temperature of first-order phase transition upon cooling/warming processes, so its absence indicates no such transition. Quantum paraelectricity in beryl is either a second-order transition or not a generic phase.

6.2.2 Effect of D_2O substitution

Substitution of D_2O ideally could enhance the phonon-softening and promote the ferroelectric ordering (as aforementioned in ch. 3). Both beryl-H and beryl-D are measured at ambient pressure down to very low temperature, and the results are shown in fig. 6.3. The absolute magnitude shown in fig. 6.3(a) is subjected to the error in geometric factor determination, so the higher magnitude of ε' in beryl-H than in beryl-D is probably not

	CW		Barrett		
	T_c (K)	C	T_c (K)	C	T_1 (K)
beryl-H	-208.259	809.968	-125.645	382.479	20.508
beryl-D	-11.285	34.222	-11.285	34.222	-4.92E-4

Table 6.1: Curie-Weiss (eqn. 2.27) and Barrett (eqn. 2.28) equations fitting parameters for beryl-H and beryl-D.

genuine. Nonetheless, the effect of quantum paraelectricity/ ferroelectric can be examined by the percentage growth in ε'. As shown in fig. 6.3(b), beryl-D exhibits a much stronger Curie-Weiss divergence at low temperature than beryl-H. This observation suggests that the paraelectric divergence is substantially greater in D_2O substituted beryl than in the H_2O counterpart. Evidently, the substitution of D_2O phenomenologically also promotes the formation of electric ordering.

Figure 6.3(c)&(d) show the fitting results of beryl-H and beryl-D at ambient pressure with the Curie-Weiss equation (eqn. 2.27) and Barrett equation (eqn. 2.28). Barrett's equation is a modification from Curie-Weiss with the inclusion of a quantum effect T_1 which prohibit the full ferroelectric transition. Instead of a transition, a plateau will be observed at the base temperature in the temperature-dependence of ε' if a quantum effect presents. As seen from the fits, the quantum effect is absent after substitution of D_2O as T_1 is practically zero where $T_1 \sim 20$ K which aligns with the previous literature [14]. The detailed fitting values are documented in tbl. 6.1. This observation validates the idea that the quantum effect can be effectively suppressed by substituting H_2O with D_2O.

6.2.3 Effect of type-II water concentration

There are two kinds of orientations for D_2O (same as for H_2O) molecule inside the cages of Beryl: perpendicular (type-I) and parallel (type-II) to the c-axis [14], and type-II water molecules (hereafter shortened as "water-II") are suggested to be prohibiting the formation of ferroelectricity. Since samples with a water-II gradient are successfully fabricated, the effect of

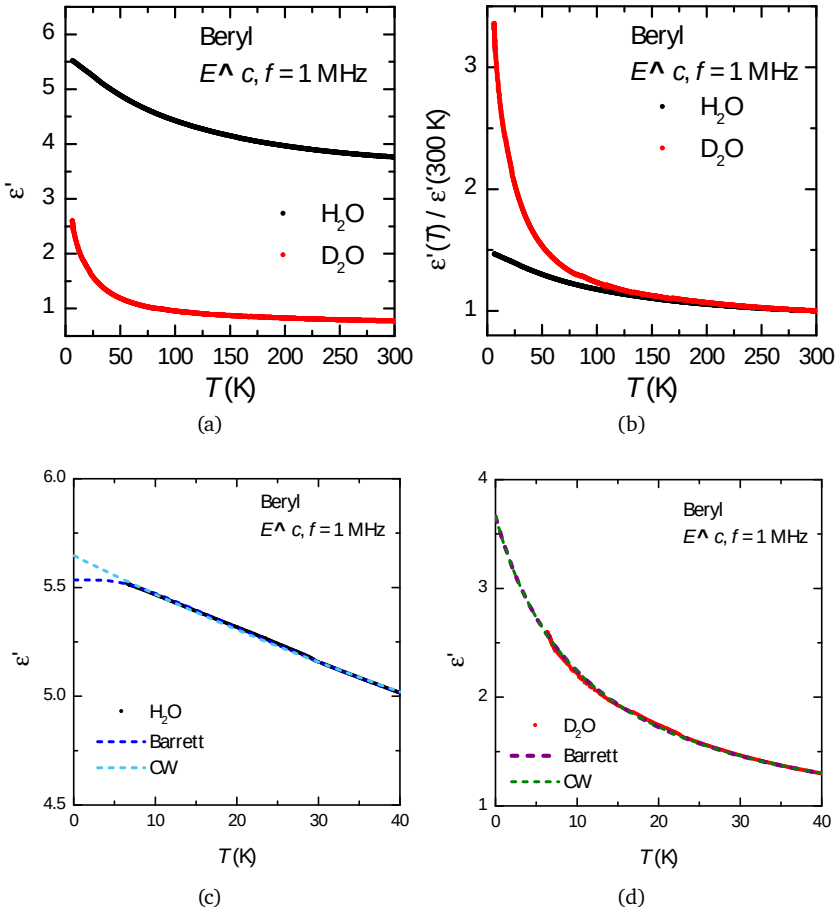

Figure 6.3: Temperature-dependence of ε' of D_2O and H_2O with $E \perp c$ at 1 MHz. (a) absolute value from raw data. (b) normalized by room temperature ε', to illustrate the percentage growth at low temperature. Zoom-in of (c) beryl-H and (d) beryl-D at low temperature with CW and Barrett fittings.

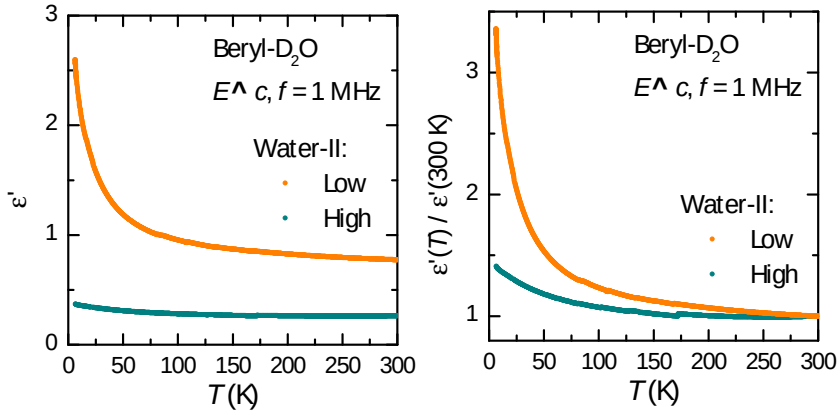

(a) (b)

Figure 6.4: (a) Temperature-dependence of ε' of beryl-D at $f = 1$ MHz and $E \perp c$ with different water-II concentrations. The absolute value of ϵ' is subject to the error in the estimation of the geometric factor. (b) Normalized ε'.

water-II concentration is thereby studied.

Figure 6.3(b) plotted the normalized $\varepsilon'(T)$ of beryl-D with high and low water-II concentrations. The paraelectric divergence developed at low temperature is improved significantly, about 2.2 times, in the low water-II concentration sample, verifying that water-II is involved in the prevention of electric ordering.

6.3 Effect of physical pressure

The application of physical pressure aims to force the water dipoles closer and thus enhance the electric-electric dipole interaction. No chemical impurity or defect is introduced along with the pressurization, but the deformation of cavity geometry and electrodes does induce extrinsic background. After the subtraction of the extrinsic effect, analysis for the evolution of quantum

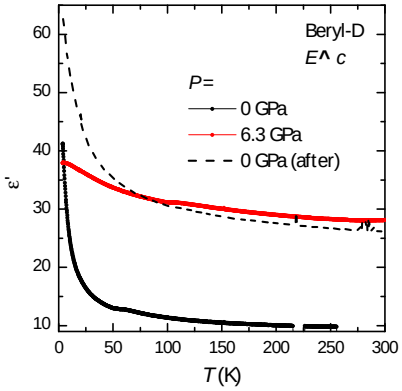

Figure 6.5: Temperature-dependence of ε' of beryl-D at ambient pressure (black), high pressure (red) and after pressure cycle (black dashed line). The gain in magnitude retains after pressure is released, indicating that the gain is an extrinsic artefact.

effect on water dipoles in beryl is conducted.

6.3.1 Extrinsic effects

In the beryl-H and beryl-D pressure measurements in this section, a gain in high-temperature permittivity with pressure is found (fig. 6.7(a) and fig. 6.9). This increase in permittivity, i.e. polarization, originated from extrinsic effects, as the magnitude of ε' did not recover, but the gain remains after decompression (dashed lines in fig. 6.5). The extrinsic nature of this growth is proven by the inconsistency between two separately prepared pressure cells of each beryl sample. The source of this effect is believed to be the artificial increase in metallic contact areas, as seen in the photos (fig. 6.6).

Nonetheless, the Curie-Weiss-like divergence at low temperature exhibits reversible pressure dependence, so there are intrinsic pressure effects on the electric ordering in the water-containing beryl systems.

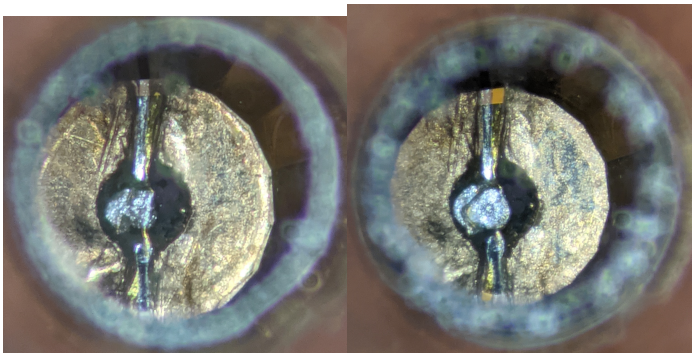

(a) (b)

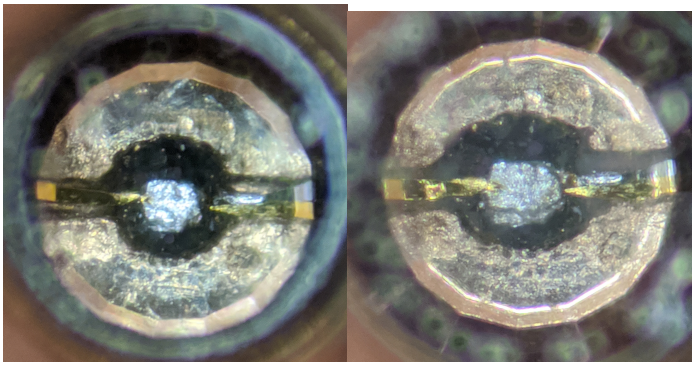

(c) (d)

Figure 6.6: Photos of the sample cavity of before and after pressurization of (a),(b) beryl-H and (c),(d) beryl-D.

6.3.2 H_2O-beryl

Figure. 6.7(a) depicts the temperature-dependence of ε' at 100 kHz under various pressure. The gain in magnitude with pressure is believed to be an extrinsic effect due to the metallic contact expansion (*c.f.* sec. 6.3.1). The divergence developed at low temperature exhibits no pressure dependence. The invariant under pressure is explicitly displayed by shifting the high-pressure curve to stack with the low-pressure data (fig. 6.7(b)).

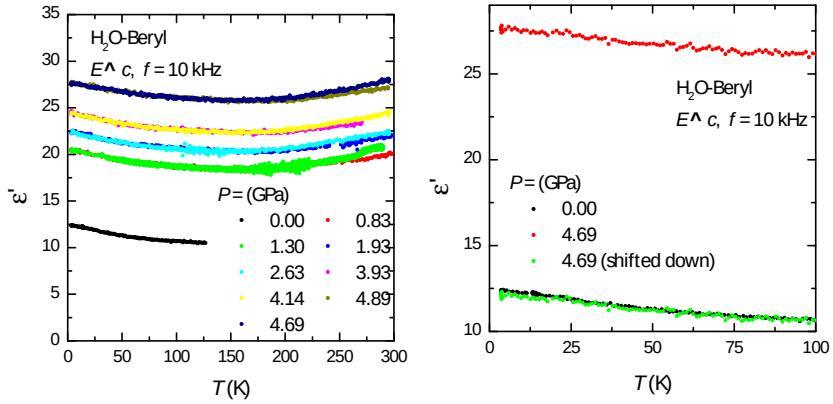

(a) (b)

Figure 6.7: (a) Temperature-dependence of ε' of beryl-H at $f = 10$ kHz with $E \perp c$. (b) Shifted high pressure (4.69 GPa) curve to low pressure (0.00 GPa). The growth at low temperature behave the same at different pressures.

Figs. 6.8(a)-(b) display the fittings and the fitting parameters of beryl-H at low and high pressure. The noise-to-signal ratio in the data is unfortunately quite high, so no precise fitting is obtained, even at ambient pressure. The curves plotted are the best-fitted results, but a wide range of variation in the parameters could also provide a converged fit. The imprecision is illustrated in the pressure dependence of the fitting parameters (figs. 6.8(c)-(d)). Critical temperature T_c from both CW and Barrett equation fittings fluctuates hugely. However, regardless of the fitting condition, no positive T_c is possible, so the data quality is nonetheless good enough to conclude no ferroelectric transition is possibly realised up to 5 GPa. The quantum effect temperature T_1 similarly exhibits huge fluctuation between 0 K - 50 K. No extra information is given except that it remains consistent with the ambient value of 20 K reported by literature [14].

Regardless of the unavailability of precise quantitative fitting, the pressure measurement data indicate firmly an invariant of quantum effect on and general temperature-dependence of water dipole ordering under physical

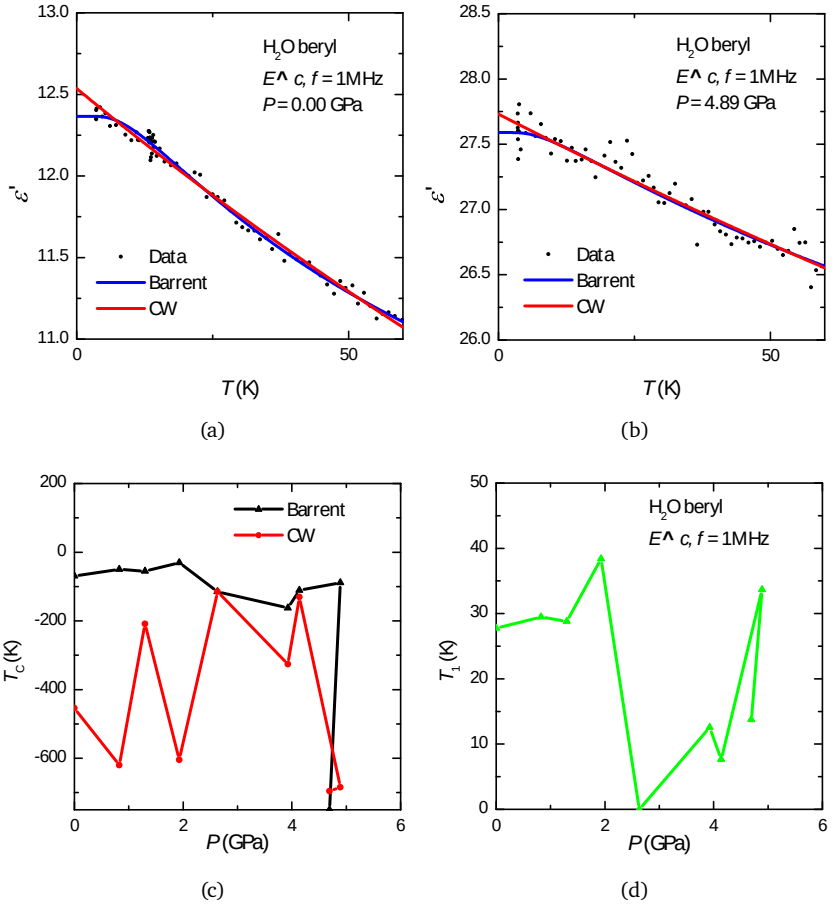

Figure 6.8: Fitting of both CW and Barrett equations at $P =$ (a) 0.00 GPa and (b) 4.89 GPa. The noise-to-signal ratio is unfortunately quite high, so the fitting results are not precise. Illustrated curves are the converged best results. (c) Critical temperature and (d) quantum effect T_1 temperature versus pressure. The critical temperature fluctuates hugely because of the high noise level. Similarly, T_1 fluctuates within 0 K-40 K. The fluctuation is around 20 K which is consistent with the literature value.

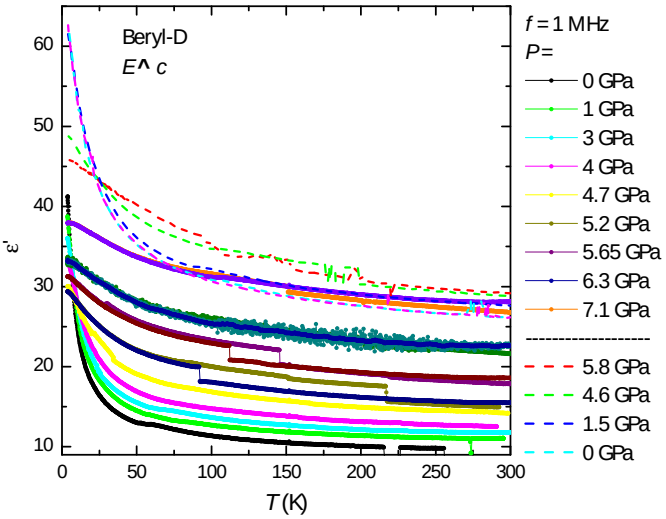

Figure 6.9: Full temperature dependence of ε' of beryl-D with low water-II content upto 7.1 GPa.

pressure up to 5 GPa.

6.3.3 D_2O-beryl

The full $\varepsilon'(T)$ of low water-II beryl-D at all pressure is depicted in fig. 6.9. As pressure rises, the high-temperature permittivity rises steadily. This increase in permittivity, i.e. polarization, presumably originated from extrinsic effects, for example, the increase in metallic contact areas (*c.f.* sec. 6.3.1). Nonetheless, the low-temperature Curie-Weiss-like divergence feature is robust and prominent. This divergence is gradually suppressed by pressure as pressure builds up. At $P = 5$ GPa, a plateau starts to be observed at the base temperature of about 4 K. Application of physical pressure is, in reverse to the expectation, jeopardizing the electric ordering in water-confining beryl.

Fig. 6.10 plotted the fittings results of the Curie-Weiss equation (eqn. 2.27) and Barrett equation (eqn. 2.28) at 0 GPa, 3 GPa and 6.2 GPa. From here, the deviation of the data from the Curie-Weiss law is clearly examined.

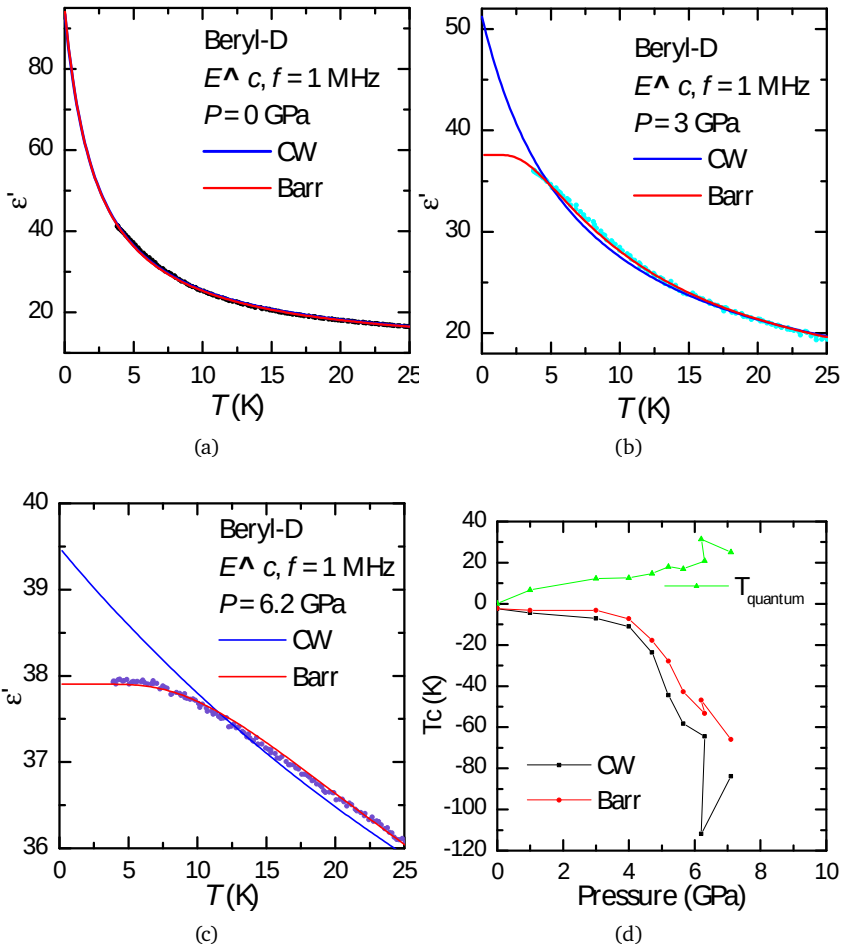

Figure 6.10: Real permittivity $\varepsilon(T)$ of beryl-D at (a) 0 GPa, (b) 3 GPa and (c) 6.2 GPa. The deviation between Curie-Weiss and Barretts equations develops earlier at higher pressure. (d) $T-P$ plot of the critical temperature from Curie-Weiss and Barrett equations and the range of quantum effect T_1. T_1 emerges upon application of pressure and reaches 20 K, as the estimated value for beryl-H in the literature [14], at 6 GPa.

At ambient pressure, there is no discernible deviation down to the base temperature of 4.5 K. The signature plateau of Barrett behaviour is gradually developed along with pressure application. The evolution of the characteristic temperature T_1 for the quantum effect is plotted in fig. 6.10(d), together with the evolution of T_c from both equations. T_1 grows gradually with pressure and reaches 20 K, the value estimation for beryl-H [14], at 6 GPa. The application of physical pressure is, in contrast of expectation, evoking the quantum effect, which prohibits ferroelectricity.

6.3.4 Refined D_2O-beryl

The D_2O-beryl data set processes a high signal-to-noise ratio and a fine step-size in pressure, so it is worth reinforcing the analysis to grasp further insights. In this section, the data set is refined by eliminating extrinsic contributions and imposing constraints on parameters based on the theoretical understanding. A deeper interpretation is obtained.

Figure. 6.11 depicts the refined beryl-D data. Beryl nature crystal is rigid and is not susceptible to compression. As reported by a XRD study [94], at the highest pressure reached in our measurement (7.1 GPa), the volume of beryl unit cell shrinks merely 4%. Therefore, no dramatic change shall be induced, especially at high temperature, and the absolute magnitude of ε'_∞ is kept constant ($= 7.3$) and the data curves are shifted correspondingly. After that, it is considered that at high temperatures, the system follows Curie-Weiss behaviour due to reduction of thermal fluctuation. The Curie-Weiss constant C (*c.f.* eqn. 2.27) is solely depending on the density of dipoles. Similarly, neither the size of nano-channel nor the number of water molecules are changed much under 7.1 GPa, C is not expected to vary through the data set, so the data curves are scaled to have a matching C ($= 415$) at high temperatures. The matching of C can be seen more explicitly in the $(\varepsilon' - \varepsilon'_\infty)^{-1}$ plot (inset of fig. 6.11), in which Curie-Weiss behaviour becomes straight lines with a slope equals C. The characteristic plateau at low temperature is unaltered and fitted again for quantitative analysis.

Figure. 6.12 shows the pressure-dependence of the Barrett (eqn. 2.28)

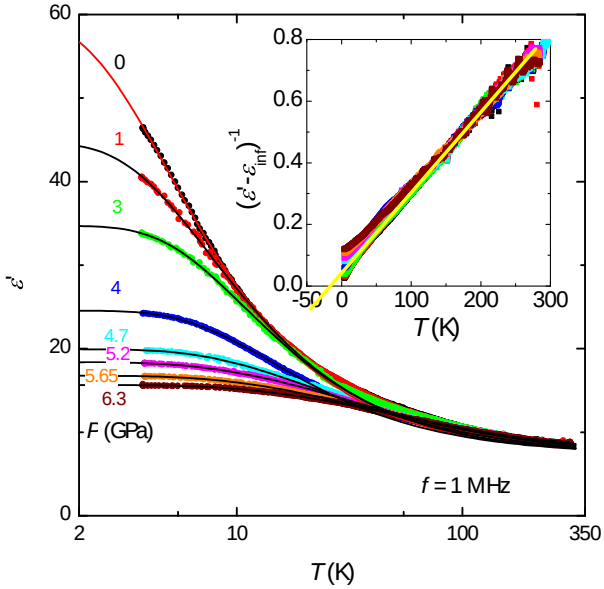

Figure 6.11: Refined ε' of beryl-D. The high temperature ε'_∞ and C are kept constant as the dipole moment and density of D_2O molecular dipoles shall not vary with pressure. Also, some jumps and consistent kink in temperatures are removed as they are most likely experimental artefacts.

and Curie-Weiss (eqn. 2.27) fitting parameters fitted only around the low-temperature plateau. The general behaviours of T_C and T_1 remain the same as before data refinement, *i.e.* both T_C and T_1 grow in magnitude with pressure. In this refined result, it is seemingly that T_1 flattens out above $P = 4.5$ GPa. This observation suggests a loss of pressure-induced change in the water dipole localization potential beyond 4 GPa, which we suggest to be the disappearance of the six-fold potential barrier. T_C and C also exhibit a distinct change above $P = 4.5$ GPa, as both start to rise in magnitude afterwards. The increase in T_C can be explained as the enhancement of dipole-dipole interaction due to reduced dipoles separation and induced anisotropy as c-axis shrunk faster. However, C, as mentioned earlier, was not expected to vary because the concentration of water content is invariant.

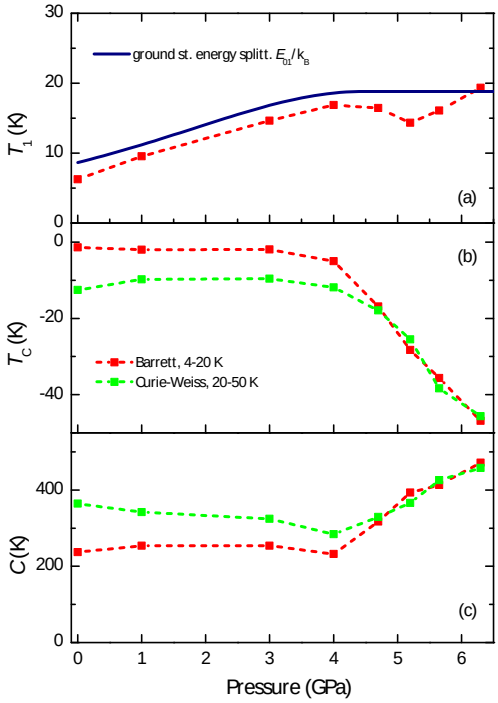

Figure 6.12: Pressure evolution of (a) quantum temperature T_1, (b) critical temperature T_c, and (c) Curie-Weiss constant C obtained from fitting of Curie-Weiss (eqn. 2.27) and Barrett equation (eqn. 2.28) on refined ε' around the low-temperature plateau. General behaviours of T_1 and T_c are the same as before refinement. Saturation of T_1 and increase in T_c begin at $P = 4.5$ GPa instead. The evolution of T_1 matches with the calculation of the energy difference between the first excited state and ground state E_{01} by Monte Carlo simulation (*c.f.* sec. 6.4). C also exhibits a rise of magnitude beyond 4.5 GPa, which requires further theoretical knowledge for interpretation.

Further or reproduced measurements are needed to address this issue.

6.4 Theoretical interpretation

The quantum temperature T_1 from the Barrett expression (eqn. 2.28) quantifies the tunnelling probability, and it is thus proportional to the energy difference between ground and first excited states E_{01}. It has been assumed in KD_2PO_4 and KH_2PO_4 that the azimuthal potential of dipoles will be suppressed by physical pressure [148]. Following the same assumption, collaborators Dr. Veniamin. A. Abalmasov and Prof. Dr. Boris Gorshunov have calculated the energy levels and azimuthal angle potential experienced by water dipoles in beryl and the results are plotted in fig. 6.13. Also, the calculated values of E_{01} are plotted alongside T_1 in fig. 6.12. The saturated value of T_1 corresponds to $E_{01} = 1.64$ meV, which coincides with the energy of free rotation around the c-axis for D_2O molecule, supporting the idea of the disappearance of the potential barrier as the mechanism behind the saturation of T_1. One concerning issue is the seemingly high estimated $V_0 = 80$ meV. Previously, the amplitude of the potential barrier was estimated by

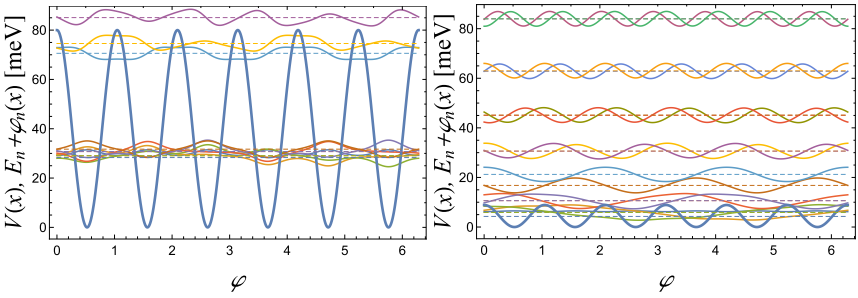

Figure 6.13: The angular dependence of the calculated azimuthal potential (thick blue curve) experienced by the energy levels (dashed lines) and wave functions (solid lines) of D_2O molecule at (a) zero pressure and (b) $P = 4$ GPa. The energy barrier is progressively suppressed by the application of pressure and fully diminished at 4.5 GPa, creating a free rotating dipolar network system.

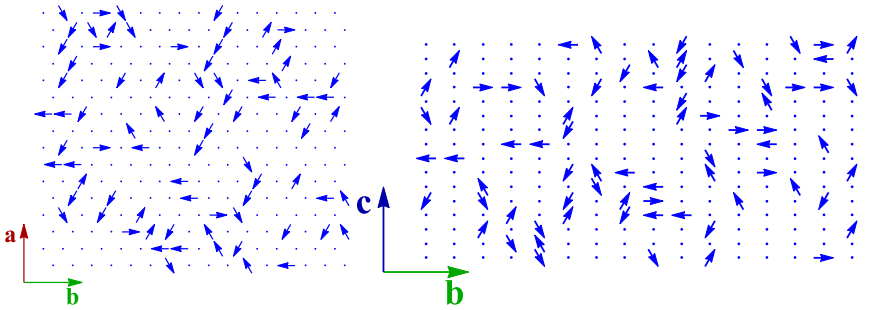

(a) (b)

Figure 6.14: (a)-(b) Water molecule dipole configuration in beryl at $T = 0\,\mathrm{K}$ obtained by Monte Carlo simulation. (a): both ferro/antiferro-electric orders can be obtained in-plane and a global ordering is absent. (b): It is important to note that the dipoles do not process component in the c-axis. For convenience, the c-axis components depicted here are actually the a-axis component. Neighbouring dipoles along the c-axis always align oppositely, so a global antiferroelectric order is expected.

INS experiments and was suggested to be no bigger than 8.4 meV [129]. This disagreement can be settled by, for example, including oxygen tunnelling. If the whole water molecule's translational and rotational tunnellings are considered [149], due to the mass increase, the corresponding V_0 for the same measured E_{01} would become smaller and so be closer to the literature value of the order of 10 meV.

A Monte Carlo simulation has also been conducted and brought insights into the in-plane and out-of-plane global dipoles order. Figures. 6.14(a)-(b) illustrate the water dipoles configuration at $T = 0\,\mathrm{K}$. It has revealed that with the presences of vacancies, *i.e.* the practical condition, the water dipoles in beryl do not necessarily align ferroelectrically in the plane. Meanwhile, along the c-direction, neighbouring dipoles are very much preferred to align oppositely. Therefore, under current conditions, no ferroelectric phase should be anticipated to be realised in water confined in beryl.

Another theoretical calculation of electric dipoles' order in a triangular lattice has been performed by collaborators Mr. Luka Jibuti and Prof. Dr. Peter

Buchler [150]. From their analysis of the dipole-dipole interaction energy, the dipoles on a single layer are energetically favoured to align in the same direction, *i.e.* ferroelectric order within one layer. The 3-dimensional dipole system is estimated by calculating the electric potential V experienced by a single dipole contributed by the seven closest dipoles from the neighbouring ordered layer. The schematic drawing of the theoretical system is borrowed and shown in fig. 6.15(a) and they obtained:

$$V = \frac{C_{dd}}{4\pi}\left(\frac{1}{c^3} - \frac{3(a^2-2c^2)}{(a^2+c^2)^{5/2}}\right)\cos(\theta) \tag{6.1}$$

$$\theta_c = \pi \tag{6.2}$$

where C_{dd} is the coupling constant, a and c are in-plane dipole separation and layers separation, respectively, θ is the angle of the dipole with respect to the a_1-axis, and θ_c is the angle with the lowest potential. The result indicated that, regardless of the layer separation, dipoles between layers are aligned antiferroelectrically (fig. 6.15(b)), so no ferroelectricity is going to be obtained macroscopically.

This theoretical work has assumed an ideal condition, namely a perfectly-filled impurity-free triangular lattice in the model, but there are two kinds of imperfections, vacancies and type-II water, in the realistic beryl sample. The effect of vacancy has also been considered in the theoretical work [150], which suggests that a vortex configuration is induced around the vacancy, which is thus absent from the global ferroelectric response (fig. 6.16(a)-(b)). Nonetheless, the vortex configuration is local and the ferroelectric order should be preserved in long-range, as illustrated in fig. 6.16(c).

The water dipoles in the beryl crystal are subjected to a 6-fold potential (fig. 3.12(b)) [129], which is neglected in this theoretical model. The height of the tunnelling peaks estimated from INS experiments are from 1.49 meV to 8.4 meV with an error bar of ±1.4 meV [129]. The interaction energy between the in-plane dipoles is estimated to be about 22 meV (*c.f.* sec. 3.2), so although the dipole-dipole interaction is still the dominant force, the environmental potential from the beryl cage is not negligible. Luckily, the

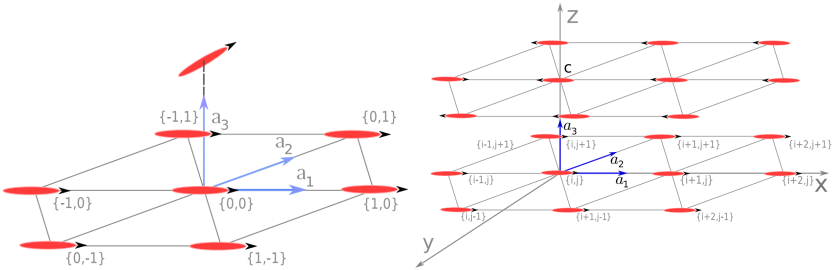

Figure 6.15: Theoretical calculation of the ground state of a two-layers triangular electric dipoles lattice [150]. (a) The 7 closest neighbouring dipoles accounted for the potential energy due to dipole-dipole interaction (eqn. 6.1). (b) The dipoles are aligned within the same layer but staggered between layers, so macroscopically antiferroelectric ordering is expected to be observed.

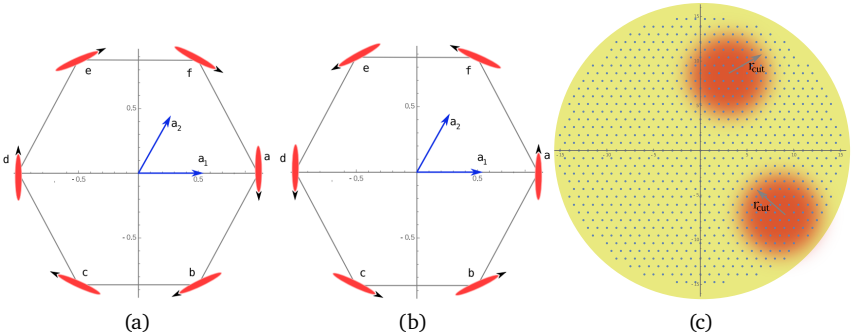

Figure 6.16: Schematic drawings of (a) clockwise and (b) anticlockwise vortex configuration of electric dipoles next to a vacancy in a trigular lattice [150]. (c) Estimation of defect-induced unpolarized domains [150]. The vortex configuration of dipoles takes place within the cutoff radius r_{cut} of the vacancy,. The regions beyond r_{cut} remain ferroelectrically ordered.

minima energy angles coincide with the neighbouring water dipoles' location, so the alignment with dipoles should not conflict, and the ignorance is justified. Nonetheless, a rigorous treatment is very much preferred for consolidating the understanding.

The two theoretical works share some accordances and provide insights in their own regard. Both works acquire vortex configuration with ab-plane in water-confining beryl with the presence of vacancies. The former Monte Carlo simulation obtains no sign of ferroelectric order even between nearest neighbouring dipoles, but the latter ideal quantum treatment suggests favourable ferroelectricity in-plane. It appears to be a high filling factor with minimal impurity will be one of the criteria for realising ferroelectric water. However, this possibility is restricted in 2-D plane, as both works reached the same conclusion as antiferroelectric order is robust along the c-direction, so global ferroelectricity is unlikely to be achieved in 3-D crystals.

Finally, the behaviours of beryl-H and beryl-D under pressure resemble a lot with the $SrTi^{16}O_3$ and $SrTi^{18}O_3$. As mentioned in sec. 2.5.4, the substitution of heavier isotope ^{18}O for ^{16}O has successfully brought up the ferroelectric transition, so the same mass enhancement has promoted FE in both $SrTiO_3$ and beryl systems. Upon pressure application, both beryl-D and $SrTi^{18}O_3$ suffer a suppression of PE divergence and gradually behave the same as their chemical counterpart. With the two echoing examples, it is strongly suggesting that, although the application of pressure enhances the strength of electric dipole-dipole interaction by reducing the spatial separations, the change in global geometry, in turn, jeopardizes the ferroelectric order. Overall, homogeneous physical pressure application tends to drive systems away from ferroelectric phase and into the quantum paraelectric phase.

6.5 Conclusion

Water confining beryl crystals are measured both at ambient and high pressure with multiple conditions. The correlations between conditions and the quantum paraelectric behaviour are discerned.

At ambient pressure, the effect of heavy isotope deuterium and the effect of type-II water (impurity) are sorted out. By substituting deuterium for hydrogen, the Curie-Weiss paraelectric divergence is greatly enhanced in rate of rise and the saturation plateau, which appears at about 20 K in H_2O-confining beryl, is absent down to 6 K. This observation aligns with the expectation of the promoted mode-softening due to the enhanced mass of electric dipoles. By reducing the concentration of water-II, the paraelectric divergence is significantly enhanced by 2.2 times in magnitude with no shift in starting temperature. It also matches with the expectation that water-II has its dipole locked by the impurity, so it is not involved in the polarization due to the external electric field itself and also sabotages its neighbouring water-I dipoles, leading to a huge reduction in free dipoles for their innate dipole-dipole interaction.

H_2O- and D_2O-confining beryl behave differently under high pressure but a universal trend can be drawn, as D_2O-beryl is restored to the state as H_2O-beryl under pressure. Upon pressurization up to 5 GPa, H_2O-confining beryl shows no sign of significant pressure dependence. The entire temperature evolution of dielectric permittivity is seemingly the same, with variations below the level of noise, in which a saturation plateau is developed at low temperature started around 20 K. D_2O-confining beryl, which exhibits no plateau and more robust paraelectric divergence at ambient pressures, shows a rapid suppression of the paraelectric divergence and the plateau emerges as pressure rises. Beyond 6 GPa, the amplitude of the divergence and the developing temperature of plateau match with that in H_2O-confining beryl. These observations suggest that the effect of homogeneous pressure, namely the action of dipoles' separations reduction from all 3 axes, is driving the water-confining system away from ordering and counteract the benefits from substitution of a heavy isotope.

Two theoretical works, a Monte Carlo simulation and a quantum mechanical treatment on an ideal triangular lattice, were conducted by collaborators. Both works suggest that the vortex configuration of dipoles will develop in-plane around vacancies. Although the latter treatment raises the possibility of ferroelectric order in-plane with perfect filling factor, the dipoles are

robustly aligned oppositely in the c-direction, so no global ferroelectric water shall be realised in beryl crystals. Application of physical pressure would reduce the azimuthal potential of dipoles and even fully eliminate barriers beyond $P = 4.5\,\mathrm{GPa}$, bringing the system towards the ideal free rotating picture. However, pressure also drives T_c away from positivity, meaning further away from the ferroelectric phase, and it is attributed to the increased dipole-dipole interaction along the c-direction. A similar observation under pressure has once been found in ferroelectric $SrTi^{16}O_3$ and $SrTi^{18}O_3$ systems. Because of these, it is inclined to conclude that the application of isotropic (homogeneous) physical pressure is not beneficial for FE realization in water-confining beryl.

In the future, it is still hopeful to realise FE phase in water-confining beryl via uniaxial pressurization along ab-plane and very high filling quality. In this case, the in-plane dipole-dipole interaction is maximized with no interruption from impurity or vacancy. Uniaxial pressure reduces the separation between water molecules in-plane while the out-of-plane separation increases because of stress release. Such that, the coupling between layers is weakened and could potentially create individually isolated 2-D layers, and all layers can be polarized in the same direction by applying a strong external electric field, accomplishing FE water.

Chapter 7

Conclusion

This thesis expanded the experimental physical pressure limit of the in-house dielectric measurement setup with the incorporation of diamond anvil cells (DAC). The incorporated setup (DAC-dielectric) has been characterized compliantly and is qualified for actual measurements by examining the inherent noise. Two condensed matter systems have been studied via the DAC-dielectric. Each system demands different capabilities of the setup and thus demonstrates the versatility and importance of this experimental improvement in this thesis.

7.1 DAC-dielectric establishment

The preparation setup and procedures for dielectric measurements under pressure via DAC is developed. The major challenge for DAC-dielectric, to secure an unattenuated export of electrical signal, is fulfilled by channels construction inside the pressurized cavity and introduction of coaxial cables close to the gasket.

Characterization of the DAC-dielectric recorded a low open capacitance, in order of fF, and low short inductance, in order of nH at $f = 10^6$ Hz. There

is no significant stray capacitance or wire loop resonation due to the cavity, and so a clean signal can be exported from the DAC. The long length of exposed wires, about the full diameter of the anvil seat, is the major source of performance loss. It resulted in a high noise-to-signal ratio, or even broken data, when approaching the frequency limits, especially beyond 10^6 Hz. Nonetheless, data within 10^{-2} to 10^6 Hz were testified to have satisfactory quality.

The highest pressure DAC-dielectric has reached is 7 GPa, from the beryl measurements. It was diagnosed the pressure ceiling because of the hole expansion along with the channel direction deformation of electrodes due to reduced thickness. Such that the pressure ceiling could be raised by improving the channel's hardness and thicker starting cavity. In the longer run, the adaptation of insulating materials or embedded-leads anvils would be the next milestone for achieving high consistency and overall performance.

7.2 Hybrid perovskite $CH_3NH_3PbX_3$

The halide series of methylammonium lead perovskite ($CH_3NH_3PbX_3$ ($X =$ I, Br or Cl)) have been measured up to 5 GPa. Four aspects of the dielectric properties of $CH_3NH_3PbX_3$ (MAPX) are examined and insights have been collected for improvement in photovoltaic performance.

The evolution of lattice structure under physical pressure and at low temperature is determined for all three halides of MAPX. By incorporating DAC-dielectric into cryogenics, the full T-P structure phase diagrams are probed. The identities of low-temperature and high-pressure structural phases are ascertained, and the stabilization of low-temperature orthorhombic phase is therefore discovered. A trend of development in the phase diagram, diminishing of intermediate tetragonal phase and replacement by cubic or orthorhombic phases, is found along the chemical doping from $X =$ I to Cl. The stabilization pressure of the low-temperature orthorhombic phase P^* is 3.2, 2.6 and 2 GPa for $X =$ I, Br and Cl, respectively, *i.e.* smaller halide ion, higher P^*.

The effect of pressure on the ion migration phenomena is examined. The degree of ion migration is generally suppressed with the increase in pressure, but sudden gain might appear across structural phase transitions. The ion migration can be completely negated deep into the high-pressure orthorhombic at pressure $P_{\text{flat}} = 4.5$, 4.3, 3.8 GPa for $X =$ I, Br and Cl, respectively. Apparently, the ion migration is allowed under ambient conditions because of the high symmetry and adequate inter-atoms space. Substitution of smaller ions, which promotes the orthorhombic phase realization and reduces neighbouring atom's distance shall diminish ion migration and thus improve stability and performance.

Frequency spectra of dielectric properties under pressure also captured a disappearance of relaxation in the orthorhombic phase. A dielectric relaxation at 1 kHz is found in low-pressure cubic and tetragonal phases in MAPX but is suddenly absent in the high-pressure orthorhombic phase. By comparing the known molecular or ionic motions in MAPX from the literature, this kHz relaxation is suggested here to be the translational motion of MA^+ cation within or between inorganic cages.

Finally, the nature of the reversible amorphization in MAPX at high pressure is commented on. The feature of structural transition, a sharp drop in real dielectric permittivity, is observed to be broadened alongside the increase in pressure. Together with the abnormal reversibility, the thesis, therefore, suggests it is indeed an inhomogeneous distortion of lattice because of the unsynchronized transitions among the crystals.

The next step following these findings is naturally the examination of heavier cations, for instance, formamidinium cation (FA^+). At the time of writing this thesis, it has already been demonstrated that a prototype of $FAPbI_3$ solar cells possess higher light-harvesting efficiency than the MA^+ counterpart. It would be beneficial to clarify if there is a universal relationship between crystal structure and photovoltaic performance among the hybrid organic-inorganic halide perovskite series.

7.3 Water-confining beryl

H_2O and D_2O confined beryl crystals with impurity gradient are characterized both at ambient pressure and up to 7 GPa.

At ambient pressure, multiple beryl samples with different conditions are comparatively measured. There is no hysteresis observed which implies the quantum paraelectric behaviour is not second order. Both substitution of H_2O to D_2O and reduction of impurities have demonstrated an enhancement of the Curie-Weiss paraelectric divergence at low temperature, *i.e.* the electric dipole ordering. The characteristic plateau for quantum paraelectricity is not realised in D_2O sample, but yet no transition is obtained. The D_2O-containing beryl crystal with the lowest impurity (beryl-D) and the pioneer H_2O-containing beryl (beryl-H) crystals have proceeded for pressure measurements.

For beryl-H, there is no apparent effect from pressure noticed up to 5 GPa. The entire temperature dependence remains unvaried throughout the pressure cycle. It is indicative that the quantum effect is saturated at ambient conditions and the interstitial distance between dipoles takes no role in the observed order prohibition.

For beryl-D, the enhanced Curie-Weiss paraelectric divergence has dwindled as the applied pressure rises alongside the resurrection of the plateau. Barrett equation fittings on the refined data yield a saturation of quantum effect, accompanied by a decline of critical temperature further into negativity, at $P > 4.5\,\text{GPa}$. The saturation of the quantum effect is conceived as the result of localizing potential barrier suppression. Two theoretical approaches conclude a prone to vacancy in-plane ferroelectric (FE) orders and a robust along-channel antiferroelectric (AFM) order in the beryl water dipoles network. As beryl crystal processes anisotropic compressibility, in which in-plane separation is compressed less than the channel axis, the drastic growth in negative critical temperature is attributed to the domination of the promoted AFM coupling as it outgrows the in-plane FE competitor.

In the future, in-plane uniaxial pressure application and softer lattices with higher potential barriers shall be the directions. The former allows

strain release in the channel axis, so the AFM ordering is weakened and the in-plane FE coupling strength might be able to overtake. The latter allows further lattice compression while preventing the disappearance of quantized localization of dipoles, so the original idea of aligning long-range dipoles with the significantly reinforced coupling can be realized.

Acknowledgements

The completion of this thesis is made possible with the help received from many beloved and brilliant people.

Utmost gratitude is extended to Prof. Martin Dressel. It is my pleasure to be granted the opportunity for doing my thesis in the 1. Physikalisces Institut. Many insights can be gained through discussions with him, because of his vast knowledge across research areas and perceptiveness. His supervision is meticulous and efficient. I particularly enjoy the energetic atmosphere he created in the institute.

Sincere gratitude is expressed to Prof. Peter Büchler and Prof. Hidenori Takagi for their willingness to be the chairman and co-referee on my dissertation committee.

Dr. Ece Uykur is the other supervisor of mine. She is a paragon of scientists. Her dedication and enthusiasm are stunning and admirable. Imitation to her shaped much of my personality. She is also a kind and down-to-earth person. Working with her has been a pleasing experience.

Prof. Boris Gorshunov, Dr. Veniamin Abalmasov, and Dr. Mikhail Belyanchikov are the collaborators of the beryl project. Besides providing me the high-quality single crystals, they have also provided me with fruitful discussions and guidance.

Gabriele Untereiner is crucial throughout the course of development and measurements. Her expertise in chemistry and sample preparation has helped in every way. In particular, she has prepared me with countless

contacted samples, for which I will be forever grateful.

I would also have to thank the experts from the mechanical and low-temperature workshop. The former manufactured parts for my special needs; the latter supplied liquid helium whenever requested. Their professionalism is commendable.

It is necessary to mention our secretaries, Agnieszka Cienkowska-Schmidt and Olga Weber for taking care of the paperwork and the peripherals in the institute. Their swift actions in solving administrative issues have promoted everyone's work around the institute.

Special mention to Dr. Roland Rösslhuber, the predecessor and developer of the pressurized dielectric spectroscopy setup. The setup I received is in perfect working condition, supplied with comprehensive and detailed instructions. Discussion with him in the beginning helped me to quickly pick up the technique. He also played the role of mentor in preparing me to fit into the new environment.

Thanks to all of the colleagues that I met in the institute: Sascha, Olga, Tobias, Lucky, Ananya, Artem, Suelki, and many others. We are all gathered together because we are similar, yet we are different. I have learned something from each of you, and I hope this experience is mutual. In addition, thank you for the joy.

Finally, I would like to thank my family and friends, as always.

Bibliography

[1] P. W. Anderson, 'More is different', *Science*, vol. 177, no. 4047, pp. 393–396, Aug. 1972 (cit. on p. 22).

[2] T. Ivek, B. Korin-Hamzić, O. Milat, S. Tomić, C. Clauss, N. Drichko, D. Schweitzer, M. Dressel, 'Collective excitations in the charge-ordered phase of α-(BEDT-TTF)$_2$I$_3$', *Physical Review Letters*, vol. 104, no. 20, p. 206 406, May 2010 (cit. on p. 23).

[3] T. Ivek, B. Korin-Hamzić, O. Milat, S. Tomić, C. Clauss, N. Drichko, D. Schweitzer, M. Dressel, 'Electrodynamic response of the charge ordering phase: Dielectric and optical studies of α-(BEDT-TTF)$_2$I$_3$', *Physical Review B*, vol. 83, no. 16, p. 165 128, Apr. 2011 (cit. on pp. 23, 32).

[4] J. Hemberger, P. Lunkenheimer, R. Fichtl, H.-A. K. von Nidda, V. Tsurkan, A. Loidl, 'Relaxor ferroelectricity and colossal magnetocapacitive coupling in ferromagnetic CdCr$_2$S$_4$', *Nature*, vol. 434, no. 7031, pp. 364–367, Mar. 2005 (cit. on p. 23).

[5] P. Lunkenheimer, J. Müller, S. Krohns, F. Schrettle, A. Loidl, B. Hartmann, R. Rommel, M. de Souza, C. Hotta, J. A. Schlueter, M. Lang, 'Multiferroicity in an organic charge-transfer salt that is suggestive of electric-dipole-driven magnetism', *Nature Materials*, vol. 11, no. 9, pp. 755–758, Aug. 2012 (cit. on p. 23).

[6] B. Miksch, A. Pustogow, M. J. Rahim, A. A. Bardin, K. Kanoda, J. A. Schlueter, R. Hübner, M. Scheffler, M. Dressel, 'Gapped magnetic ground state in quantum spin liquid candidate κ-(BEDT-TTF)$_2$Cu$_2$(CN)$_3$', *Science*, vol. 372, no. 6539, pp. 276–279, Apr. 2021 (cit. on p. 23).

[7] M. Dressel, 'Ordering phenomena in quasi-one-dimensional organic conductors', *Naturwissenschaften*, vol. 94, no. 7, pp. 527–541, May 2007 (cit. on p. 23).

[8] S. Tomić, M. Dressel, 'Ferroelectricity in molecular solids: A review of electrodynamic properties', *Reports on Progress in Physics*, vol. 78, no. 9, p. 096 501, Jul. 2015 (cit. on pp. 23, 41).

[9] A. Pustogow, M. Bories, A. Löhle, R. Rösslhuber, E. Zhukova, B. Gorshunov, S. Tomić, J. A. Schlueter, R. Hübner, T. Hiramatsu, Y. Yoshida, G. Saito, R. Kato, T.-H. Lee, V. Dobrosavljević, S. Fratini, M. Dressel, 'Quantum spin liquids unveil the genuine mott state', *Nature Materials*, vol. 17, no. 9, pp. 773–777, Aug. 2018 (cit. on p. 23).

[10] R. Rösslhuber, A. Pustogow, E. Uykur, A. Böhme, A. Löhle, R. Hübner, J. A. Schlueter, Y. Tan, V. Dobrosavljević, M. Dressel, 'Phase coexistence at the first-order mott transition revealed by pressure-dependent dielectric spectroscopy of κ-(BEDT-TTF)$_2$-Cu$_2$(CN)$_3$', *Physical Review B*, vol. 103, no. 12, p. 125 111, Mar. 2021 (cit. on p. 23).

[11] T. Leijtens, G. E. Eperon, N. K. Noel, S. N. Habisreutinger, A. Petrozza, H. J. Snaith, 'Stability of metal halide perovskite solar cells', *Advanced Energy Materials*, vol. 5, no. 20, p. 1 500 963, Sep. 2015 (cit. on p. 24).

[12] T. A. Berhe, W.-N. Su, C.-H. Chen, C.-J. Pan, J.-H. Cheng, H.-M. Chen, M.-C. Tsai, L.-Y. Chen, A. A. Dubale, B.-J. Hwang, 'Organometal halide perovskite solar cells: Degradation and stability', *Energy & Environmental Science*, vol. 9, no. 2, pp. 323–356, 2016 (cit. on p. 24).

[13] B. Saparov, D. B. Mitzi, 'Organic–inorganic perovskites: Structural versatility for functional materials design', *Chemical Reviews*, vol. 116, no. 7, pp. 4558–4596, Apr. 2016 (cit. on p. 24).

[14] B. P. Gorshunov, V. I. Torgashev, E. S. Zhukova, V. G. Thomas, M. A. Belyanchikov, C. Kadlec, F. Kadlec, M. Savinov, T. Ostapchuk, J. Petzelt, J. Prokleška, P. V. Tomas, E. V. Pestrjakov, D. A. Fursenko, G. S. Shakurov, A. S. Prokhorov, V. S. Gorelik, L. S. Kadyrov, V. V. Uskov, R. K. Kremer, M. Dressel, 'Incipient ferroelectricity of water molecules confined to nano-channels of beryl', *Nature Communications*, vol. 7, no. 1, Sep. 2016 (cit. on pp. 24, 72–75, 77, 132, 137, 140, 141).

[15] D. Griffiths, *Introduction to Electrodynamics*. Cambridge: Cambridge University Press, 2017 (cit. on p. 25).

[16] M. Dressel, G. Grüner, *Electrodynamics of Solids*. Cambridge University Press, Jan. 2002 (cit. on p. 27).

[17] K. W. Wagner, 'Erklärung der dielektrischen nachwirkungsvorgänge auf grund maxwellscher vorstellungen', *Archiv für Elektrotechnik*, vol. 2, no. 9, pp. 371–387, Sep. 1914 (cit. on p. 28).

[18] F. Kremer, A. Schönhals, Eds., *Broadband Dielectric Spectroscopy*. Springer Berlin Heidelberg, 2003 (cit. on pp. 28, 65, 80, 82).

[19] Y. Chen, D. Or, 'Effects of Maxwell-Wagner polarization on soil complex dielectric permittivity under variable temperature and electrical conductivity', *Water Resources Research*, vol. 42, no. 6, Jun. 2006 (cit. on p. 29).

[20] L. Solymar, D. Walsh, R. R. A. Syms, *Electrical Properties of Materials*. Oxford University Press, Oct. 2010 (cit. on pp. 28, 37).

[21] C. P. Lindsey, G. D. Patterson, 'Detailed comparison of the Williams-Watts and Cole-Davidson functions', *The Journal of Chemical Physics*, vol. 73, no. 7, pp. 3348–3357, Oct. 1980 (cit. on p. 33).

[22] P. Lunkenheimer, U. Schneider, R. Brand, A. Loid, 'Glassy dynamics', *Contemporary Physics*, vol. 41, no. 1, pp. 15–36, Jan. 2000 (cit. on pp. 33, 34, 80, 82).

[23] P. Lunkenheimer, A. Loidl, 'Dielectric spectroscopy on organic charge-transfer salts', *Journal of Physics: Condensed Matter*, vol. 27, no. 37, p. 373 001, Sep. 2015 (cit. on pp. 34, 52).

[24] A. E. Glazounov, A. K. Tagantsev, 'Direct evidence for Vögel–Fulcher freezing in relaxor ferroelectrics', *Applied Physics Letters*, vol. 73, no. 6, pp. 856–858, Aug. 1998 (cit. on p. 35).

[25] M. Abdel-Jawad, I. Terasaki, T. Sasaki, N. Yoneyama, N. Kobayashi, Y. Uesu, C. Hotta, 'Anomalous dielectric response in the dimer mott insulator κ-(BEDT-TTF)$_2$Cu$_2$(CN)$_3$', *Physical Review B*, vol. 82, no. 12, p. 125 119, Sep. 2010 (cit. on p. 35).

[26] P. Chandra, G. G. Lonzarich, S. E. Rowley, J. F. Scott, 'Prospects and applications near ferroelectric quantum phase transitions: A key issues review', *Reports on Progress in Physics*, vol. 80, no. 11, p. 112 502, Sep. 2017 (cit. on pp. 36, 40, 45).

[27] J. F. Scott, 'Applications of modern ferroelectrics', *Science*, vol. 315, no. 5814, pp. 954–959, Feb. 2007 (cit. on pp. 36, 38).

[28] W. Heywang, *Piezoelectricity : evolution and future of a technology*. Berlin: Springer, 2008 (cit. on pp. 36–38, 40, 43).

[29] C. Kittel, *Introduction to Solid State Physics*. WILEY, Nov. 2004, 680 pp. [Online]. Available: https://www.ebook.de/de/product/4290142/charles_kittel_introduction_to_solid_state_physics.html (cit. on p. 38).

[30] G. Liu, S. Zhang, W. Jiang, W. Cao, 'Losses in ferroelectric materials', *Materials Science and Engineering: R: Reports*, vol. 89, pp. 1–48, Mar. 2015 (cit. on p. 39).

[31] S. E. Rowley, L. J. Spalek, R. P. Smith, M. P. M. Dean, M. Itoh, J. F. Scott, G. G. Lonzarich, S. S. Saxena, 'Ferroelectric quantum criticality', *Nature Physics*, vol. 10, no. 5, pp. 367–372, Mar. 2014 (cit. on pp. 39, 45, 47, 51).

[32] W. J. Merz, 'The electric and optical behavior of $BaTiO_3$ single-domain crystals', *Physical Review*, vol. 76, no. 8, p. 1221, 1949 (cit. on p. 42).

[33] J. Hlinka, T. Ostapchuk, D. Nuzhnyy, J. Petzelt, P. Kuzel, C. Kadlec, P. Vanek, I. Ponomareva, L. Bellaiche, 'Coexistence of the phonon and relaxation soft modes in the terahertz dielectric response of tetragonal $BaTiO_3$', *Physical Review Letters*, vol. 101, no. 16, p. 167 402, Oct. 2008 (cit. on p. 41).

[34] K. A. Müller, H. Burkard, '$SrTiO_3$: An intrinsic quantum paraelectric below 4 K', *Physical Review B*, vol. 19, no. 7, pp. 3593–3602, Apr. 1979 (cit. on pp. 41, 44).

[35] L. Pálová, P. Chandra, P. Coleman, 'Quantum critical paraelectrics and the casimir effect in time', *Physical Review B*, vol. 79, no. 7, p. 075 101, Feb. 2009 (cit. on pp. 44, 45, 48).

[36] K. A. Müller, W. Berlinger, E. Tosatti, 'Indication for a novel phase in the quantum paraelectric regime of $SrTiO_3$', *Zeitschrift für Physik B Condensed Matter*, vol. 84, no. 2, pp. 277–283, Jun. 1991 (cit. on p. 41).

[37] R. M. Smith, J. Gardner, F. D. Morrison, S. E. Rowley, C. Ferraz, M. A. Carpenter, J. Chen, J. Hodkinson, S. E. Dutton, J. F. Scott, 'Quantum critical points in ferroelectric relaxors: Stuffed tungsten bronze $K_3Li_2Ta_5O_{15}$ and lead pyrochlore ($Pb_2Nb_2O_7$)', *Phys. Rev. Materials*, vol. 2, no. 8, p. 084 409, Aug. 2018 (cit. on p. 41).

[38] S. Horiuchi, Y. Okimoto, R. Kumai, Y. Tokura, 'Quantum phase transition in organic charge-transfer complexes', *Science*, vol. 299, no. 5604, pp. 229–232, Jan. 2003 (cit. on p. 41).

[39] F. Kagawa, N. Minami, S. Horiuchi, Y. Tokura, 'Athermal domain-wall creep near a ferroelectric quantum critical point', *Nat. Commun.*, vol. 7, no. 1, p. 10 675, Feb. 2016 (cit. on p. 41).

[40] F. Kagawa, S. Horiuchi, Y. Tokura, 'Quantum phenomena emerging near a ferroelectric critical point in a donor–acceptor organic charge-transfer complex', *Crystals*, vol. 7, no. 4, p. 106, Apr. 2017 (cit. on p. 41).

[41] M. Dressel, S. Tomić, 'Molecular quantum materials: Electronic phases and charge dynamics in two-dimensional organic solids', *Adv. Phys.*, vol. 69, p. 1, 2021 (cit. on p. 41).

[42] S.-P. Shen, Y.-S. Chai, J.-Z. Cong, P.-J. Sun, J. Lu, L.-Q. Yan, S.-G. Wang, Y. Sun, 'Magnetic-ion-induced displacive electric polarization in FeO_5 bipyramidal units of (Ba,Sr)$Fe_{12}O_{19}$ hexaferrites', *Phys. Rev. B*, vol. 90, no. 18, p. 180 404, Nov. 2014 (cit. on p. 41).

[43] H. B. Cao, Z. Y. Zhao, M. Lee, E. S. Choi, M. A. McGuire, B. C. Sales, H. D. Zhou, J.-Q. Yan, D. G. Mandrus, 'High pressure floating zone growth and structural properties of ferrimagnetic quantum paraelectric $BaFe_{12}O_{19}$', *APL Materials*, vol. 3, no. 6, p. 062 512, Jun. 2015 (cit. on p. 41).

[44] J. H. Barrett, 'Dielectric constant in perovskite type crystals', *Physical Review*, vol. 86, no. 1, pp. 118–120, Apr. 1952 (cit. on p. 43).

[45] J. Dec, W. Kleemann, 'From Barrett to generalized quantum Curie–Weiss law', *Solid State Communications*, vol. 106, no. 10, pp. 695–699, Apr. 1998 (cit. on p. 43).

[46] O. E. Kvyatkovskii, 'Quantum effects in incipient and low-temperature ferroelectrics (a review)', *Physics of the Solid State*, vol. 43, no. 8, pp. 1401–1419, Aug. 2001 (cit. on pp. 43, 45, 74).

[47] R. A. Parker, 'Static dielectric constant of rutile (TiO_2), 1.6-1060 °K', *Physical Review*, vol. 124, no. 6, pp. 1719–1722, Dec. 1961 (cit. on pp. 45, 46).

[48] D. Rytz, U. T. Höchli, H. Bilz, 'Dielectric susceptibility in quantum ferroelectrics', *Physical Review B*, vol. 22, no. 1, pp. 359–364, Jul. 1980 (cit. on p. 45).

[49] A. R. Akbarzadeh, L. Bellaiche, K. Leung, J. Íñiguez, D. Vanderbilt, 'Atomistic simulations of the incipient ferroelectric $KTaO_3$', *Physical Review B*, vol. 70, no. 5, p. 054 103, Aug. 2004 (cit. on pp. 45, 46).

[50] V. Lemanov, A. Sotnikov, E. Smirnova, M. Weihnacht, R. Kunze, 'Perovskite $CaTiO_3$ as an incipient ferroelectric', *Solid State Communications*, vol. 110, no. 11, pp. 611–614, May 1999 (cit. on pp. 45, 46).

[51] V. V. Lemanov, A. V. Sotnikov, E. P. Smirnova, M. Weihnacht, 'From incipient ferroelectricity in $CaTiO_3$ to real ferroelectricity in $Ca_{1-x}Pb_xTiO_3$ solid solutions', *Applied Physics Letters*, vol. 81, no. 5, pp. 886–888, Jul. 2002 (cit. on p. 45).

[52] S.-P. Shen, J.-C. Wu, J.-D. Song, X.-F. Sun, Y.-F. Yang, Y.-S. Chai, D.-S. Shang, S.-G. Wang, J. F. Scott, Y. Sun, 'Quantum electric-dipole liquid on a triangular lattice', *Nature Communications*, vol. 7, no. 1, Feb. 2016 (cit. on pp. 45, 46).

[53] V. V. Lemanov, 'Improper ferroelastic $SrTiO_3$ and what we know today about its properties', *Ferroelectrics*, vol. 265, no. 1, pp. 1–21, Jan. 2002 (cit. on p. 45).

[54] D. Khmel'Nitskiĭ, V. Shneerson, 'Phase transitions of the displacement type in crystals at very low temperatures', *Soviet Journal of Experimental and Theoretical Physics*, vol. 37, p. 164, 1973 (cit. on p. 45).

[55] S. E. Rowley, M. Hadjimichael, M. N. Ali, Y. C. Durmaz, J. C. Lashley, R. J. Cava, J. F. Scott, 'Quantum criticality in a uniaxial organic ferroelectric', *Journal of Physics: Condensed Matter*, vol. 27, no. 39, p. 395 901, Sep. 2015 (cit. on pp. 48, 49).

[56] H. Uwe, T. Sakudo, 'Stress-induced ferroelectricity and soft phonon modes in $SrTiO_3$', *Physical Review B*, vol. 13, no. 1, pp. 271–286, Jan. 1976 (cit. on p. 49).

[57] J. G. Bednorz, K. A. Müller, '$Sr_{1-x}Ca_xTiO_3$: An XY quantum ferroelectric with transition to randomness', *Physical Review Letters*, vol. 52, no. 25, pp. 2289–2292, Jun. 1984 (cit. on p. 49).

[58] M. Itoh, R. Wang, 'Quantum ferroelectricity in $SrTiO_3$ induced by oxygen isotope exchange', *Applied Physics Letters*, vol. 76, no. 2, pp. 221–223, Jan. 2000 (cit. on pp. 49, 51).

[59] R. Wang, N. Sakamoto, M. Itoh, 'Effects of pressure on the dielectric properties of $SrTi_{18}O_3$ and $SrTi_{16}O_3$ single crystals', *Physical Review B*, vol. 62, no. 6, R3577–R3580, Aug. 2000 (cit. on pp. 49–51).

[60] P. Roth, E. Hegenbarth, M. Muller, U. Escher, 'Deviations from curie-weiss behavior of $(Ba_{0.06}Sr_{0.94})TiO_3$ caused by high hydrostatic pressure due to quantum effects', *Ferroelectrics*, vol. 74, no. 1, pp. 331–337, Aug. 1987 (cit. on p. 49).

[61] M. J. Coak, C. R. S. Haines, C. Liu, G. G. Guzmán-Verri, S. S. Saxena, 'Pressure dependence of ferroelectric quantum critical fluctuations', *Physical Review B*, vol. 100, no. 21, p. 214 111, Dec. 2019 (cit. on pp. 49, 51).

[62] Y. Yuan, J. Huang, 'Ion migration in organometal trihalide perovskite and its impact on photovoltaic efficiency and stability', *Accounts of Chemical Research*, vol. 49, no. 2, pp. 286–293, Jan. 2016 (cit. on p. 54).

[63] N.-G. Park, M. Grätzel, T. Miyasaka, Eds., *Organic-Inorganic Halide Perovskite Photovoltaics*. Springer International Publishing, 2016 (cit. on pp. 54, 55).

[64] L. M. Rodriguez-Martinez, J. P. Attfield, 'Cation disorder and size effects in magnetoresistive manganese oxide perovskites', *Physical Review B*, vol. 54, no. 22, R15622–R15625, Dec. 1996 (cit. on p. 57).

[65] A. P. Ramirez, 'Colossal magnetoresistance', *Journal of Physics: Condensed Matter*, vol. 9, no. 39, pp. 8171–8199, Sep. 1997 (cit. on p. 57).

[66] I. Grinberg, D. V. West, M. Torres, G. Gou, D. M. Stein, L. Wu, G. Chen, E. M. Gallo, A. R. Akbashev, P. K. Davies, J. E. Spanier, A. M. Rappe, 'Perovskite oxides for visible-light-absorbing ferroelectric and photovoltaic materials', *Nature*, vol. 503, no. 7477, pp. 509–512, Nov. 2013 (cit. on p. 57).

[67] Y. Maeno, H. Hashimoto, K. Yoshida, S. Nishizaki, T. Fujita, J. G. Bednorz, F. Lichtenberg, 'Superconductivity in a layered perovskite without copper', *Nature*, vol. 372, no. 6506, pp. 532–534, Dec. 1994 (cit. on p. 57).

[68] A. Kojima, K. Teshima, Y. Shirai, T. Miyasaka, 'Organometal halide perovskites as visible-light sensitizers for photovoltaic cells', *Journal of the American Chemical Society*, vol. 131, no. 17, pp. 6050–6051, May 2009 (cit. on p. 58).

[69] M. Grätzel, 'The light and shade of perovskite solar cells', *Nature Materials*, vol. 13, no. 9, pp. 838–842, Aug. 2014 (cit. on p. 58).

[70] 'Perovskite fever', *Nature Materials*, vol. 13, no. 9, pp. 837–837, Aug. 2014 (cit. on p. 58).

[71] J. Jeong, M. Kim, J. Seo, H. Lu, P. Ahlawat, A. Mishra, Y. Yang, M. A. Hope, F. T. Eickemeyer, M. Kim, Y. J. Yoon, I. W. Choi, B. P. Darwich, S. J. Choi, Y. Jo, J. H. Lee, B. Walker, S. M. Zakeeruddin, L. Emsley, U. Rothlisberger, A. Hagfeldt, D. S. Kim, M. Grätzel, J. Y. Kim, 'Pseudo-halide anion engineering for α-$FAPbI_3$ perovskite solar cells', *Nature*, Apr. 2021 (cit. on p. 58).

[72] N. Onoda-Yamamuro, T. Matsuo, H. Suga, 'Calorimetric and IR spectroscopic studies of phase transitions in methylammonium trihalogenoplumbates (II)†', *Journal of Physics and Chemistry of Solids*, vol. 51, no. 12, pp. 1383–1395, Jan. 1990 (cit. on pp. 58, 59).

[73] N. Onoda-Yamamuro, T. Matsuo, H. Suga, 'Dielectric study of $CH_3NH_3PbX_3$ (X = Cl, Br, I)', *Journal of Physics and Chemistry of Solids*, vol. 53, no. 7, pp. 935–939, Jul. 1992 (cit. on pp. 58, 59, 62, 68).

[74] R. Wasylishen, O. Knop, J. Macdonald, 'Cation rotation in methylammonium lead halides', *Solid State Communications*, vol. 56, no. 7, pp. 581–582, Nov. 1985 (cit. on pp. 60, 68, 69, 124).

[75] Q. Xu, T. Eguchi, H. Nakayama, N. Nakamura, M. Kishita, 'Molecular motions and phase transitions in solid $CH_3NH_3PbX_3$ (X = Cl, Br, I) as studied by NMR and NQR', *Zeitschrift für Naturforschung A*, vol. 46, no. 3, pp. 240–246, Mar. 1991 (cit. on pp. 60, 67, 68, 124).

[76] M. T. Weller, O. J. Weber, P. F. Henry, A. M. D. Pumpo, T. C. Hansen, 'Complete structure and cation orientation in the perovskite photovoltaic methylammonium lead iodide between 100 and 352 K', *Chemical Communications*, vol. 51, no. 20, pp. 4180–4183, 2015 (cit. on pp. 60, 69).

[77] D. H. Fabini, T. Hogan, H. A. Evans, C. C. Stoumpos, M. G. Kanatzidis, R. Seshadri, 'Dielectric and thermodynamic signatures of low-temperature glassy dynamics in the hybrid perovskites $CH_3NH_3PbI_3$ and $HC(NH_2)_2PbI_3$', *The Journal of Physical Chemistry Letters*, vol. 7, no. 3, pp. 376–381, Jan. 2016 (cit. on pp. 60, 61, 65).

[78] T. Chen, B. J. Foley, B. Ipek, M. Tyagi, J. R. D. Copley, C. M. Brown, J. J. Choi, S.-H. Lee, 'Rotational dynamics of organic cations in the $CH_3NH_3PbI_3$ perovskite', *Physical Chemistry Chemical Physics*, vol. 17, no. 46, pp. 31 278–31 286, 2015 (cit. on p. 60).

[79] N. Onoda-Yamamuro, O. Yamamuro, T. Matsuo, H. Suga, 'p-T phase relations of $CH_3NH_3PbI_3$ (X = Cl, Br, I) crystals', *Journal of Physics and Chemistry of Solids*, vol. 53, no. 2, pp. 277–281, Feb. 1992 (cit. on pp. 60, 61, 104).

[80] K. Gesi, 'Effect of hydrostatic pressure on the structural phase transitions in $CH_3NH_3PbX_3$ (X = Cl, Br, I)', *Ferroelectrics*, vol. 203, no. 1, pp. 249–268, Nov. 1997 (cit. on pp. 60–63, 102, 104).

[81] I. P. Swainson, M. G. Tucker, D. J. Wilson, B. Winkler, V. Milman, 'Pressure response of an organic-inorganic perovskite: methylammonium lead bromide', *Chemistry of Materials*, vol. 19, no. 10, pp. 2401–2405, May 2007 (cit. on pp. 60, 62, 64).

[82] A. Jaffe, Y. Lin, C. M. Beavers, J. Voss, W. L. Mao, H. I. Karunadasa, 'High-pressure single-crystal structures of 3D lead-halide hybrid perovskites and pressure effects on their electronic and optical properties', *ACS Central Science*, vol. 2, no. 4, pp. 201–209, Apr. 2016 (cit. on p. 62).

[83] L. Wang, K. Wang, G. Xiao, Q. Zeng, B. Zou, 'Pressure-induced structural evolution and band gap shifts of organometal halide perovskite-based methylammonium lead chloride', *The Journal of Physical Chemistry Letters*, vol. 7, no. 24, pp. 5273–5279, Dec. 2016 (cit. on p. 64).

[84] M. Szafrański, A. Katrusiak, 'Photovoltaic hybrid perovskites under pressure', *The Journal of Physical Chemistry Letters*, vol. 8, no. 11, pp. 2496–2506, May 2017 (cit. on p. 64).

[85] Y. Wang, X. Lü, W. Yang, T. Wen, L. Yang, X. Ren, L. Wang, Z. Lin, Y. Zhao, 'Pressure-induced phase transformation, reversible amorphization, and anomalous visible light response in organolead bromide perovskite', *Journal of the American Chemical Society*, vol. 137, no. 34, pp. 11 144–11 149, Aug. 2015 (cit. on p. 64).

[86] A. Dualeh, T. Moehl, N. Tétreault, J. Teuscher, P. Gao, M. K. Nazeeruddin, M. Grätzel, 'Impedance spectroscopic analysis of lead iodide perovskite-sensitized solid-state solar cells', *ACS Nano*, vol. 8, no. 1, pp. 362–373, Dec. 2013 (cit. on pp. 65, 66).

[87] R. Gottesman, E. Haltzi, L. Gouda, S. Tirosh, Y. Bouhadana, A. Zaban, E. Mosconi, F. D. Angelis, 'Extremely slow photoconductivity response of $CH_3NH_3PbI_3$ perovskites suggesting structural changes under working conditions', *The Journal of Physical Chemistry Letters*, vol. 5, no. 15, pp. 2662–2669, Jul. 2014 (cit. on pp. 65, 67).

[88] W. Tress, N. Marinova, T. Moehl, S. M. Zakeeruddin, M. K. Nazeeruddin, M. Grätzel, 'Understanding the rate-dependent J–V hysteresis, slow time component, and aging in $CH_3NH_3PbI_3$ perovskite solar cells: The role of a compensated electric field', *Energy & Environmental Science*, vol. 8, no. 3, pp. 995–1004, 2015 (cit. on p. 65).

[89] Z. Xiao, Y. Yuan, Y. Shao, Q. Wang, Q. Dong, C. Bi, P. Sharma, A. Gruverman, J. Huang, 'Giant switchable photovoltaic effect in organometal trihalide perovskite devices', *Nature Materials*, vol. 14, no. 2, pp. 193–198, Dec. 2014 (cit. on p. 65).

[90] N. Pellet, P. Gao, G. Gregori, T.-Y. Yang, M. K. Nazeeruddin, J. Maier, M. Grätzel, 'Mixed-organic-cation perovskite photovoltaics for enhanced solar-light harvesting', *Angewandte Chemie International Edition*, vol. 53, no. 12, pp. 3151–3157, Feb. 2014 (cit. on p. 65).

[91] J. M. Frost, K. T. Butler, A. Walsh, 'Molecular ferroelectric contributions to anomalous hysteresis in hybrid perovskite solar cells', *APL Materials*, vol. 2, no. 8, p. 081 506, Aug. 2014 (cit. on p. 65).

[92] H. J. Snaith, A. Abate, J. M. Ball, G. E. Eperon, T. Leijtens, N. K. Noel, S. D. Stranks, J. T.-W. Wang, K. Wojciechowski, W. Zhang, 'Anomalous hysteresis in perovskite solar cells', *The Journal of Physical Chemistry Letters*, vol. 5, no. 9, pp. 1511–1515, Apr. 2014 (cit. on p. 65).

[93] A. M. A. Leguy, J. M. Frost, A. P. McMahon, V. G. Sakai, W. Kockelmann, C. Law, X. Li, F. Foglia, A. Walsh, B. C. O'Regan, J. Nelson, J. T. Cabral, P. R. F. Barnes, 'The dynamics of methylammonium ions in hybrid organic–inorganic perovskite solar cells', *Nature Communications*, vol. 6, no. 1, May 2015 (cit. on pp. 65, 67–69, 122, 124).

[94] D. Fan, J. Xu, Y. Kuang, X. Li, Y. Li, H. Xie, 'Compressibility and equation of state of beryl ($Be_3Al_2Si_6O_{18}$) by using a diamond anvil cell and in situ synchrotron X-ray diffraction', *Physics and Chemistry of Minerals*, vol. 42, no. 7, pp. 529–539, Mar. 2015 (cit. on pp. 65, 79, 141).

[95] T.-Y. Yang, G. Gregori, N. Pellet, M. Grätzel, J. Maier, 'The significance of ion conduction in a hybrid organic-inorganic lead-iodide-based perovskite photosensitizer', *Angewandte Chemie International Edition*, vol. 54, no. 27, pp. 7905–7910, May 2015 (cit. on pp. 65, 66, 105, 108, 119).

[96] J. G. Labram, D. H. Fabini, E. E. Perry, A. J. Lehner, H. Wang, A. M. Glaudell, G. Wu, H. Evans, D. Buck, R. Cotta, L. Echegoyen, F. Wudl, R. Seshadri, M. L. Chabinyc, 'Temperature-dependent polarization in field-effect transport and photovoltaic measurements of methylammonium lead iodide', *The Journal of Physical Chemistry Letters*, vol. 6, no. 18, pp. 3565–3571, Aug. 2015 (cit. on p. 65).

[97] A. Walsh, D. O. Scanlon, S. Chen, X. G. Gong, S.-H. Wei, 'Self-regulation mechanism for charged point defects in hybrid halide perovskites', *Angewandte Chemie International Edition*, vol. 54, no. 6, pp. 1791–1794, Dec. 2014 (cit. on p. 65).

[98] J. M. Azpiroz, E. Mosconi, J. Bisquert, F. D. Angelis, 'Defect migration in methylammonium lead iodide and its role in perovskite solar cell operation', *Energy & Environmental Science*, vol. 8, no. 7, pp. 2118–2127, 2015 (cit. on p. 67).

[99] C. Eames, J. M. Frost, P. R. F. Barnes, B. C. O'Regan, A. Walsh, M. S. Islam, 'Ionic transport in hybrid lead iodide perovskite solar cells', *Nature Communications*, vol. 6, no. 1, Jun. 2015 (cit. on p. 67).

[100] D. A. Egger, L. Kronik, A. M. Rappe, 'Theory of hydrogen migration in organic-inorganic halide perovskites', *Angewandte Chemie International Edition*, vol. 54, no. 42, pp. 12 437–12 441, Jun. 2015 (cit. on p. 67).

[101] X. Zhang, J.-X. Shen, M. E. Turiansky, C. G. V. de Walle, 'Minimizing hydrogen vacancies to enable highly efficient hybrid perovskites', *Nature Materials*, Apr. 2021 (cit. on p. 67).

[102] J. Zhao, Y. Deng, H. Wei, X. Zheng, Z. Yu, Y. Shao, J. E. Shield, J. Huang, 'Strained hybrid perovskite thin films and their impact on the intrinsic stability of perovskite solar cells', *Science Advances*, vol. 3, no. 11, eaao5616, Nov. 2017 (cit. on pp. 67, 120).

[103] C. Motta, F. El-Mellouhi, S. Kais, N. Tabet, F. Alharbi, S. Sanvito, 'Revealing the role of organic cations in hybrid halide perovskite $CH_3NH_3PbI_3$', *Nature Communications*, vol. 6, no. 1, Apr. 2015 (cit. on pp. 67, 69).

[104] J. Gong, M. Yang, X. Ma, R. D. Schaller, G. Liu, L. Kong, Y. Yang, M. C. Beard, M. Lesslie, Y. Dai, B. Huang, K. Zhu, T. Xu, 'Electron–rotor interaction in organic–inorganic lead iodide perovskites discovered by isotope effects', *The Journal of Physical Chemistry Letters*, vol. 7, no. 15, pp. 2879–2887, Jul. 2016 (cit. on pp. 67–70).

[105] A. A. Bakulin, O. Selig, H. J. Bakker, Y. L. Rezus, C. Müller, T. Glaser, R. Lovrincic, Z. Sun, Z. Chen, A. Walsh, J. M. Frost, T. L. C. Jansen, 'Real-time observation of organic cation reorientation in methylammonium lead iodide perovskites', *The Journal of Physical Chemistry Letters*, vol. 6, no. 18, pp. 3663–3669, Sep. 2015 (cit. on pp. 67–70, 124).

[106] F. Brivio, J. M. Frost, J. M. Skelton, A. J. Jackson, O. J. Weber, M. T. Weller, A. R. Goñi, A. M. A. Leguy, P. R. F. Barnes, A. Walsh, 'Lattice dynamics and vibrational spectra of the orthorhombic, tetragonal, and cubic phases of methylammonium lead iodide', *Physical Review B*, vol. 92, no. 14, p. 144 308, Oct. 2015 (cit. on pp. 67, 68).

[107] E. Mosconi, C. Quarti, T. Ivanovska, G. Ruani, F. D. Angelis, 'Structural and electronic properties of organo-halide lead perovskites: A combined IR-spectroscopy and ab initio molecular dynamics investigation', *Phys. Chem. Chem. Phys.*, vol. 16, no. 30, pp. 16 137–16 144, 2014 (cit. on pp. 67, 68, 124).

[108] I. Anusca, S. Balčiūnas, P. Gemeiner, Š. Svirskas, M. Sanlialp, G. Lackner, C. Fettkenhauer, J. Belovickis, V. Samulionis, M. Ivanov, B. Dkhil, J. Banys, V. V. Shvartsman, D. C. Lupascu, 'Dielectric response: Answer to many questions in the methylammonium lead halide solar cell absorbers', *Advanced*

Energy Materials, vol. 7, no. 19, p. 1 700 600, May 2017 (cit. on pp. 67, 68, 110, 124).

[109] O. Knop, R. E. Wasylishen, M. A. White, T. S. Cameron, M. J. M. V. Oort, 'Alkylammonium lead halides. part 2. $CH_3NH_3PbX_3$ (X = Cl, Br, I) perovskites: Cuboctahedral halide cages with isotropic cation reorientation', *Canadian Journal of Chemistry*, vol. 68, no. 3, pp. 412–422, Mar. 1990 (cit. on p. 67).

[110] T. Baikie, Y. Fang, J. M. Kadro, M. Schreyer, F. Wei, S. G. Mhaisalkar, M. Grätzel, T. J. White, 'Synthesis and crystal chemistry of the hybrid perovskite $CH_3NH_3PbI_3$ for solid-state sensitised solar cell applications', *Journal of Materials Chemistry A*, vol. 1, no. 18, p. 5628, 2013 (cit. on p. 67).

[111] T. Glaser, C. Müller, M. Sendner, C. Krekeler, O. E. Semonin, T. D. Hull, O. Yaffe, J. S. Owen, W. Kowalsky, A. Pucci, R. Lovrinčić, 'Infrared spectroscopic study of vibrational modes in methylammonium lead halide perovskites', *The Journal of Physical Chemistry Letters*, vol. 6, no. 15, pp. 2913–2918, Jul. 2015 (cit. on pp. 68, 124).

[112] A. Poglitsch, D. Weber, 'Dynamic disorder in methylammoniumtrihalogenoplumbates (II) observed by millimeter-wave spectroscopy', *The Journal of Chemical Physics*, vol. 87, no. 11, pp. 6373–6378, Dec. 1987 (cit. on pp. 68, 124).

[113] F. Brivio, A. B. Walker, A. Walsh, 'Structural and electronic properties of hybrid perovskites for high-efficiency thin-film photovoltaics from first-principles', *APL Materials*, vol. 1, no. 4, p. 042 111, Oct. 2013 (cit. on pp. 68, 124).

[114] J.-H. Lee, N. C. Bristowe, P. D. Bristowe, A. K. Cheetham, 'Role of hydrogen-bonding and its interplay with octahedral tilting in $CH_3NH_3PbI_3$', *Chemical Communications*, vol. 51, no. 29, pp. 6434–6437, 2015 (cit. on p. 68).

[115] V. Arrighi, J. S. Higgins, A. N. Burgess, W. S. Howells, 'Rotation of methyl side groups in polymers: A fourier transform approach to quasielastic neutron scattering. 1. homopolymers', *Macromolecules*, vol. 28, no. 8, pp. 2745–2753, Apr. 1995 (cit. on p. 68).

[116] D. J. Kubicki, D. Prochowicz, A. Hofstetter, P. Péchy, S. M. Zakeeruddin, M. Grätzel, L. Emsley, 'Cation dynamics in mixed-cation $MA_xFA_{1-x}PbI_3$ hybrid perovskites from solid-state NMR', *Journal of the American Chemical Society*, vol. 139, no. 29, pp. 10 055–10 061, Jul. 2017 (cit. on p. 70).

[117] D. J. Kubicki, D. Prochowicz, A. Hofstetter, M. Saski, P. Yadav, D. Bi, N. Pellet, J. Lewiński, S. M. Zakeeruddin, M. Grätzel, L. Emsley, 'Formation of stable mixed guanidinium-methylammonium phases with exceptionally long carrier lifetimes for high-efficiency lead iodide-based perovskite photovoltaics', *Journal of the American Chemical Society*, vol. 140, no. 9, pp. 3345–3351, Feb. 2018 (cit. on p. 70).

[118] O. Selig, A. Sadhanala, C. Müller, R. Lovrincic, Z. Chen, Y. L. A. Rezus, J. M. Frost, T. L. C. Jansen, A. A. Bakulin, 'Organic cation rotation and immobilization in pure and mixed methylammonium lead-halide perovskites', *Journal of the American Chemical Society*, vol. 139, no. 11, pp. 4068–4074, Mar. 2017 (cit. on p. 70).

[119] L. Pauling, 'The structure and entropy of ice and of other crystals with some randomness of atomic arrangement', *Journal of the American Chemical Society*, vol. 57, no. 12, pp. 2680–2684, Dec. 1935 (cit. on p. 71).

[120] W. K. David Eisenberg, *The Structure and Properties of Water*. OUP Oxford, Oct. 20, 2005, 316 pp. [Online]. Available: https://www.ebook.de/de/product/4443557/david_eisenberg_walter_kauzmann_the_structure_and_properties_of_water.html (cit. on p. 71).

[121] Y. Maniwa, H. Kataura, M. Abe, A. Udaka, S. Suzuki, Y. Achiba, H. Kira, K. Matsuda, H. Kadowaki, Y. Okabe, 'Ordered water inside carbon nanotubes: Formation of pentagonal to octagonal ice-nanotubes', *Chemical Physics Letters*, vol. 401, no. 4-6, pp. 534–538, Jan. 2005 (cit. on p. 71).

[122] C. Luo, W. Fa, J. Zhou, J. Dong, X. C. Zeng, 'Ferroelectric ordering in ice nanotubes confined in carbon nanotubes', *Nano Letters*, vol. 8, no. 9, pp. 2607–2612, Sep. 2008 (cit. on p. 71).

[123] M. J. Iedema, M. J. Dresser, D. L. Doering, J. B. Rowland, W. P. Hess, A. A. Tsekouras, J. P. Cowin, 'Ferroelectricity in water ice', *The Journal of Physical Chemistry B*, vol. 102, no. 46, pp. 9203–9214, Nov. 1998 (cit. on p. 71).

[124] C. Spagnoli, K. Loos, A. Ulman, M. K. Cowman, 'Imaging structured water and bound polysaccharide on mica surface at ambient temperature', *Journal of the American Chemical Society*, vol. 125, no. 23, pp. 7124–7128, Jun. 2003 (cit. on p. 71).

[125] W.-H. Zhao, J. Bai, L.-F. Yuan, J. Yang, X. C. Zeng, 'Ferroelectric hexagonal and rhombic monolayer ice phases', *Chem. Sci.*, vol. 5, no. 5, pp. 1757–1764, 2014 (cit. on p. 71).

[126] H.-X. Zhao, X.-J. Kong, H. Li, Y.-C. Jin, L.-S. Long, X. C. Zeng, R.-B. Huang, L.-S. Zheng, 'Transition from one-dimensional water to ferroelectric ice within a supramolecular architecture', *Proceedings of the National Academy of Sciences*, vol. 108, no. 9, pp. 3481–3486, Feb. 2011 (cit. on p. 71).

[127] D. Linde, *CRC Handbook of Chemistry and Physics, 87th Edition*. Taylor & Francis, 2006. [Online]. Available: https://books.google.de/books?id=yTTUQgAACAAJ (cit. on p. 73).

[128] S. L. Shostak, W. L. Ebenstein, J. S. Muenter, 'The dipole moment of water. i. dipole moments and hyperfine properties of H_2O and HDO in the ground and excited vibrational states', *The Journal of Chemical Physics*, vol. 94, no. 9, pp. 5875–5882, May 1991 (cit. on p. 73).

[129] A. I. Kolesnikov, G. F. Reiter, N. Choudhury, T. R. Prisk, E. Mamontov, A. Podlesnyak, G. Ehlers, A. G. Seel, D. J. Wesolowski, L. M. Anovitz, 'Quantum tunneling of water in beryl: A new state of the water molecule', *Physical Review Letters*, vol. 116, no. 16, Apr. 2016 (cit. on pp. 74, 76, 146, 147).

[130] Y. Nakajima, S. Naya, 'Orientational phase transition and dynamic susceptibility of hindered-rotating dipolar system –a librator-rotator model–', *Journal of the Physical Society of Japan*, vol. 63, no. 3, pp. 904–914, Mar. 1994 (cit. on pp. 74, 76).

[131] R. I. Mashkovtsev, V. G. Thomas, D. A. Fursenko, E. S. Zhukova, V. V. Uskov, B. P. Gorshunov, 'FTIR spectroscopy of D_2O and HDO molecules in the c-axis channels of synthetic beryl', *American Mineralogist*, vol. 101, no. 1, pp. 175–180, Jan. 2016 (cit. on pp. 77, 78).

[132] *Impedance measurement handbook*, 6th, Keysight technologies, 2016 (cit. on pp. 81–83).

[133] *Alpha-a high resolution dielectric, conductivity, impedance and gain-phase modular measurement system maunal*, 7th, Agilent Technologies, Dec. 2000 (cit. on p. 81).

[134] *Alpha-a high resolution dielectric, conductivity, impedance and gain-phase modular measurement system user's maunal*, 3.4, Novocontrol Technologies GmbH & Co. KG, Jun. 2017 (cit. on p. 81).

[135] 'Characterizing diamonds with FT-IR spectroscopy', *AZO Materials*, 2019 (cit. on p. 87).

[136] H.-K. Mao, X.-J. Chen, Y. Ding, B. Li, L. Wang, 'Solids, liquids, and gases under high pressure', *Reviews of Modern Physics*, vol. 90, no. 1, p. 015 007, Mar. 2018 (cit. on p. 89).

[137] D. J. Dunstan, 'Theory of the gasket in diamond anvil high-pressure cells', *Review of Scientific Instruments*, vol. 60, no. 12, pp. 3789–3795, Dec. 1989 (cit. on p. 91).

[138] M. I. Eremets, *High Pressure Experimental Methods*. Oxford University Press, Feb. 1, 1996, 406 pp. [Online]. Available: https://www.ebook.de/de/product/3604143/m_i_eremets_high_pressure_experimental_methods.html (cit. on p. 91).

[139] E. Jameson, *Electrical Discharge Machining*. Society of Manufacturing Engineers, Marketing Services Division, 1983, 2001. [Online]. Available: https://books.google.de/books?id=cAwAogEACAAJ (cit. on p. 91).

[140] A. P. Drozdov, M. I. Eremets, I. A. Troyan, V. Ksenofontov, S. I. Shylin, 'Conventional superconductivity at 203 Kelvin at high pressures in the sulfur hydride system', *Nature*, vol. 525, no. 7567, pp. 73–76, Aug. 2015 (cit. on p. 94).

[141] F. Capitani, B. Langerome, J.-B. Brubach, P. Roy, A. Drozdov, M. I. Eremets, E. J. Nicol, J. P. Carbotte, T. Timusk, 'Spectroscopic evidence of a new energy scale for superconductivity in H_3S', *Nature Physics*, vol. 13, no. 9, pp. 859–863, Jun. 2017 (cit. on p. 94).

[142] H. K. Mao, J. Xu, P. M. Bell, 'Calibration of the ruby pressure gauge to 800 kbar under quasi-hydrostatic conditions', *Journal of Geophysical Research*, vol. 91, no. B5, p. 4673, 1986 (cit. on p. 96).

[143] G. J. Piermarini, S. Block, J. D. Barnett, R. A. Forman, 'Calibration of the pressure dependence of the $R1$ ruby fluorescence line to 195 kbar', *Journal of Applied Physics*, vol. 46, no. 6, pp. 2774–2780, Jun. 1975 (cit. on p. 96).

[144] M. Kollár, L. Ćirić, J. H. Dil, A. Weber, S. Muff, H. M. Ronnow, B. Náfrádi, B. P. Monnier, J. S. Luterbacher, L. Forró, E. Horváth, 'Clean, cleaved surfaces of the photovoltaic perovskite', *Scientific Reports*, vol. 7, no. 1, p. 695, Apr. 2017 (cit. on p. 102).

[145] V. Merkl, 'Investigations of high pressure phases in hybrid perovskites via infrared spectroscopy', Bachelor's Thesis, Universität Stuttgart, 2020 (cit. on p. 103).

[146] B. Klis, 'Memory effects in halide perovskites: High pressure infrared investigations', Bachelor's Thesis, Universität Stuttgart, 2020 (cit. on p. 116).

[147] N. A. M. Elliger, 'Investigations of high pressure phases in hybrid perovskites via infrared spectroscopy', Bachelor's Thesis, Universität Stuttgart, 2021 (cit. on pp. 114, 116).

[148] S. Endo, K. Deguchi, M. Tokunaga, 'Quantum paraelectricity in KD_2PO_4 and KH_2PO_4 under high pressure', *Physical Review Letters*, vol. 88, no. 3, p. 035 503, Jan. 2002 (cit. on p. 145).

[149] M. A. Belyanchikov, E. S. Zhukova, S. Tretiak, A. Zhugayevych, M. Dressel, F. Uhlig, J. Smiatek, M. Fyta, V. G. Thomas, B. P. Gorshunov, 'Vibrational states of nano-confined water molecules in beryl investigated by first-principles calculations and optical experiments', *Physical Chemistry Chemical Physics*, vol. 19, no. 45, pp. 30 740–30 748, 2017 (cit. on p. 146).

[150] L. Jibuti, 'Quantum phases of water molecules in nano-cavities', M.S. thesis, University of Stuttgartt, Institute for Theoretical Physics III, 2018 (cit. on pp. 147, 148).

Declaration

I hereby declare that this thesis and the work reported herein was composed by and originated entirely from me. Information derived from the published and unpublished work of others has been acknowledged in the text and references.

Yuk Tai Chan

Date